MICROSTRUCTURAL AND MICROHARDNESS CHARACTERIZATION OF PRIMARY AND RECYCLED CAST AL-SI PISTON ALLOYS PROCESSED BY HIGH-PRESSURE TORSION

FREDRICK MADARAKA MWEMA

MASTER OF SCIENCE
(Mechanical Engineering)

JOMO KENYATTA UNIVERSITY OF AGRICULTURE AND TECHNOLOGY

2015

Microstructural and Microhardness Characterization of Primary and Recycled Cast Al-Si Piston Alloys Processed by High-pressure Torsion

Fredrick Madaraka Mwema

A thesis submitted in partial fulfillment of the requirements for the award of Master of Science degree in Mechanical Engineering in the Jomo Kenyatta University of Agriculture and Technology

2015

DECLARATION

This thesis is my original work and has not been presented for a degree in any other University.

Signature:.. Date..................

Fredrick Madaraka Mwema

This thesis has been submitted for examination with our approval as the University Supervisors.

Signature:.. Date..................

Dr. Thomas O. Mbuya

University of Nairobi, Kenya

Signature:.. Date..................

Dr. Bruno R. Mose

JKUAT, Kenya

Signature:.. Date..................

Dr. James N. Keraita

DeKUT, Kenya

DEDICATION

I dedicate this work to my sweetheart, Joan Mwîhaki and our playful twin sons, Victor Mwema and Robin Nyika; you are my powerhouse. To my aging grandmother, Agnes Kûla, 'vai kyaasa kitemuthia'; you are my source of inspiration.

ACKNOWLEDGEMENT

I would like to express my sincere appreciation to the following people whose support was invaluable to this work.

Firstly, I would like to thank my supervisors Dr. Mbuya, Dr. Bruno and Dr. Keraita for their invaluable guidance, leadership and motivation during the course of this work. It is through their advice that I was able to learn 'how to undertake a scientific research' and complete this work.

Secondly, special thanks to Professor Philippa Reed, the head of Materials Research Group, University of Southampton, UK for hosting me as a visiting postgraduate student, for financing my SEM sessions and for taking her time to engage in useful discussions regarding my research. Thirdly, huge thanks to Dr. Nong Gao and Dr. C.T. Wang, both of University of Southampton, UK. Dr. Nong Gao has been very resourceful to me since we first met in October 2013 in Southampton while Dr. CT Wang assisted in the initial preparation of the high-pressure torsion samples.

My sincere appreciation to DeKUT for financial support. I also acknowledge the University of Nairobi for allowing me to use their facilities.

Last but not least, I would like to thank my family, and most importantly, my wife for understanding me throughout the research period. Her prayers and support encouraged me even when I felt like giving up.

TABLE OF CONTENTS

LIST OF TABLES

LIST OF FIGURES

ABBREVIATIONS

ARB	Accumulative Roll Bonding
EBSD	Electron Backscatter Diffraction
ECAP	Equal Channel Angular Pressing
FSW	Friction Stir Welding
GBs	Grain Boundaries
HAGBs	High Angle Grain Boundaries
HPT	High Pressure Torsion
LAGBs	Low Angle Grain Boundaries
OIM	Orientation Imaging Microscopy
RPM	Revolution Per Minute
SEM	Scanning Electron Microscope
SPD	Severe Plastic Deformation
UFG	Ultra-Fine Grain
VHN	Vickers Hardness Number

NOMENCLATURE

Symbols

h	Thickness of HPT sample
N	Number of High Pressure-Torsion turns
n	Number of Equal Channel Angular Pressing passes/cycles
P	Compression Load per area
r	Distance from the center of HPT sample
T	Torsion
ϵ	Equivalent strain
ϵ_{true}	True strain
γ	Shear strain
θ	Angle of twist due to torsion in HPT

ABSTRACT

This research has characterized the microstructure and microhardness properties of primary (virgin material) and recycled (herein referred to as secondary alloys) cast Al-Si piston alloys processed by high-pressure torsion. Three primary Al-Si piston all alloys (Al-12%Si, unmodified Al-7%Si and modified Al-7%Si) and one secondary Al-Si piston alloy (10.6%Si piston alloy) were investigated. Modification of Al-7%Si alloy was achieved through addition of silicon modifier (strontium). All the alloys were processed by high-pressure torsion at room temperature for constant speed of 1 revolution per minute and at a pressure of 3.0 GPa. The samples were processed up to 10 high-pressure turns.

It was found that both primary and secondary alloys behaved similarly during high-pressure torsion. Microhardness for all the alloys increased with number of turns along the diameter as revealed by the microhardness line profiles. Furthermore, the microhardness for most of the alloys were symmetrical about the centre; with lowest microhardness at centre. The microhardness along the diameter of all the samples tended towards homogeneity although a homogenous microhardness distribution was not achieved after 10 turns. However, it was found that Al-12%Si alloy exhibited a very high microhardness gradient even after 10 turns. The microhardness in primary modified silicon (modified Al-7%Si) alloy increased slowly compared to the other alloys. This is because there was only breakdown

of the Si structures rather than Si particles as observed for the other alloys. The microhardness-equivalent strain relationship revealed that all the alloys studied in this work undergo strain hardening with slow recovery during high-pressure torsion.

Microstructural analysis through Scanning Electron Microscopy, optical microscope and ImageJ software, revealed that fine structures can be achieved through high-pressure torsion of both primary and secondary Al-Si piston alloys. The microstructural analysis and Weibull distribution plots of particle sizes revealed smaller phases at the edges than at the centre for all the alloys even after 10 turns. This indicates that Al-Si piston alloys do not breakdown fully after 10 turns unlike simple Al-Si alloys and pure aluminium. After 10 turns, for all the alloys, it was observed that nearly all the intermetallic phases except the Si-rich phases had broken down and redistributed within the Al-matrix. It was also observed that there was not much break down of the Si particles in the modified Al-Si piston alloy since most of the break down was observed on the network of modified Si structures after 10 turns.

These results indicate the possibility of processing Al-Si piston alloys to ultrafine grain structures through high-pressure torsion for improved performance in their application as engine materials. However, future work is recommended on processing the samples for more than 10 turns to evaluate the achievement of homogenous microstructure. To further understand the deformation mechanisms, grain boundary and dislocation motions should be studied.There is also need to characterize the high-pressure torsion processed Al-Si piston alloys for other properties such as thermal stability, corrosion and wear.

CHAPTER ONE

1.0 INTRODUCTION

1.1 Background

Severe plastic deformation (SPD) has been shown to produce materials with exceptionally small grain sizes [1] and has therefore attracted the interest of many researchers and experts in materials engineering as a means of processing materials [1]. Some of the most common SPD techniques include equal channel angular pressing (ECAP), high-pressure torsion (HPT), multiple forging, friction stir welding (FSW) and accumulative roll bonding (ARB) [1]. ARB refines materials up to an average grain size of 2 μm [2], ECAP refines materials to an average grain size range of 0.3-0.5 μm [3] while HPT refines materials up to 0.1 μm [1,3]. This means that ECAP and HPT refine materials into ultra-fine grain (UFG) structures (UFG materials are those materials whose grain sizes are less than 1 micron). Compared to ECAP, HPT achieves higher grain refinement since higher strains are involved [1,3,4]. This is because there is application of both torsion and compression on the sample during HPT. Additionally, compared to other methods, HPT processes materials with minimal change in overall dimensions [1]. As such, HPT is the most attractive SPD technique.

HPT-processed materials offer several attractive properties. These materials exhibit high strength at room temperatures according to the Hall-Petch relationship [5]. They exhibit superplastic properties at 50% absolute melting temperature ($0.5T_m$) [6]. They also have high fracture toughness. The most attractive and extraordinary feature of HPT-processed materials is that they possess high strength and high ductility [7, 8]. This is because deformation in UFG materials occurs through grain boundary sliding and enhanced grain rotation rather than dislocation motion, thereby enhancing both ductility and strength [7–9].

Because of these attractive properties, extensive research has been conducted on different metals and alloys processed by HPT. For instance, studies have been conducted on the properties of HPT processed pure metals such as high purity nickel [10, 11], austenitic steel [12], copper [13] and aluminium [14]. Microstructure and mechanical properties of bulk nanostructured tantalum and tungsten materials processed by high-pressure torsion have also been reported [15, 16]. Recently, microstructural and microhardness characterization of HPT processed aluminium alloys has been reported; some of these alloys include Al-Mg-Sc alloy [17], cast Al-7%Si alloy [18, 19], Al-7075 [20], Al-2024 [4], Al-2%Si-0.25%Sc [21] and many others. Due to the small sizes of the HPT processed samples, most of these materials can find applications in micro-mechanical systems and biomedical mini-components (such as screws, springs and staples) [22, 23]. HPT-processed ring specimens can find application in producing washers [24].

Although considerable studies have been carried out on HPT processing of Al alloys, including Al-Si alloys, little information exist on HPT processing of Al-Si alloys used in automobile engine piston [25–27]. The effects of HPT on Al-Si piston alloys cannot be assumed to be like those of simple Al-Si alloys since the microstructure of these alloys is complex comprising of a complex network of Si particles and other second phases such as various types of intermetallics. Therefore, the breakdown and evolution of such complex structures during HPT and the subsequent effect on microhardness, which correlates directly with wear and other mechanical properties of the material, would be interesting aspects to study. Furthermore, the effect of HPT on recycled (or secondary) materials has not been studied extensively.

Grain refinement of Al-Si piston materials has been shown to reduce failures of the most loaded areas of an engine piston [25]. Some of the highly-stresssed regions include piston bowl rim, pin and pon bore [25]. Thermo-mechanical treatments such as bowl remelting which are currently used are associated with high-temperature challenges such as formation of pores, oxidation and heat affected zone (HAZ) and as such a limited level of grain refinement can be achieved [26,27]. HPT is not associated with these challenges and has been shown to produce bulk nanostructured materials. Therefore, the present research has characterized the microstructure and microhardness properties of HPT-processed Al-Si piston alloy to present HPT as an alternative grain refinement process for the piston material.

1.2 Problem Statement

Grain refinement of piston material (Al-Si alloy) around the bowl rim, pin and pin bore has proven to prolong the life of the engine pistons [26]. Presently, remelting of the bowl rim is used to reduce crack initiation in the bowl rim [26]. However, this process is associated with formation of pores and oxides in addition to degradation of mechanical properties in the heat affected zone during the remelting process. HPT has been found effective in grain refinement of metals and alloys and is contaminant and porosity-free [23]. Although extensive studies have been carried out on different alloys, HPT has not been carried out on Al-Si piston alloys. Therefore, the effect of HPT on Al-Si piston alloys has not been understood. Furthermore, no single SPD technique has been used for grain refinement of piston alloys. Therefore, by characterizing the microstructure and microhardness of Al-Si piston alloys, this study provides information on the effect of HPT on Al-Si piston alloys, which is currently lacking. Such information maybe used to evaluate HPT as an alternative grain refinement process for engine materials in future.

1.3 Objectives

The main objective of this research is to characterize the evolution of microstructure and microhardness of primary and recycled cast Al-Si piston alloys processed by high-pressure torsion. To achieve this, the following specific objectives have been identified:

(i) To characterize microstructural evolution and homogeneity with the number of HPT turns.

(ii) To characterize the evolution and distribution of microhardness with the number of HPT turns.

1.4 Thesis outline

This thesis is divided into six chapters of which this is the first. Chapter 2 provides the literature review on the principles of HPT and the previous research carried out on the effects of HPT on material properties. Chapter 3 contains the methodology used in carrying out this research. Chapters 4 and 5 report the results together with discussion on the effect of HPT on microstructure and microhardness of primary and secondary Al-Si piston alloys respectively. Finally, chapter 6 contains a summary of all findings and conclusions drawn from the study.

CHAPTER TWO

2.0 LITERATURE REVIEW

2.1 Introduction

The chapter describes the fundamentals of severe plastic deformation (SPD) with focus on HPT. The microstructure and microhardness properties of aluminium and Al-based alloys are also reviewed.

2.2 Severe Plastic Deformation (SPD)

Severe plastic deformation is any processing/forming method under which the material is subjected to intense hydrostatic pressure to impart very high strains without significant change in dimension and shape of the sample. The high strain involved leads to a very high density of lattice dislocations and hence exceptional grain refinement [22]. As listed below, severe plastic deformation has three distinct advantages over the traditional plastic deformation methods such as cold rolling, forging and drawing [1].

- Materials processed by SPD methods have ultra-fine grains (UFG) structures and high angle grain boundaries (HAGBs), which increase their strength [28] whereas, materials processed by traditional methods have low angle grain boundaries (LAGBs) and cellular-type substructures. This is because, in

SPD processing, it is possible to alter the strain path unlike in traditional methods where the strain path is continuous.

- SPD techniques process materials with minimal alteration to their overall dimensions. Consequently, as the straining increases, there is formation of relatively homogenous nanostructures throughout the volume of materials processed by SPD techniques.
- SPD techniques impose larger plastic strains without causing any mechanical damage or cracks in the material. Cracks cause failure in materials.

Equal channel angular pressing (ECAP) and high-pressure torsion (HPT) impose larger plastic strains (true strains, ϵ_{true}, >10), therefore, resulting in formation of more UFGs [1, 22]. HPT causes more deformation than ECAP and, therefore, higher microstructural refinement can be achieved [29].

Since this research is based on HPT, the principles of the HPT process and properties of the HPT processed materials are presented in more detail in the subsequent sections of this chapter.

2.3 High-pressure Torsion (HPT)

The concept of HPT was first presented in 1943 by Bridgeman [30]. It involves subjecting a sample to a high compression load per unit area (P), combined with torsion between two anvils. The upper anvil is under compression while the lower anvil rotates to provide torsion (T) to the sample (Figure 2.1).

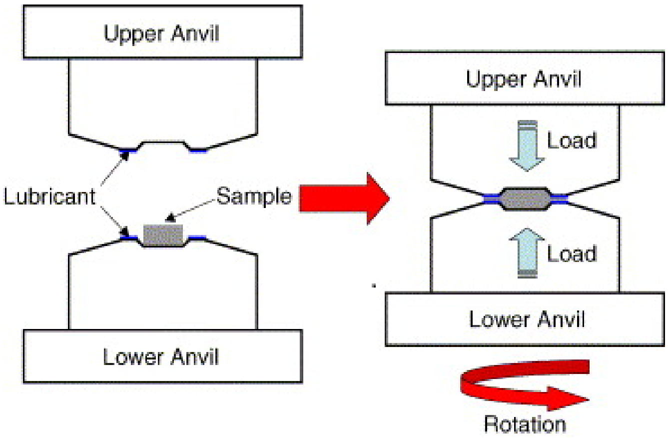

Figure 2.1: A schematic showing the principle of the HPT process [17]

The sample is usually a solid disk with a typical diameter of 10 millimeters and thickness of about 1 mm. These sample dimensions depend on the size of the dies of the high-pressure machine. As indicated in Figure 2.1, the design of the tool is such that the process occurs under quasi-constrained conditions [1, 22]. Quasi-constrained conditions means that the sample is partially constrained between the two anvils. Under these conditions, the sample is deformed without major outflow of the material between the two anvils. The deformation of the sample is caused by the surface friction between the two anvils and the sample. By considering a typical HPT sample shown in Figure 2.2, the equations for strain estimations have been developed as shown by equations (2.1), (2.2), (2.3) and (2.4) [11, 22].

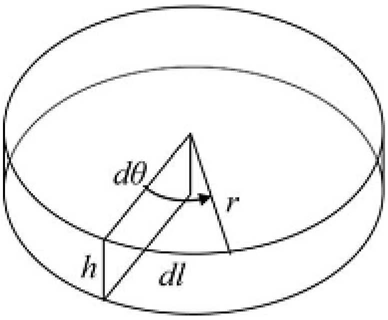

Figure 2.2: Strain parameters in HPT [11]

From Figure 2.2, dθ is a small rotation and dl is the displacement of the element. For $r > 0$, the shear strain (γ) is given by;

$$\gamma = \frac{2\pi N r}{h} \tag{2.1}$$

Where N is the number of rotations of the lower HPT anvil (commonly referred to as the number of HPT turns), h is the sample thickness and r is the distance from the center of the sample. The equivalent strain, ϵ, is given by the Von Mises criterion as follows [31];

$$\epsilon = \frac{2\pi N r}{h\sqrt{3}} \tag{2.2}$$

Equation (2.2) is used when very small shear strains are imposed ($\gamma < 0.8$). For shear strains equal or larger than 0.8, the strain is given by equation (2.3) [31].

$$\epsilon = \frac{2}{\sqrt{3}} ln[(1 + \frac{\gamma^2}{4})^{\frac{1}{2}} + \frac{\gamma}{2}] \tag{2.3}$$

During HPT processing, the material may experience reduction in thickness. As such, Degtyarev [32] established the following relationship to account for this decrease.

$$\epsilon_{true} = ln(\frac{2\pi N r h_o}{h^2}) \tag{2.4}$$

Where h_o and h denote the original and final thicknesses respectively.

These equations are a good estimation of the theoretical variation of strain along the diameter of the sample but do not hold for the central region ($r = 0$).

2.4 Properties of HPT processed materials

2.4.1 Introduction

High-pressure torsion has been carried out on a wide range of metals and their alloys [31]. In this subsection, effects of HPT on microstructure and microhardness properties of pure aluminium, Al-Si and other alloys are reviewed. Because of the small size of HPT samples, microstructure and microhardness are the most accurate and easiest properties to undertake. This is why they are widely used to characterize HPT-processed materials. It requires very specialized equipment to undertake other mechanical tests on such small samples. Microhardness, which represents the mechanical properties, depends on the microstructure of the material.

2.4.2 Microstructure of HPT-processed aluminium and aluminium-based alloys

Extensive data are available on HPT processing of aluminium and aluminium-based alloys [4, 14, 17–21, 33]. The general finding from these reports is that HPT refines aluminium and aluminium-based alloys into UFG structures with average grain sizes within the range of ∼0.1-0.3 μm or even smaller [22]. For instance, HPT has been used to process pure aluminium to an average grain size of 0.1 μm [14] and 0.8 μm [34–36], Al-7%Si at room temperature and 445K to mean grain sizes of 0.3 μm and 1.3 μm respectively [18, 19]. It has also been used to process Al-7%Si-0.25%Sc to a mean grain size of about 0.15 μm [21] and Al-6061 at room temperature to an average grain size of about 0.5μm [33]. Previous researchers have reported HPT processing of Al-2024 at room temperature and at 673K to average grain sizes of about 0.15 and 0.3 μm respectively and Al-7075 at room temperature to an average grain size of 0.25 μm [4, 20]. These grain sizes are considerably smaller compared to those achieved through ARB and ECAP of aluminium and aluminium alloys [2, 3, 31, 37–41]. However these studies did not detail the transformation of different phases present during the HPT process.

At low number of HPT turns (less than 5 turns), pure aluminium exhibits non-homogenous grain refinement with higher refinement reported at the edges of the sample [34–36]. For instance, Zhilyaev et al [35] reported that after 2 turns of

HPT-processing of 99.7% pure aluminium, average grain sizes of 1.5 μm and 1 μm were obtained at the center and edge respectively. After 8 turns, a homogenous average grain size of 0.8 μm was reported [35]. This variation in grain refinement along the diameter of the samples is consistent with the strain variation model shown by equation 2.4 and other reports [34, 36]. However, it was, on the contrary, reported [35] that beyond eight revolutions, higher grain refinement occurs at the center than at the periphery of the samples. This agrees with Zhilyaev et al's study [14], which reported smaller grain sizes at the central region than at the periphery of the sample beyond two turns. These findings contradict other studies on pure aluminium [24, 34, 36, 42], which have reported smaller grain sizes at the periphery of the samples even at high number of turns. The findings also contradict the theoretical strain variation along the diameter predicted by equation (2.4). This behavior was attributed to high stacking fault energy at the highly-strained edges of the sample, which results in dynamic recovery (and hence growth) of the grains at the edges [22, 35]. In pure Al, it was shown that homogenous microstructure is achieved through grain refinement-recovery cycle at the periphery followed by the grain refinement of the central region of the sample eventually [14, 24, 34–36, 42]. As shown in Figure 2.3, the microstructure at the central region has relatively smaller grains contrary to the strain hardening theory [35]. The ‘continuous circles’ rather than ‘spots’ in both Figures 2.3a and 2.3b on the selected area electron diffraction (SAD) inset indicate the presence of smaller grains than at the edge of the sample.

Similar to pure aluminium, simple aluminium alloy systems processed by HPT have been shown to exhibit nonhomogenous grain refinement along the diameter of the samples at low number of turns [4, 17]. Microstructural inhomogeneity at low turns was reported for HPT processed samples of Al-3%Mg-0.2%Sc [17]. In this report, it was observed that the microstructure at the outer region of the sample was highly distorted consisting of an array of UFG structures with an average grain size of about 0.17 μm after 1 turn. As shown by the continuous rings of SAD pattern in Figure 2.4a, the grains had boundaries with high angles of misorientation (HAGBs) and the structure contained tangles of dislocations and high-energy non-stable grain boundaries. Similar observation was reported for other HPT processed Al-1.5%Mg and Al-3%Mg solid solution alloys examined by high-resolution electron microscopy (HREM) [43].

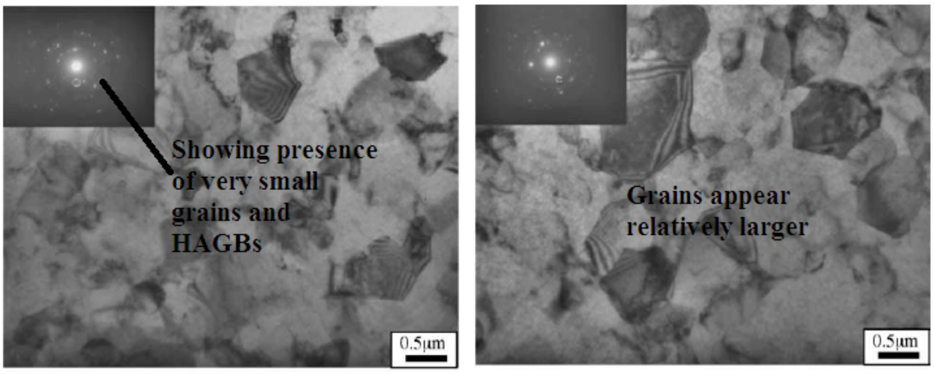

(a) Central region (b) Periphery

Figure 2.3: TEM micrographs showing finer grains at the central in Al for N=8 [35]

The presence of high-energy and non-equilibrium grain boundaries on the highly strained regions of an HPT sample has also been reported for annealed and solution treated Al-2024 processed at room temperature [17] and for other alloys [44]. Examination of the central region revealed contrasting results; the microstructure contained coarse microstructure of irregular grains and ill-defined grain boundaries. The SAD pattern at the central region, shown in Figure 2.4b, contained diffraction spots, which implies that the central core consisted of LAGBs.

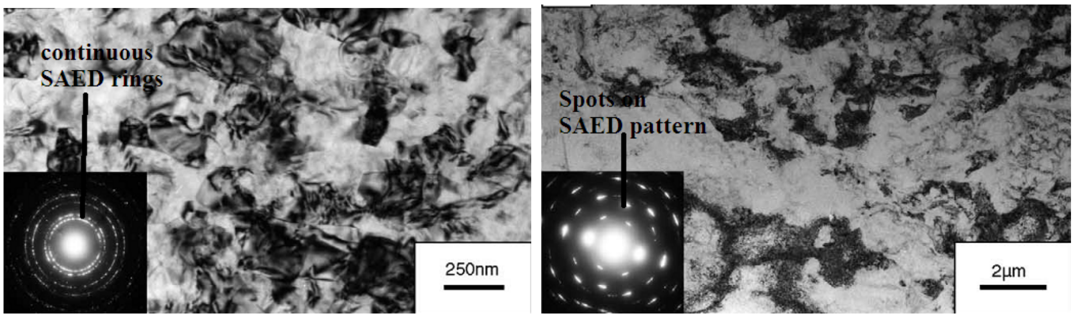

(a) Edge (b) Central core

Figure 2.4: TEM micrographs and SAED patterns showing inhomogenous microstructure for Al-3%Mg-0.2%Sc after N=1 [17]

Severe plastic deformation in aluminium alloys occurs through evolution of LAGBs into HAGBs [20, 33]. It was reported through orientation imaging microscopy (OIM) that unprocessed Al-7075 consists of elongated grain structure with LAGBs as shown in Figure 2.5a [20]. However, on HPT processing with 5 turns, an equiaxed grain structure with HAGBs was obtained as shown in Figure 2.5b. Al-6061 processed with 5 HPT turns was reported to have a higher fraction of HAGBs than LAGBs [33]. Occurrence of HAGBs during severe plastic deformation can be attributed to grain subdivision [45]. At low and medium strains, there is break up of grains into cells and cell blocks [3, 46]. This substructure evolves into a lamellar structure as the strain increases. During this process, there is generation of new HAGBs. This occurs through a simultaneous action of microstructure and texture mechanisms [46]. The microstructural mechanism starts at low deformations and involves accumulation of dislocations in the cell and cell block boundaries, which results in increase in the angle of misorientation of the boundaries with increase in strain. This mechanism results in formation of grain boundaries with misorientation in the range of 15^o-30^o. The texture mechanism occurs at high strains and involves rotations of the subdivided grains into different directions. This results into grain boundaries with misorientation in the range of 20^o-60^o [3, 46].

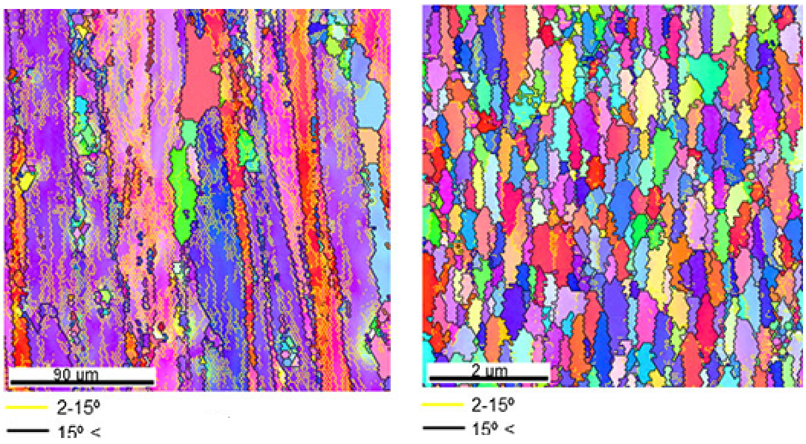

(a) Unprocessed sample (b) Processed sample for N=5

Figure 2.5: OIM images showing evolution of HAGBs of Al-7075 after HPT [20]

HPT results in formation of exceptional microstructures in complex aluminium alloys, which cannot be achieved through other processing techniques. For instance, HPT processing of cast Al-11%Fe resulted in formation of a nanocrystalline structure within the Al-matrix with dispersion and dissolution of second phase particles, refinement of the grain sizes into nanodimensional range and partial amorphization [47]. The solubility of solid iron in aluminium matrix was extended to 2.2%Fe and this resulted into formation of a supersaturated iron solid solution. As such, post-HPT aging and subsequent hardening of the conventionally non-hardenable Al-Fe alloy was possible [47]. Extension of solubility of Fe and dissolution of second phase particles such as $Al_{13}Fe_4$ was also observed in Al-7.5%Fe and Al-16%Fe alloys [48]. Solubility of second phase particles was also enhanced by HPT processing of Al6% Zn2.8% Mg1% Cu0.37% Zr alloy [49]. Similar results were also reported for Al-1.5%Zr alloy in which the microstructure was found to contain a single-phase of aluminium solid solution supersaturated with dissolved phases such as aluminides [50]. There is usually formation of poorly delineated curved and wavy grain boundaries on HPT processing of these allys. This has been attributed to presence of defects within the grain boundaries, which give rise to internal stresses during HPT [47, 48].

2.4.3 Microstructure of HPT-processed aluminium-silicon alloys

HPT results in breakdown and evolution of second phase particles in Al-Si based alloys into submicrometer range. For instance, it was reported that eutectic coral-shaped silicon particles in as-cast Al-7%Si-0.3%Fe-0.02%Na alloy with average particle size of 15 μm were transformed into small silicon particles with average particle size of 5 μm after 5 turns of HPT as shown in Figure 2.6 [19]. The study also reported homogenous distribution of Si particles within the aluminium matrix after HPT (Figure 2.7). Near the edges of the sample, new and small Si nanoparticles (<0.1 μm) around coarse Si particles in particle-free zones were observed at high magnification using electron imaging. The presence of these new Si particles was attributed to grain growth due to temperature rise (estimated to about 120-140K) during HPT [19]. The presence of particle-free zones and formation of new and small Si particles was also observed for a two-phase Al-7%Si alloy [18]. However, the formation of new Si particles was not attributed to grain growth in this case since temperature rise during HPT was shown to be insignificant to cause nucleation and grain growth [51–53]. The results of these two studies were therefore in conflict.

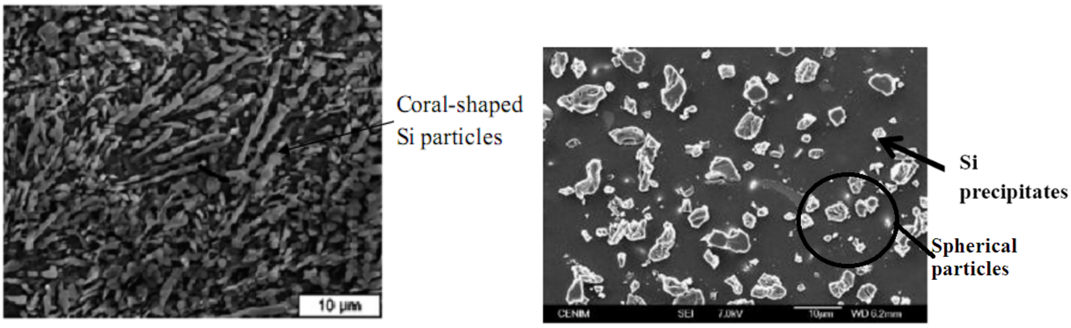

(a) Deep etched unprocessed sample (b) HPT processed sample

Figure 2.6: SEM micrograph of Al-7%Si-0.3%Fe-0.02%Na illustrating breakdown of long Si corals after 5 HPT turns [19]

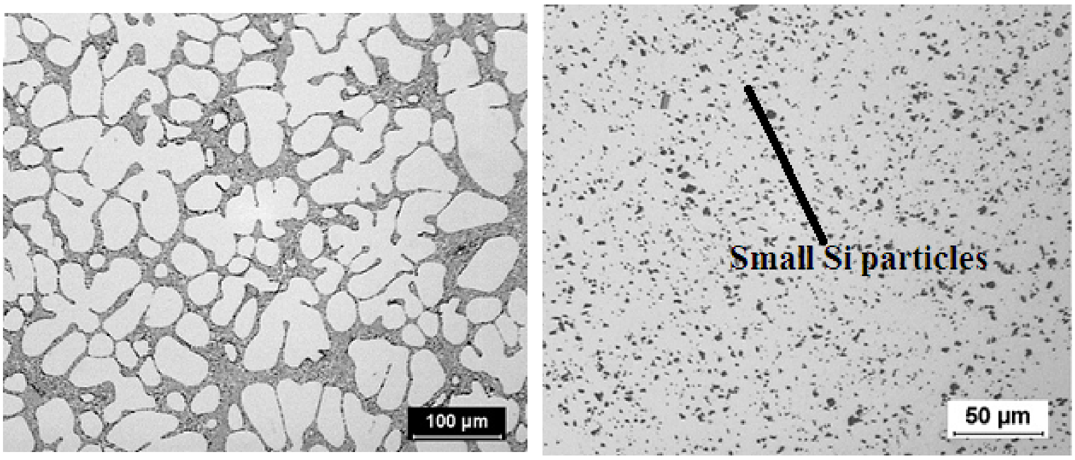

(a) As-cast alloy (b) HPT processed alloy

Figure 2.7: Optical micrographs of Al-7%Si-0.3%Fe-0.02%Na showing homogenous distribution of small Si after 5 HPT turns [19]

Through a validated FEM-model, a master plot showing temperature rise within HPT work piece for several alloys including Al was developed to resolve this conflict [51]. From this model, it was shown that the maximum temperature rise, which can occur during HPT is $\sim 15^o$ [18]. Such temperature rise cannot have a significant role in nucleation and growth of small Si particles observed in studies [18, 19].

Therefore, new and small Si particles can be attributed to breakdown of large Si particles and dispersion within the Al matrix due to subsequent plastic deformation during HPT [18].

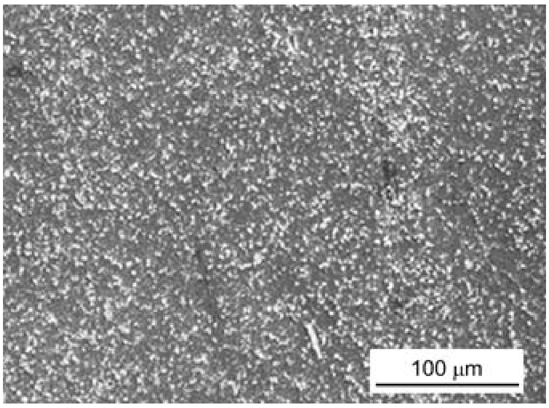

Figure 2.8: SEM micrograph showing evolution into small and new Si in HPT processed Al-7%Si, N=10 [18]

There is evolution of coarse structures into spherical or circular particles during HPT of Al-Si alloys. Such particles reduce regions of high stress concentration during loading and hence enhances performance of the material. These observations were reported for Al-2%Si-0.25%Sc alloy in which there was breakdown of the network of Si particles in the as-cast sample shown in Figure 2.9a into evenly distributed small spherical Si particles throughout the Al matrix shown in Figure 2.9b [21]. Fine and evenly distributed Si particles were also reported in cast solid and chips of AlSi8Cu3 (A380 alloy) after 10 turns of HPT [54]. As illustrated in Figures 2.6b, 2.7b and 2.8, most of the new and small Si particles exhibited spherical or near-spherical morphology after HPT.

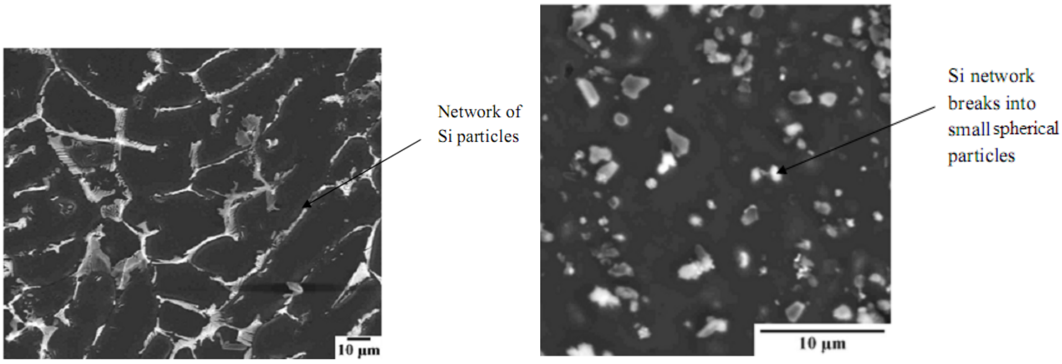

(a) Unprocessed sample (b) HPT processed sample

Figure 2.9: SEM micrograph showing breakdown of Si network of Al-2%Si-0.25%Sc after HPT [21]

HPT processing of complex Al-Si alloys results in formation of non-equilibrium and disordered structure. For instance, a comparison between the structure of Al-2%Si and Al-2%Si-0.25%Sc alloys revealed important differences [21]. It was shown that the structure development during HPT of Al-2%Si alloy is similar to that of aluminum with dislocation cell formation and a recovered microstructure. On the contrary, Al-2%Si-0.25%Sc alloy consisted of a non-homogenous microstructure with grains having non-equilibrium boundaries and dislocations. Transmission electron microscope (TEM) observations of these alloys revealed clearly defined boundaries in Al-2%Si alloy after 2 turns and dislocation networks within the grains and grain boundaries with high angles of misorientation in Al-2%Si-0.25%Sc alloy after 5 turns [21]. The study further reported that addition of 0.25%Sc into Al-2%Si alloy results in stabilization of the grain boundaries after HPT due to formation of the Al_3Sc precipitates and as such, there was no recovery of the structure as observed in Al-2%Si alloy. Similar observations of non-homogenous and non-equilibrium grain boundary structure with dislocation tangles were reported for $AlSi_8Cu_3$ alloy [54].

Deformation-induced precipitation is responsible for extra grain refinement in supersaturated solid solution Al-Si alloys. Cepeda Jimnez et al [55] compared the microstructural evolution of Al-7%Si-0.3%Fe in three different silicon supersaturation contents (1.6%Si, 1.1%Si and 0.7%Si). It was reported that the lower the initial Si solid solution in Al-7%Si-0.3%Fe alloy, the larger the grain size after HPT. This is because low solid solution results in precipitation of a smaller number of precipitates, which produces smaller pinning/dragging effect on the dislocations such that recovery and grain growth can occur. Precipitates block dislocations and grain boundaries for HPT processed alloys such that recovery and grain growth do not occur, therefore enhancing achievement of fine grains after HPT [21, 55].

It was also reported [55] that low initial Si solid solution enhance formation of homogenous structure during HPT. However, a bimodal structure (one region with UFGs and the other with coarse grains next to large eutectic silicon particles) was observed for high initial Si solid solution alloys. HPT produces high dislocation density near the eutectic Si due to high strain gradients. As such, due to dislocation motion, Si atoms diffuse towards the large eutectic Si creating particle-free zones. There is therefore decrease in pinning effect on the grain boundaries, which leads to dynamic recovery enhancing formation of coarse-grained microstructure near the large eutectic Si particles. The diffusion of Si atoms decreases as the recovery occurs. This is why UFG structures could be observed in regions where solid solution was sufficient to induce deformation precipitation during HPT. Bimodal structures were also observed for other Al-Si alloys consisting of coarse-grained structure at central core and UFG structures at the periphery; these have been attributed to strain variation along the diameter of the HPT samples [18,19,21,54]. However, for simple alloy systems such as two-phase Al-Si alloys, the bimodal structure diminishes with the increase in number of turns and pressure [18,19,54].

2.4.4 Microhardness of pure aluminium and Al-Si based alloys

Microhardness values are used to characterize the mechanical properties of HPT-processed materials [56]. Microhardness correlates directly with the wear properties of a material. Furthermore, other properties such as ultimate tensile strength and yield strength can be predicted from microhardness values [57]. Since microhardness depends on the microstructure, it is used to evaluate homogeneity in grain refinement as well as the effect of HPT on the material.

Microhardness in pure Al increases on HPT processing has been reported [36,56, 58]. During early stages of HPT processing, the microhardness values at the central core are usually higher than at the edges and on further increase in HPT turns, the microhardness at the edges remains nearly constant while that at the central region lowers leading to microhardness homogeneity. For example, higher microhardness was reported at the center of the sample for up to 1 HPT turn [36, 58]. Figure 2.10 shows that microhardness is higher at the center for $\frac{1}{8}$, $\frac{1}{4}$, $\frac{3}{4}$ and $\frac{7}{8}$ turns while above 1 turn, the microhardness decreases in the center. This means that microhardness homogeneity in pure Al occurs through softening [56].

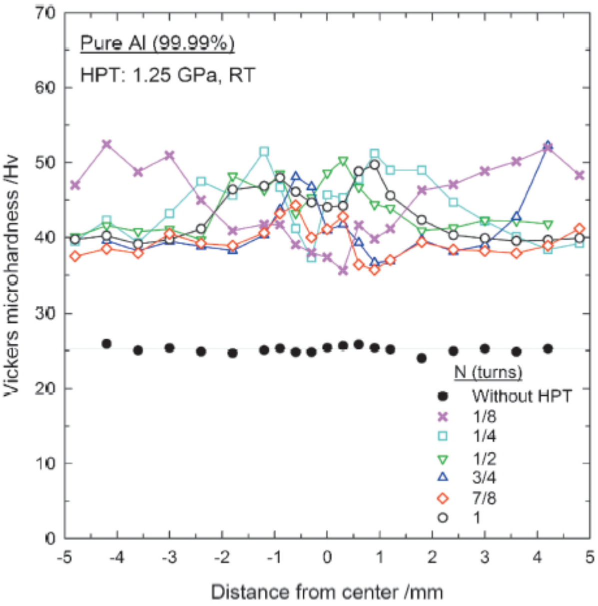

Figure 2.10: Variations of the average Vickers microhardness values as a function of the distance from the center of the high-purity Al disks after HPT atP=1.25 GPa for $\frac{1}{8}$,$\frac{1}{4}$,$\frac{1}{2}$,$\frac{3}{4}$, $\frac{7}{8}$ and 1 turns: the dotted line shows the average hardness in an annealed condition without processing [36]

This behavior has been explained by considering the microhardness variation with equivalent strain for pure Al shown in Figure 2.11.

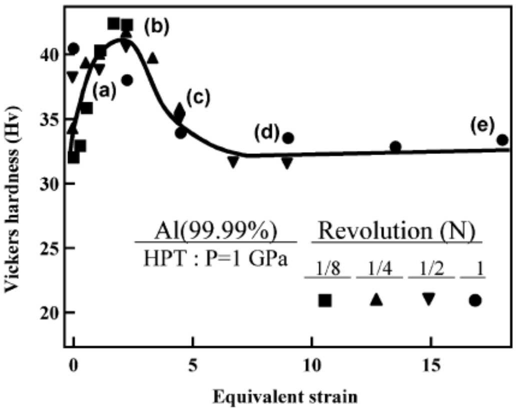

Figure 2.11: Microhardness-strain ϵ relationship for HPT pure aluminium [58]

As shown in the Figure 2.11, the microhardness increases rapidly to a maximum at low strains followed by a decrease to a saturation microhardness with increase in strains. This microhardness model is exhibited by materials which achieve microhardness homogeneity through softening with rapid recovery on HPT [36, 56, 58]. This behavior is attributed to high stacking fault energy which enhances easy cross-slip and rapid microstructural recovery in pure Al [36, 55, 58]. The rapid increase in microhardness at low strains is attributed to increase in dislocation density and formation of sub-grain boundaries such that there is blockage of dislocations. The rapid decrease in microhardness is attributed to annihilation of dislocations at the grains. The annihilation of dislocations in grains is enhanced by a strain-dependent level of long-range internal stresses during HPT [59]. Furthermore, increase in strains increases the misorientation angles of boundaries which results in build up of dislocations [58, 59]. In the saturation region, there is balanced generation and annihilation of dislocations within the grains.

Microhardness in Al-Si alloys increases on HPT processing and varies significantly along the diameter of the sample with the lowest microhardness at the centre [18, 21]. This is because the lowest Von Mises equivalent strains occur at the center of the samples as depicted by equations (2.2)-(2.4). This variation reduces with increase in number of HPT turns for Al-Si alloys until homogeneity is achieved (Figure 2.12) [18, 21]. This means that most Al-Si alloys evolve towards homogeneity through strain hardening with or without recovery. Simple Al-Si alloys achieve microstructural homogeneity (saturation) since they do not undergo recovery during HPT. Their microhardness behavior is shown in Figure 2.13a. Multi-phase Al-Si alloys such as Al-2%Si-0.25%Sc and $AlSi_8Cu_3$ do not achieve microstructural saturation after HPT due to slow recovery [21,54,55]. The microhardness behavior of such alloys is shown in Figure 2.13b.

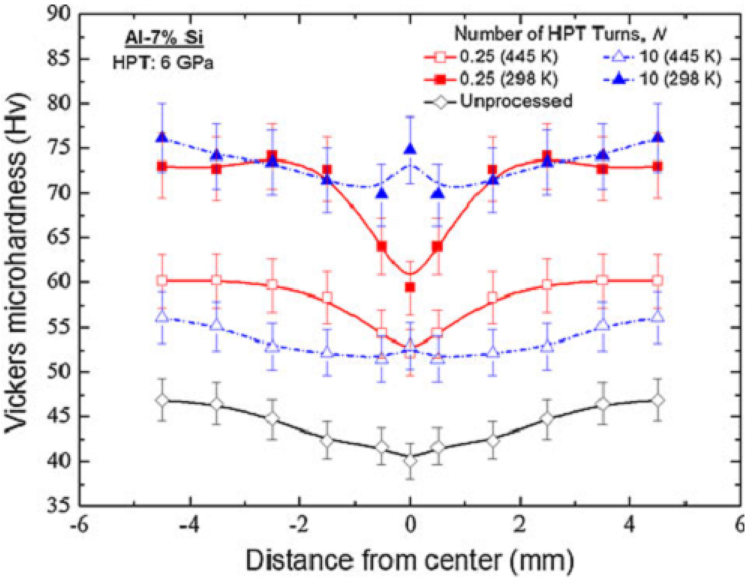

Figure 2.12: Microhardness of an HPT processed Al-7%Si alloy as a function of distance from the centre for different number of turns [21]

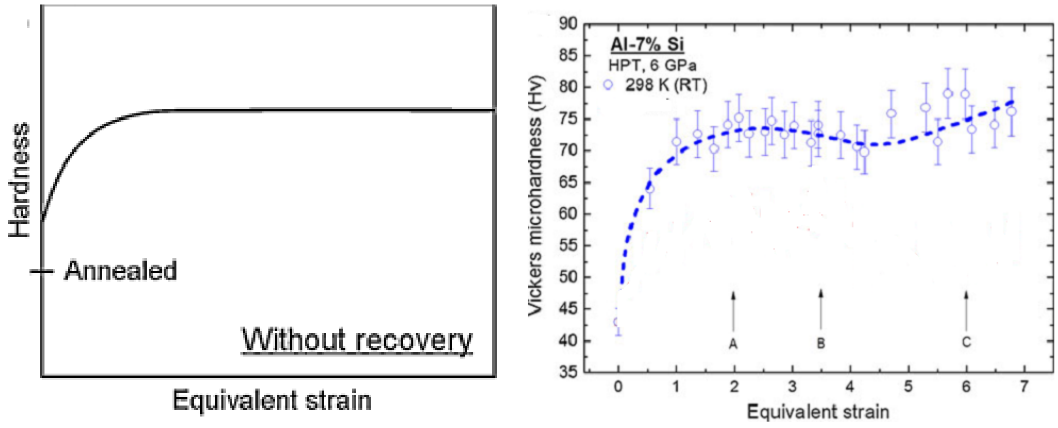

(a) Without recovery

(b) With slow recovery

Figure 2.13: Microhardness-strain relationship models for Al-Si alloys [21, 56]

As shown in Figure 2.13b, microhardness in some Al-Si alloys exhibits non-monotonic relationship with strain; increases, decreases and then increases with strain. The increase is attributed to grain refinement while the decrease to slow recovery during HPT. Such alloys are difficult to achieve microhardness homogeneity since the cycle of grain refinement-recovery-grain refinement may continue to reoccur.

2.5 Review of Microhardness measurement methods

Microhardness testing of HPT samples is not a straightforward procedure due to the small size of the samples. A single microhardness measurement is not an accurate representation of microhardness of the material. Various methods have therefore been employed in microhardness measurement of HPT samples that provide better representation of the hardness distribution in the material [11, 18, 60]. These methods are briefly described in the next subsections.

2.5.1 Method 1

Figure 2.14 illustrates a method of carrying out microhardness measurement across the diameter of an HPT processed sample. Points denoted by O in Figure 2.14 (0.3 mm from each other) are selected across the radius of the sample. For each point (O), microhardness measurements are taken at four points (⊕) located at 0.15 mm from point O [60]. The microhardness at O is the average of the local microhardness values at the four ⊕ points.

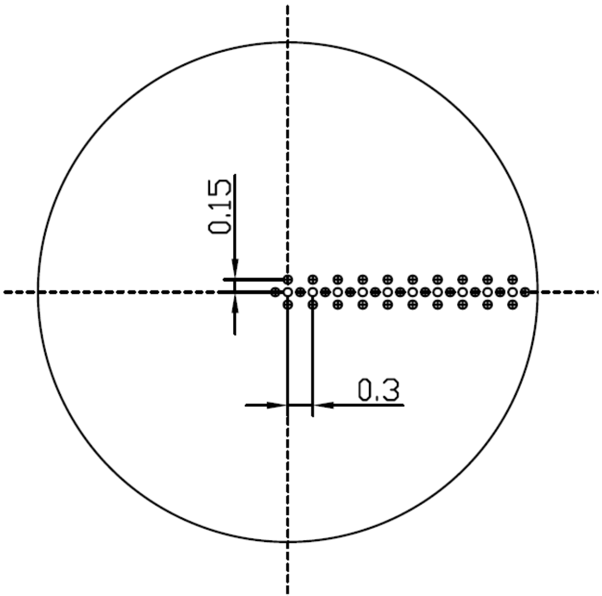

Figure 2.14: Microhardness measurement across the diameter of HPT sample [60]

2.5.2 Method 2

Figure 2.15 illustrates the procedure for determining microhardness profile over the surface area of the HPT sample. The microhardness is measured at various equidistant points selected over the surface of the sample (⊕).

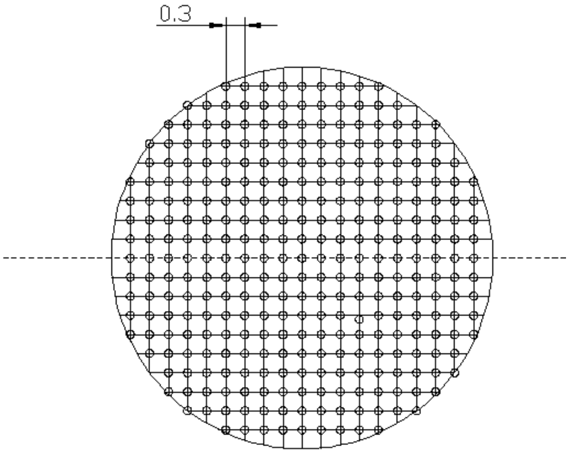

Figure 2.15: Microhardness measurement across the surface of HPT sample [60]

2.5.3 Method 3

For statistical accuracy, the method illustrated in Figure 2.16 is used [18]. For diameter A, the points ⊕ are 0.9 mm from each other. For diameters B, C and D the points ⊕ are at ±1.25, ±2.25, ±3.25 and ±4.25.

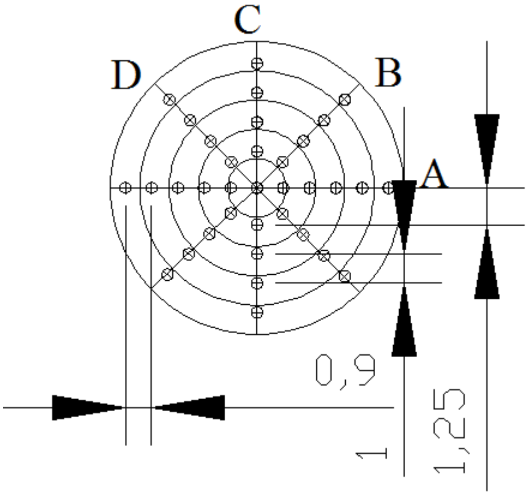

Figure 2.16: Procedure for measuring values for generating microhardness line profiles [18]

The microhardness at each point ⊕ is determined by averaging microhardness measurements taken at four points located at 0.3 mm around the point ⊕ [18]. To determine microhardness as function of radius, circles are drawn at r=1 mm, 2 mm, 3 mm, and 4 mm, thereby creating five annular rings. Within each ring, the microhardness values represented by points ⊕ are averaged. The value obtained is assigned to mid-radius of the annular ring. In this method, each microhardness value is an average of 40 values except at r=0 where the value of microhardness was an average of four values.

2.5.4 Method 4

For surface representation of microhardness across the diameter, a method shown in Figure 2.17 is used. Measurements are taken at various points 1.25 mm from each other (O) along eight diameters 45^o from each other. The microhardness of

O, is the average of values of four points ($\oplus$) located at 0.3 mm from O except for the points located at the edges [11]. Each average microhardness value can be read against X-Y scale and plotted as surface profile.

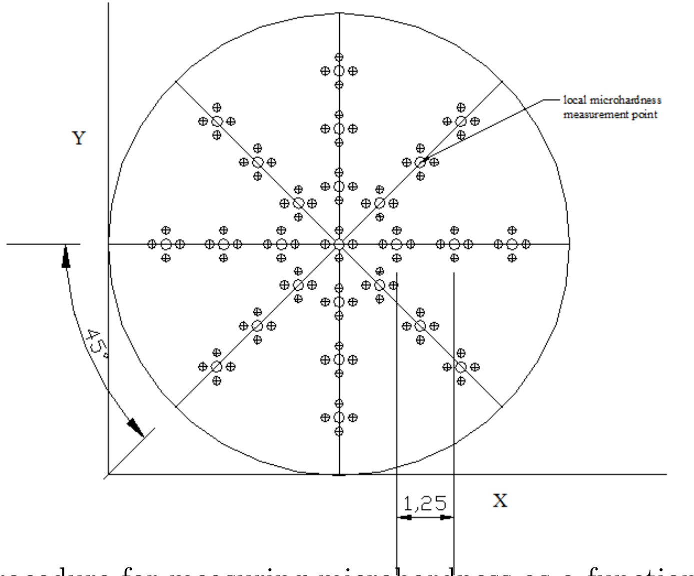

Figure 2.17: Procedure for measuring microhardness as a function of X-Y scale

The choice of method to employ in microhardness measurement depends on its simplicity, effectiveness and accuracy. For instance, although method 1 is practically the easiest for generating microhardness line profiles, measurements are taken in one direction of r as shown in Figure 2.14 and the other direction assumed to have the same microhardness values.

On the other hand, method 2 illustrated in Figure 2.15 is used in measurement of local microhardness over the entire surface of the sample. It is used in generating microhardness contour maps and microhardness meshes to provide pictorial variation of the microhardness, and hence microstructure, across the sample surface.

However, the method is inaccurate since it considers a single microhardness value for each point $\oplus$ and cannot be relied upon to provide accurate representation of microhardness distribution.

Method 3 shown in Figure 2.16 is the most statistically accurate for generation of line profiles since each point along the diameter is an average of 40 microhardness values. However, it is practically complex and prone to practical errors. The method has only been used by Mungole et al [18].

Method 4 illustrated in Figure 2.17 has been widely used in generation of both microhardness line and area profiles across the surface of the sample [10, 11]. This method is less complex and therefore less practical errors are involved (compared to method 3). The method is more accurate than method 2 since each hardness value is an average of four values. However, the method uses few points along the diameter of the sample, which cannot be sufficient representative of the sample.

2.6 Summary

Although the effect of HPT processing on the structure and hardness of Al-Si alloys, such as Al-2%Si, Al-7%Si, $AlSi_8Cu_3$, Al-7%Si-0.3%Fe-0.02%Na, Al-7%Si-0.3%Fe and Al-2%Si-0.25%Sc were previously reported, little has been done on the effect of imposing a very high strain (during HPT) on the evolution of structure and hardness in Al-Si piston and other complex multicomponent alloys. These are particularly important materials to study due to their application as piston materials. Furthermore, the currently published results are for relatively simple Al-Si systems. It has also been shown that different particles and intermetallic phases in aluminium alloys evolve differently during HPT. However, most of the previous reports on HPT-processed Al-Si alloys described the evolution of Si particles without considering other particles such as Cu-bearing phases in $AlSi_8Cu_3$, Fe-bearing phases in Al-7%Si-0.3%Fe-0.02%Na and Al-7%Si-0.3%Fe and Sc-bearing phases in Al-2%Si-0.25%Sc alloys. Therefore, there is little information on the evolution of intermetallic particles during HPT of Al-Si alloys. Additionally, most of the Al-Si alloys previously processed were undertaken up to 10 turns. There is need to process Al-Si alloys beyond 10 turns to evaluate further evolution of the structure. Another gap identified from this research is that HPT has not been used to process secondary Al-Si alloys to evaluate whether SPD improves the properties of such alloys. This research characterizes the microstructural and microhardness evolution of HPT-processed Al-Si piston alloys up to 10 turns with emphasizes on transformation of intermetallic phases and evolution towards homogeneity.

CHAPTER THREE

3.0 METHODOLOGY

3.1 Introduction

This chapter describes the materials, equipment and methods used in the research.

3.2 Materials

Tables 3.1 and 3.2 show the composition (%Wt) of primary and secondary piston alloys studied in this work. The alloys were previously investigated for their fatigue and other mechanical properties [61–63] due to their application as engine materials. The primary cast Al-Si piston alloys were supplied by Federal Mogul (FM), UK. The primary alloys had been prepared by casting followed by quenching in water. The alloys were then aged for 8 hours at 230^{o}C after which they were

Table 3.1: Composition of cast primary alloys

	wt.%									**ppm**	
Alloy	**Si**	**Cu**	**Ni**	**Mg**	**Fe**	**Mn**	**Ti**	**Zr**	**V**	**P**	**Sr**
A	12.45	3.93	2.78	0.67	0.44	0.03	0.01	0.05	0.04	55	0
B	6.9	3.89	3	0.62	0.22	0.03	0.01	0.05	0.04	45-50	0
C	6.9	3.89	3	0.62	0.22	0.03	0.01	0.05	0.04	45-50	150-155

Table 3.2: Composition of cast secondary alloy

	wt.%												
Alloy	**Si**	**Cu**	**Ni**	**Mg**	**Fe**	**Mn**	**Cr**	**Ti**	**Sn**	**Zn**	**P**	**Sr**	**Al-5Ti-1B**
Base alloy (P)	10.6	1.36	1.08	0.78	1.06	0.08	0.03	0.06	0.02	0.09	0.04	0	0

air-cooled. The chemical compositions of the primary alloys are shown in Table 3.1.

The recycled cast Al-Si piston alloys herein referred to secondary alloys were obtained by melting piston scrap in a 70Kg capacity oil fired graphite crucible furnace at Jomo Kenyatta University of Agriculture and Technology (JKUAT) foundry laboratory. The piston scrap was charged into the furnace and heated to a temperature of 730^{o}C under a flux cover. The melt was skimmed off before pouring and then transferred into 4Kg capacity ingot moulds fabricated from mild steel sheets. On complete cooling, the ingots were removed from the moulds. Samples for chemical analysis were poured into copper moulds, which were then immediately quenched in cold water to avoid compositional segregation. The chilled samples were sent to LSM, UK for compositional analysis. The chemical composition of the recycled (secondary) alloy used in this work is shown in Table 3.2

3.3 Experimental procedures

3.3.1 HPT processing

HPT processing of these samples was carried out at the University of Southampton, UK. Samples were sliced from cast ingots with a diameter of 10 mm and ground with abrasive papers to a thickness of 0.8-0.85 mm. The samples were then placed onto the lower anvil with a circular cavity of 10 mm diameter and 0.25 mm thickness. The upper anvil has a cavity with similar dimensions as the lower one. The HPT processing was conducted at room temperature using the HPT facility shown in Figure 3.1. Processing at room temperature has been shown to enhance mechanical properties since recrystallization does not occur [18]. The edges of the anvils were lubricated using MoS_2 to reduce friction between anvil edges since very high friction results in sticking of the sample onto the anvil. Lubrication therefore ensures heterogenous deformation does not occur [64, 65].

After the disc samples were fitted in the cavity of the lower anvil, the lower anvil moved upward and imposed high pressure to the samples by pressing against the upper anvil. Then, the lower anvil was rotated at a speed of 1 revolution per minute (rpm) while maintaining the compression force, so that a high-pressure straining was imposed to the disc sample. A low rotational speed of the lower anvil was chosen because higher speeds result into higher deformation rate, which consequently result into heating of the sample [51]. A pressure of 3 GPa was chosen since it has been previously reported that very high imposed pressure results in generation of very high heat and therefore optimum compressive pressure should be chosen to ensure there is no heating [51].

For Al alloys, it has been shown [51, 64] that pressures slightly above 2.5 GPa are sufficient for optimum HPT processing, hence the choice of 3 GPa. Furthermore, HPT processing was conducted under quasi-constrained conditions since through finite element modeling of high-pressure torsion, it has been confirmed that quasi-constrained processing enhances high deformation during HPT [51,64,66]. Quasi-constrained condition was achieved by leaving a small gap of ∼0.3 mm between the upper and lower anvil of the facility during HPT processing.

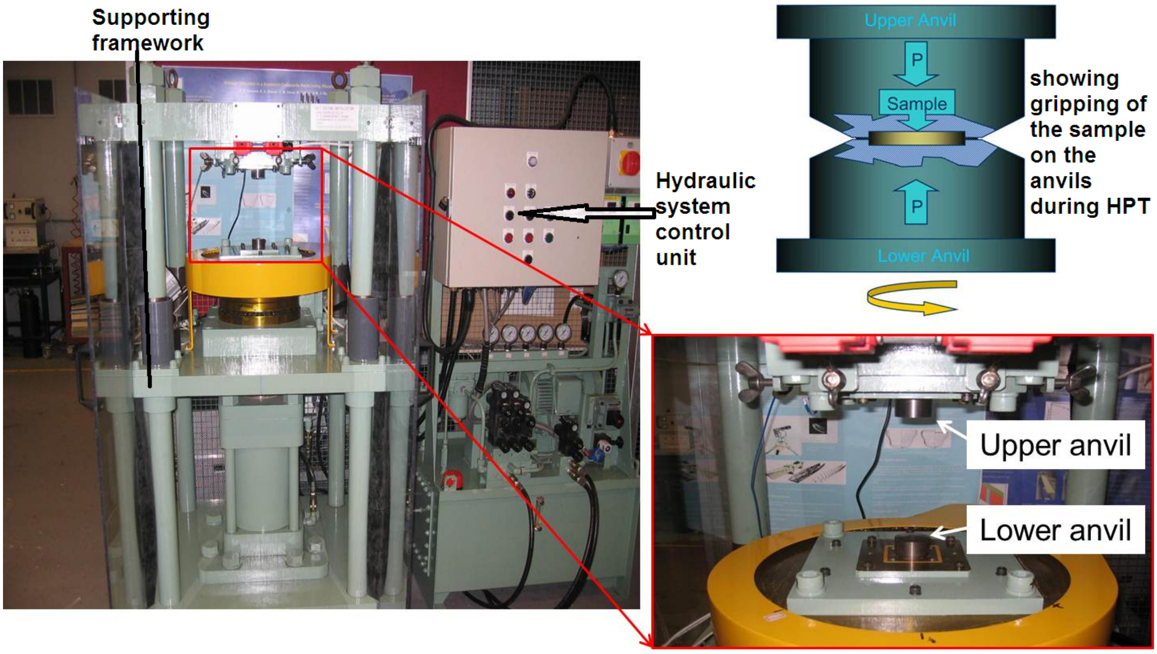

Figure 3.1: A photograph of the HPT facility used for this study located at the University of Southampton and an illustration of how the workpiece is positioned during HPT processing

3.3.2 Microstructure examination

Optical microscopy

Both as-received and HPT-processed samples were mounted for metallographic examination. Table 3.3 summarizes the procedure for polishing the samples for metallographic examination.

Table 3.3: Procedure for grinding and polishing samples for metallographic examination

No.	Procedure	Chemicals
1	Grinding	Silicon Carbide papers ♯800 followed by ♯1200. The samples were then washed in water, methanol and then dried
2	Polishing	Polished to mirror-like surface using Strues diamond pastes of 1 μm followed by $\frac{1}{4}$ μm. The samples were then washed and dried
3	Finishing	Polished to oxide polish suspension (0.05 μm) finish

The samples were examined using Olympus BX5 optical microscope.

Scanning Electron Microscopy (SEM)

The fully polished samples were further cleaned using an ultrasonic bath to remove any particles or suspensions on their surfaces. They were then investigated using a JEOL JSM 6500F microscope at an accelerating voltage of 15 kV. The microscope is fitted with an Oxford Inca 300 energy dispersive X-ray suite. SEM analysis was carried out using both secondary and backscatter electron modes. It is important to note that SEM was undertaken selectively for the modified Al-7%Si and the secondary Al-Si alloy due to cost and time constraints.

Image Analysis

The images were analyzed using ImageJ software to quantify the microstructural break down during HPT. ImageJ supports standard image processing functions such as contrast manipulation, sharpening, smoothing, edge detection and median filtering [67]. The procedure for undertaking the image analysis is described in details in literature [68] and is summarized in Figure 3.2. The output of this procedure was the area and circularity of particles. Circularity (C) is a measure of shape which is calculated as

$$C = \frac{4A\pi}{P^2} \tag{3.1}$$

where, A is the particle area and P is the particle perimeter. Circular shapes have circularity close to 1 and vice versa. The grain sizes could not be presented in this research since it was not possible to see grain boundaries in SEM microscope. Transmission Electron Microscope (TEM), which was not available for this research, is used in measuring grain sizes for these alloys. As such, area of structures was used to quantify the microstructure breakdown.

The data was then exported to Minitab 16 software (www.minitab.com) for distribution analysis of areas of particles. Since 3-parameter Weibull and 3-parameter lognormal distribution functions have been shown to provide a good fit for particle sizes in aluminium alloys in previous studies [69–71], the two distributions were evaluated for fit onto the current data on area of particles. From the evaluation, Weibull distribution function was shown to provide a better fit for the current data and therefore was chosen in this research (see Figures 6.1 and 6.2 in Appendix A). The probability distribution function (pdf) of the 3-parameter Weibull distribution can be written as:

$$F(x) = 1 - exp\{(\frac{x-\gamma}{\beta})^{\alpha}\}, x \geq \gamma \tag{3.2}$$

Where,

x=particle area

α=shape parameter (standard deviation)

β=scale paramenter (mean)

γ=minimum value (location parameter)

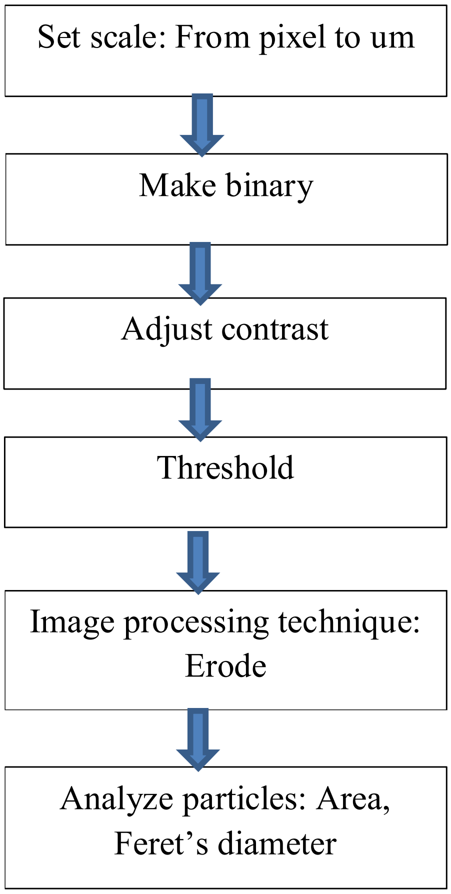

Figure 3.2: Image analysis procedure using ImageJ

3.3.3 Microhardness measurements

To undertake line profile measurements in this research, a new measurement method was developed in this work based the aspects of methods 1, 3 and 4 discussed in the literature. Unlike in method 1, the measurements were taken across the diameter of the samples. Measurements were taken on 40 local points ($\bigoplus$) across the diameter of the sample located at 250 μm from each other. Around each point ($\bigoplus$), just as in methods 3 and 4, measurements were taken on four other points (O) located at 125 μm from the $\bigoplus$ point. The microhardness of each point ($\bigoplus$) was determined by taking the average of the five microhardness values (one at point $\bigoplus$ and four at O points). In this way, at least 150 readings were recorded for each sample. This method is more accurate than methods 1 and 4 and simpler than method 3 and it is illustrated in Figure 3.3.

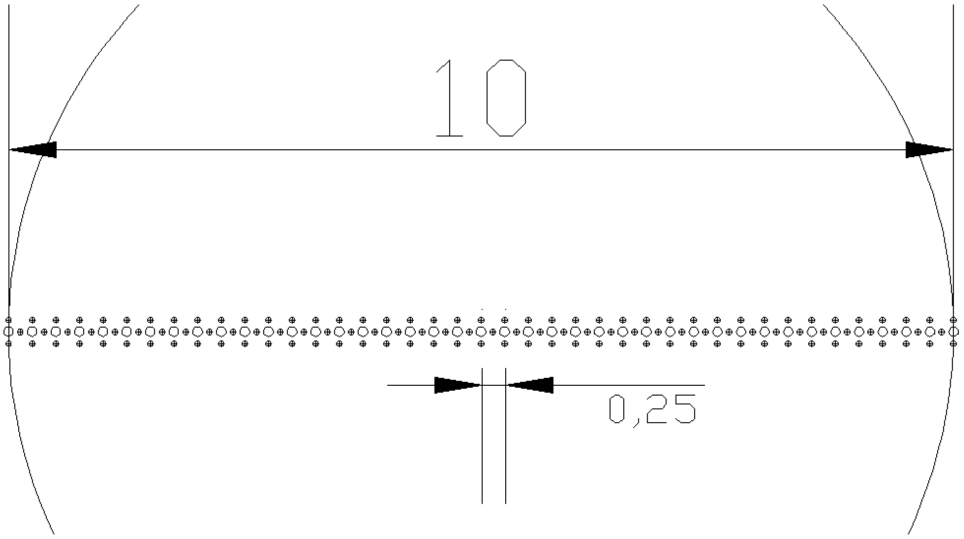

Figure 3.3: Showing line profile microhardness measurement procedure developed for this research

The applied load of 300g was used at a dwell time of 10s during measurement.

CHAPTER FOUR

4.0 RESULTS AND DISCUSSIONS: PRIMARY Al-Si PISTON ALLOYS

4.1 Introduction

This chapter presents the results and discussion of microhardness and microstructure of primary Al-Si piston alloys. The three primary alloys studied are Al-12%Si, unmodified Al-7%Si and modified Al-7%Si piston alloys denoted as A, B and C respectively in Table 3.1.

4.2 High-pressure Torsion Processing of Al-12%Si Piston Alloy

4.2.1 Properties of the As-received Al-12%Si piston alloy

Microstructure

The intermetallic particles have been identified from literature since it is not possible to do so through an optical microscope. Using an optical micorscope, the microstructure was observed to contain large blocky primary Si and small eutectic Si particles as indicated in Figure 4.1. Based on the literature, some of the common intermetallic particles present in this alloy include AlCuNi, Al_9FeNi, Mg_2Si

and Al_2Cu [61]. AlCuNi and Al_9FeNi usually exhibit large and blocky morphology whereas Mg_2Si and Al_2Cu have Chinese script morphologies [61].

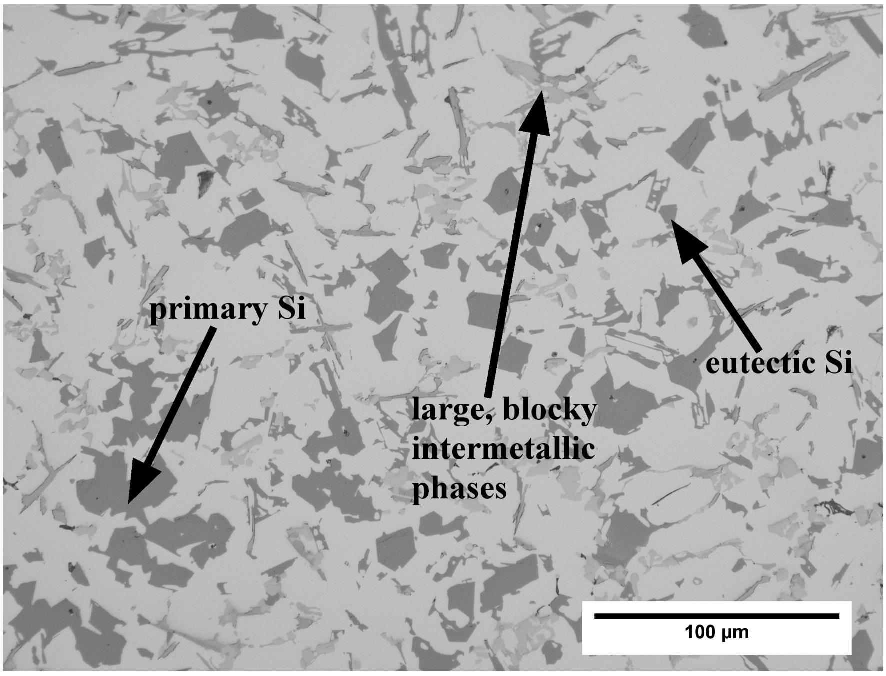

Figure 4.1: Optical micrograph showing various phases in unprocessed Al-12%Si piston alloy

Microhardness

Figure4.2 shows the average microhardness and scatter bars along the diameter of the Al-12%Si sample. The microhardness is not uniform as theoretically expected. This is due to the complex nature of the microstructure shown in Figure 4.1.

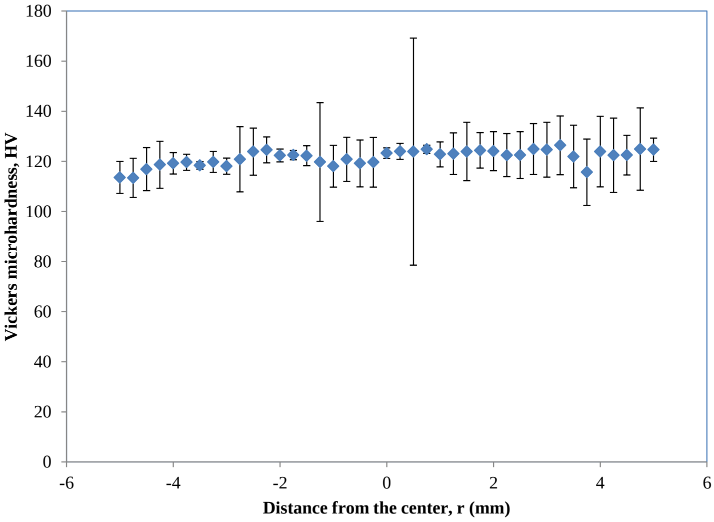

Figure 4.2: Vickers Microhardness across the diameter of unprocessed Al-12%Si sample

4.2.2 Microstructural evolution

Figure 4.3 shows the optical micrographs after $\frac{1}{4}$, $\frac{1}{2}$, 1 and 10 HPT turns during HPT of Al-12%Si piston alloy. Figures 4.4 and 4.5 show microstructure after 1 and 10 turns at higher and lower magnifications respectively. After $\frac{1}{4}$ turn, Figure 4.3a, there is no observable microstructural change at the central region. This is because the minimum strain occurs at the central region as revealed by the strain model. However, small Si particles can be observed at the edge as seen in Figure 4.3b. These particles originate from break down of primary Si. Fragments of intermetallic phases can also be observed. The breakdown at the edge is because of the presence of maximum strain.

Large and blocky Si particles are still visible at the central region after $\frac{1}{2}$ HPT turn (Figure 4.3c). However, there are broken phases observed. This means that intermetallic phases in Al-12%Si alloy start to break down after $\frac{1}{2}$ turn at the central region. There is no microstructural transformation at the edge after $\frac{1}{2}$ turn (Figure 4.3d).

There are cracked intermetallic phases present at the central region after 1 turn as indicated in Figure 4.3e. However, there are unbroken Chinese-script phases present at the center. This observation can be confirmed by a higher magnification optical micrograph given in Figure 4.4. These observations confirm that break down is still insignificant at the central region even after 1 turn. At the edge, Figure 4.3f, considerable break down of intermetallic phases can be observed although there are still both unbroken primary Si and intermetallic phases still present.

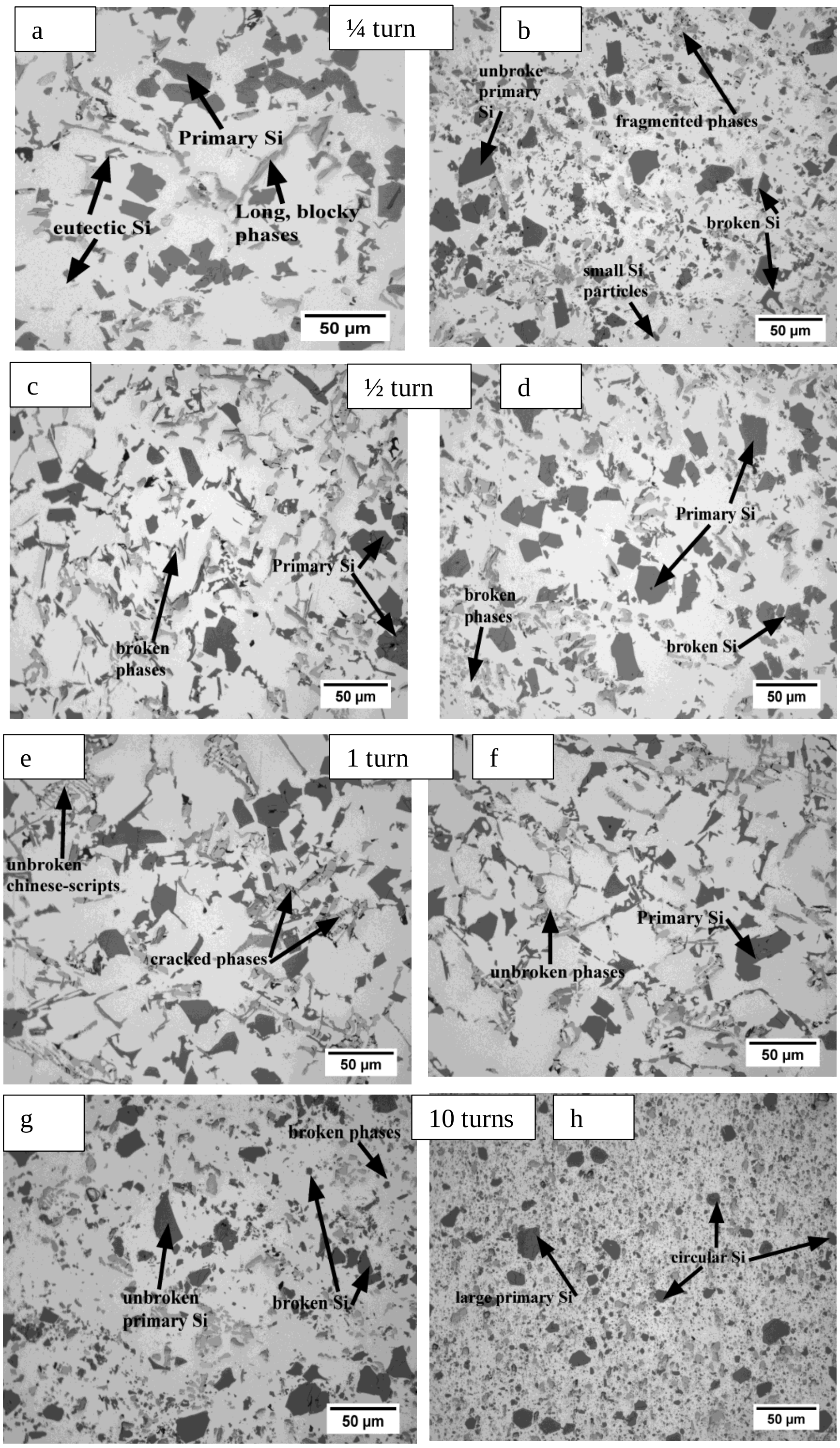

Figure 4.3: Optical micrographs showing microstructural evolution during HPT of Al-12%Si alloy at different number of turns. Images a, c, e, g represent the microstructure at the central region while images b, d, f, h represent the microstructure at the edges.

After 10 turns, more break down of intermetallic phases can be observed although unbroken primary Si is widely present at the central region (Figure 4.3g). This is because Si particles are stronger than the other phases. At the edge, the microstructure appears equiaxed with most of intermetallic phases broken and redistributed throughout the Al matrix. An interesting observation to note is the presence of small and circular Si particles as shown in Figure 4.3h. This observation will be described under subsection 4.2.4. Large primary Si particles are still present after 10 turns.

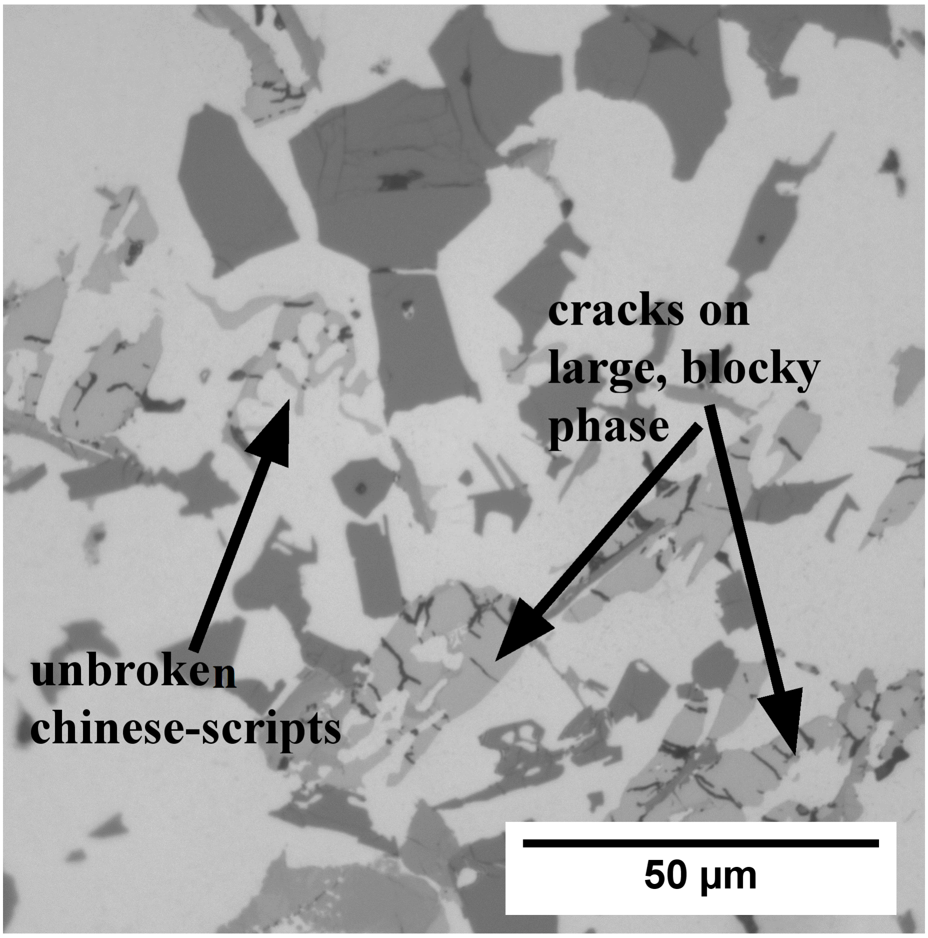

Figure 4.4: Optical micrograph at the central region of Al-12%Si sample showing cracks on intermetallic phases after 1 HPT turn

Figure 4.5 shows a 'whirlpool' pattern with distinct shear lines observed around the central core after 10 HPT turns. These patterns confirm that full and homogeneous deformation has not occurred after 10 turns. Similar patterns were reported for pure Al at 5 turns and two-phase alloys at low number of turns [72].

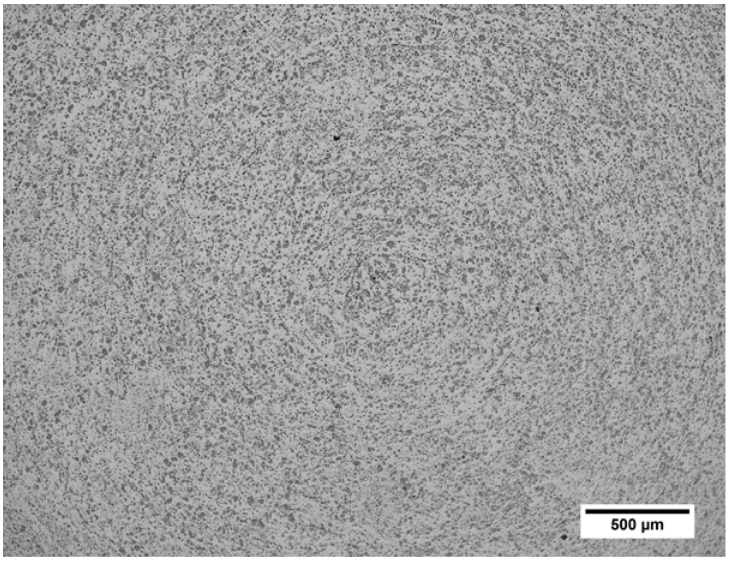

Figure 4.5: Optical micrograph of Al-12%Si showing whirl pattern after 10 turns at the centre

4.2.3 Microhardness evolution

Figure 4.6 shows the microhardness line profiles (with scatter bars) for an Al-12%Si piston alloy sample after $\frac{1}{4}$, $\frac{1}{2}$, 1 and 10 HPT turns. The microhardness for the as-received cast Al-12%Si piston alloy is also shown for comparison. After $\frac{1}{4}$ turn, the microhardness has increased by 20% and 70% at the centre and edge respectively from initial values of the as-received alloy . This is due to higher refinement at the edge than at the center as observed in the microstructure analysis (Figures 4.3a and 4.3b in subsection 4.2.2). The average microhardness has increased non-uniformly along the diameter. From the centre to r∼±1 mm, the microhardness is nearly homogeneous. Then it increases linearly up to r∼±2.5 mm beyond which it becomes nonlinear on both sides of the diameter.

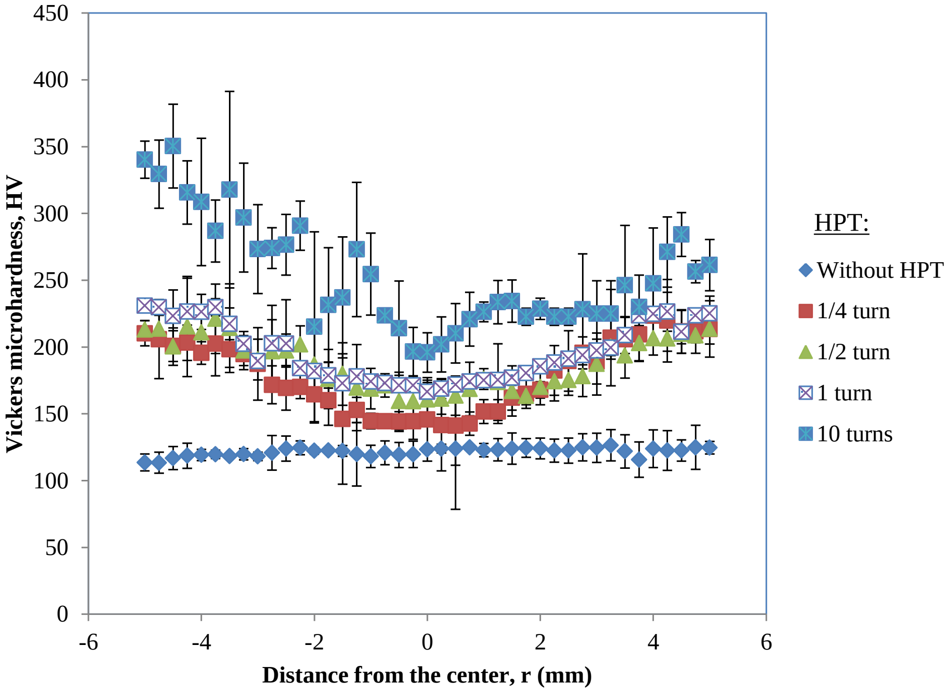

Figure 4.6: Vickers microhardness as function of distance from the centre of Al-12%Si alloy after $\frac{1}{4}$, $\frac{1}{2}$, 1 and 10 turns. The microhardness variation for unprocessed alloy and the scatter bars are also shown.

Generally, the error bars are nearly equal except at random points. This can be attributed to presence of a few broken and unbroken phases as observed in Figure 4.3b.

After $\frac{1}{2}$ turn, microhardness has increased by ∼29% and ∼71% from the initial values of the as-received samples at the central region and at the edges respectively. As shown, the size of scatter bars vary randomly along the diameter except from diameter of +1.8 mm to the edge where the size of scatter bars can be observed to be nearly equal. This indicates nonhomogeneous microstructure after $\frac{1}{2}$ turns. As seen in Figures 4.3c and 4.3d, the microstructure contains a 'mixture' of large unbroken silicon particles, broken Si and fragments of other particles. Each of these microstructural constituents exhibit different microhardness and hence the scatter in microhardness measurements.

Microhardness values have increased by ∼30% and ∼84% at centre and edges respectively from the initial values of the as-received alloy after 1 turn. The microhardness from r∼±3.8 to the edge along the diameter are nearly uniform indicating evolution towards microhardness homogeneity.

After 10 HPT turns, the homogeneity in scatter bars has decreased and their sizes increased considerably. This can be attributed to break down and redistribution of particles throughout the Al matrix. The greater microhardness gradient present after 10 turns can be attributed to the more large and unbroken Si particles observed at the central region than at the edge (Figures 4.3g and 4.3h).

It can be seen in Figure 4.6 that there is a very small difference between microhardness values for quarter and half turns especially around the central region. This is because there are no significant microstructural changes occurring between the two turns. Furthermore, the sizes of scatter bars are very large after 10 turns. This can be attributed to redistribution of Si and intermetallic particles within the matrix due to effect of high-pressure torsion. It can also be seen that the line profile after 10 turns is not symmetrical about the centre as it has been reported for other aluminium alloys processed by HPT [1, 4, 6, 7, 10–18, 20–22, 73]. This is a confirmation that homogeneous microstructural refinement in Al-12%Si piston alloy is not achieved after 10 turns.

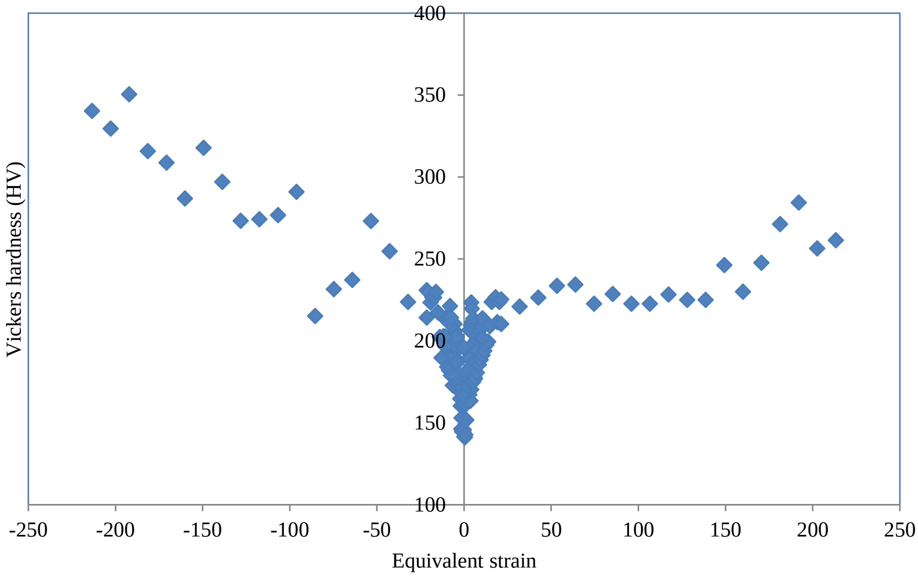

Figure 4.7: Vickers microhardness variation with equivalent strain for Al-12%Si piston alloy. It shows a non-monotonic relationship. Also note the lack of symmetry on both sides of the diameter.

Figure 4.7 shows variation of microhardness with the equivalent strain for Al-12%Si piston alloy. A very low microhardness is observed at zero equivalent strain. It can also be seen that the microhardness along Al-12%Si piston alloy exhibits a non-monotonic relationship with the equivalent strain. A similar behavior is reported in literature [18] for materials which undergo strain hardening with slow recovery such as Al-7%Si alloy.

4.2.4 Distribution of particles in HPT processed Al-12%Si piston alloy

The 3-parameter Weibull distribution function was fitted to the particle area data and the results are as shown in Figures 4.8 and 4.9. Although Weibull distribution was found to give the closest fit, significant lack of fit is still present in Figures 4.8 and 4.9 especially after HPT processing. Data for HPT-processed samples show large Anderson-Darling goodness-of-fit parameter (AD values) and P-values less than 0.005 in Figure 4.8. For close fits, AD and P values should be less than 1 and 0.005 respectively [70, 71]. The lack of fit can be attributed to particle redistribution after HPT as was seen in Figure 4.3. The figures also show that the scale parameter (β) which indicates the mean of the data is decreasing with the number of turns and along the diameter. This is consistent with the microhardness results report in Figure 4.6. The shape parameter (α), which indicates the standard deviation of the data has decreased on HPT processing. However, 10 HPT-turn gives the highest α-values than the rest of the turns. This is consistent with the scatter in microhardness measurements after 10 turns shown in Figure 4.6 and it is attributed to breakdown and redistribution of hard phases throughout the Al matrix as indicated from Figure 4.3h.

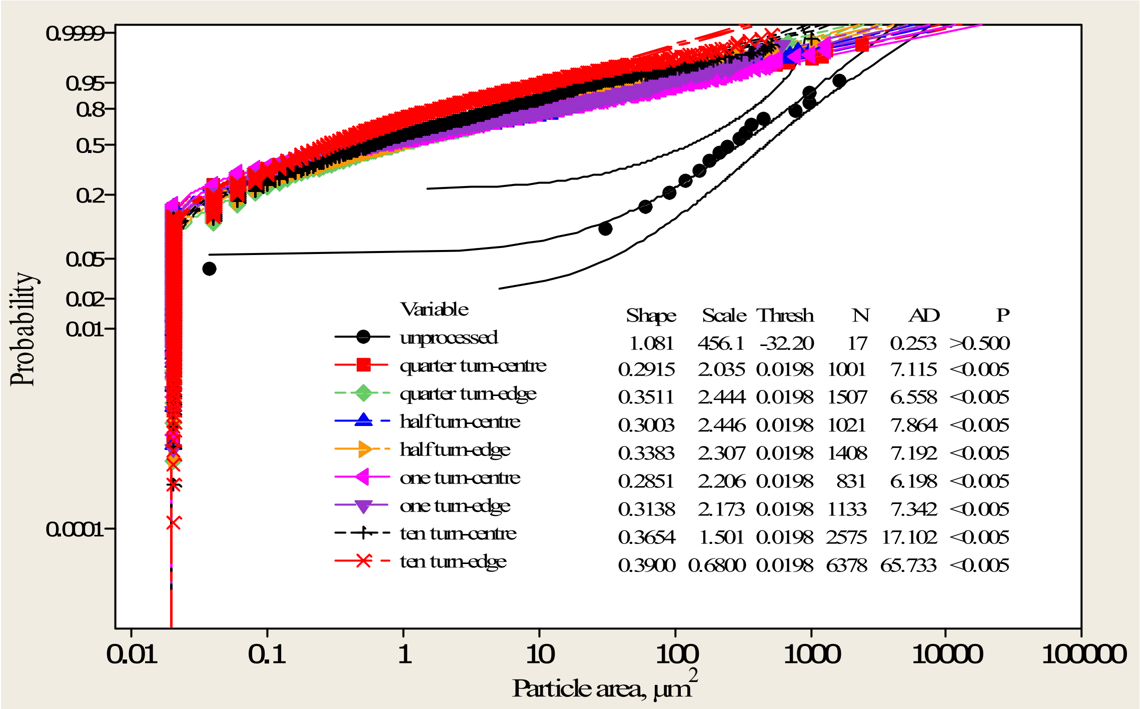

Figure 4.8: The 3-parameter Weibull probability plots of areas of particle in unprocessed and HPT-processed Al-12%Si piston alloy. The parameter, AD and P values are also shown

Figure 4.9 shows that the particle areas after 10 turns are heavily skewed towards the smaller particles. A close examination of the distribution however shows a very high particle size difference between the central region and the periphery after 10 turns. For instance, taking a percentile at 90% shows that 90% of the particles have an area less or equal to 15 μm^2 at the central region. This is very high compared to 5.8 μm^2 at the edge. This disparity in particle sizes could be the reason for the asymmetrical and non-uniform microhardness line profiles after 10 turns (see Figure 4.6).

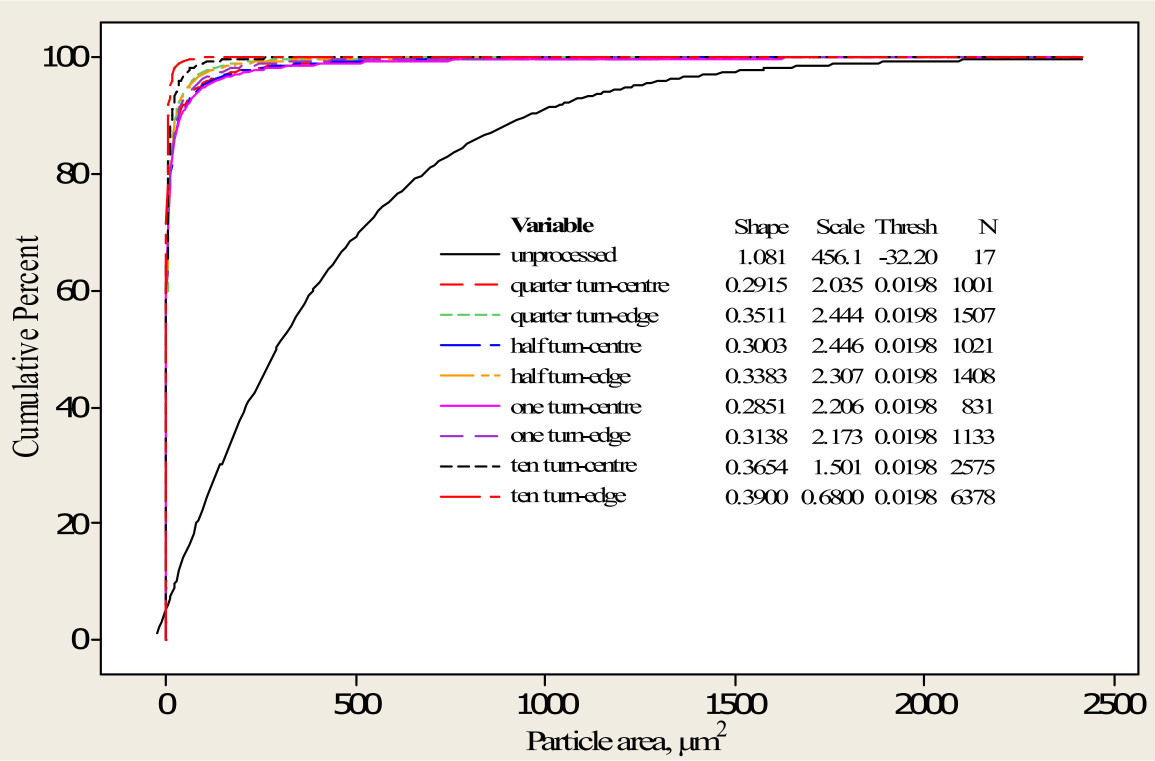

Figure 4.9: The 3-parameter Weibull cumulative distribution plots of areas of particle in unprocessed and HPT-processed Al-12%Si piston samples showing that the area population is heavily skewed to smaller particles after 10 HPT turns. The parameter values are also shown

Figures 4.10 and 4.11 show plots of circularity vs. particle area for $\frac{1}{4}$ and 10 turns at centre and edge as obtained from the ImageJ analysis. Larger particles exhibit irregular morphology. This can be seen in Figure 4.10a, where most of the particles have a circularity of less than 0.4. This is consistent with an earlier report [70] in which larger particles were shown to have irregular shapes. This is because after $\frac{1}{4}$ turn, there were large and interconnected intermetallic particles present as observed in Figure 4.3a. It can be seen in Figure4.11 that there is increase in circularity of particles with the number of turns as more particles are broken down. This is consistent with the earlier observation as shown in Figure 4.3h where circular small Si particles were present after 10 turns. However, it can be seen that after 10 turns there are still many irregular-shaped particles present. This mix of circular and irregular particles could be another reason for asymmetrical microhardness line profile after 10 turns.

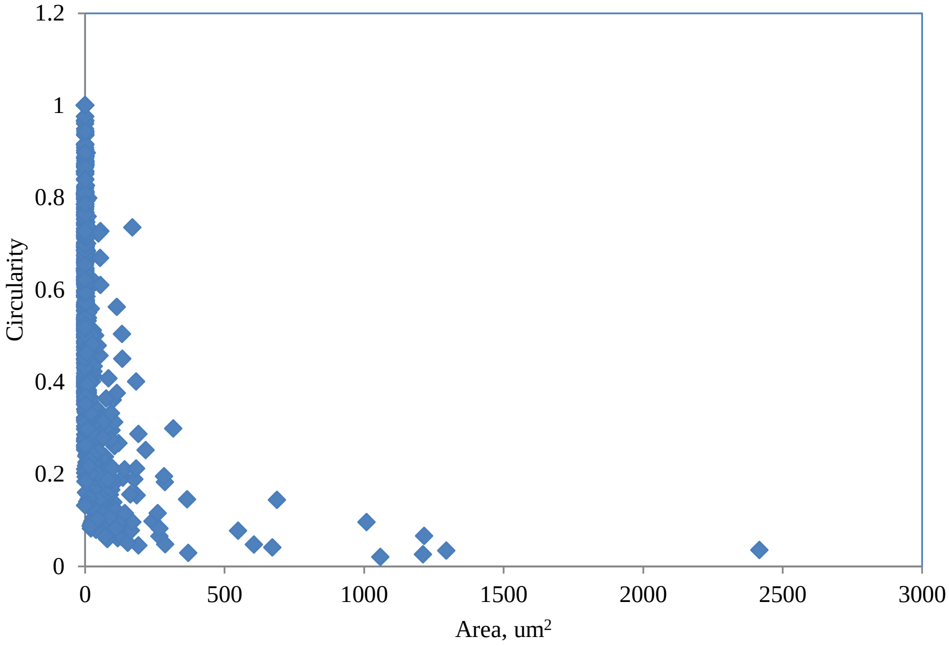

(a) $\frac{1}{4}$ turn-central region

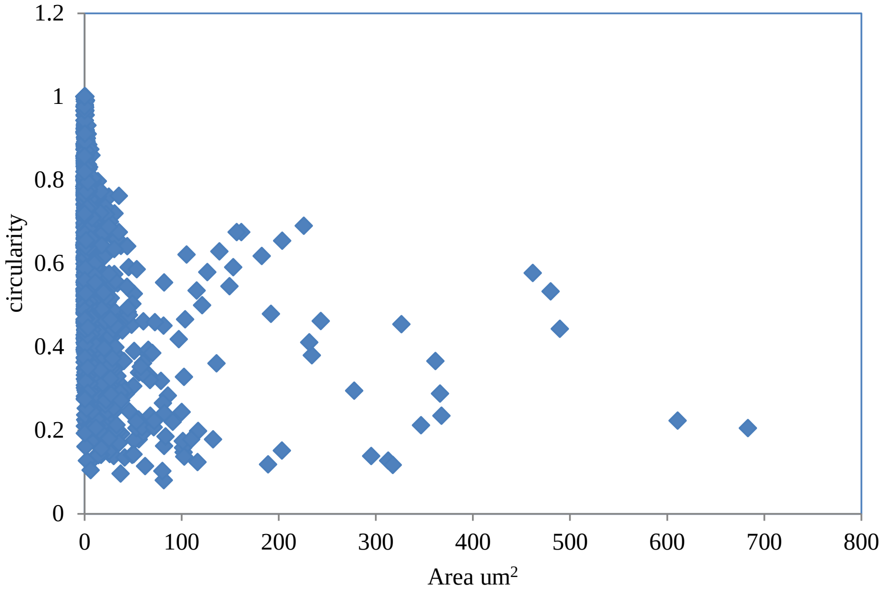

(b) $\frac{1}{4}$ turn-edge

Figure 4.10: Relationship between circularity and particle area for $\frac{1}{4}$-turn HPT-processed Al-12%Si alloy

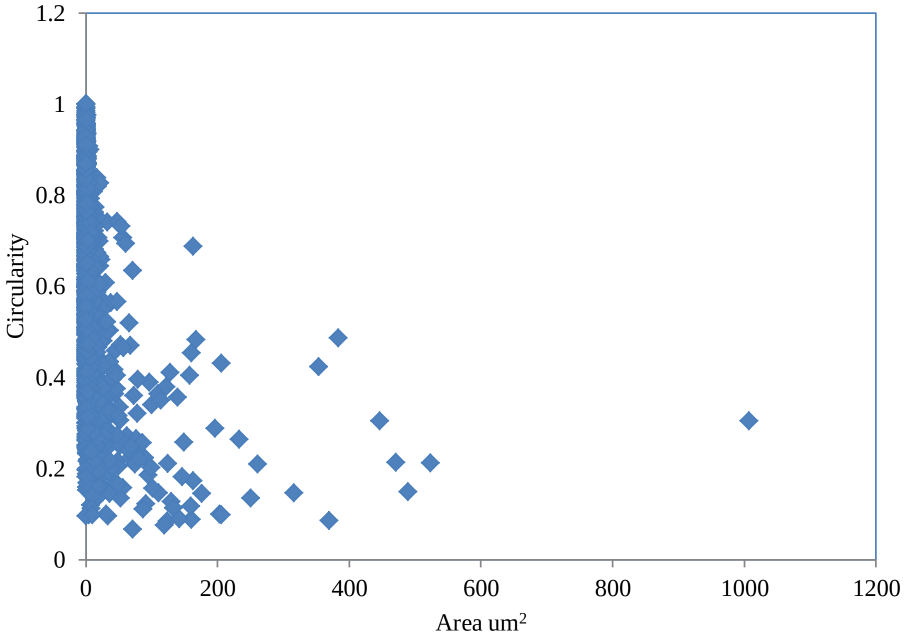

(a) 10 turns-central region

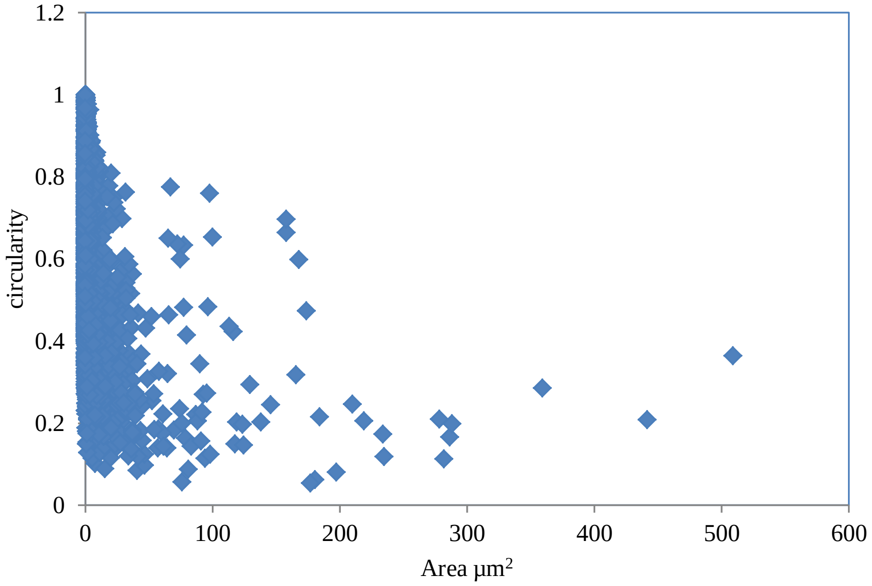

(b) 10 turns-edge

Figure 4.11: Relationship between circularity and particle area for 10-turn HPT-processed Al-12%Si alloy

4.3 High-pressure Torsion Processing of Unmodified Al-7%Si Piston Alloy

4.3.1 Properties of as-received cast unmodified Al-7%Si piston alloy

Microstructure

Figure 4.12 shows the optical micrograph of microstructure of as-received unmodified Al-7%Si piston alloy at different optical magnifications. The microstructure contains coarse Si particles and occasionally long and irregularly shaped intermetallic particles. At lower magnification, both coarse silicon particles and long secondary particles can be seen (Figure 4.12a) whereas at higher magnification, irregular shaped intermetallic particles can be seen (Figure 4.12b). The intermetallic particles present in this alloy are similar to those identified in Al-12%Si piston sample.

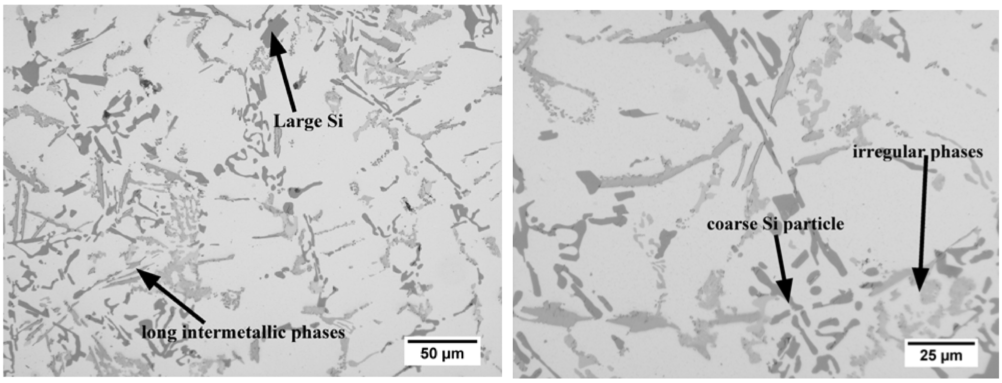

(a) Showing long secondary phases (b) Showing irregular secondary phases

Figure 4.12: Optical micrograph of as-received unmodified cast Al-7%Si piston alloy sample

Microhardness

Figure 4.13 shows the average microhardness and scatter bars along the diameter of as-received Al-7%Si piston alloy. The microhardness is not as uniform along the diameter due to the nature of the microstructure. This is similar to results for Al-12%Si piston alloy.

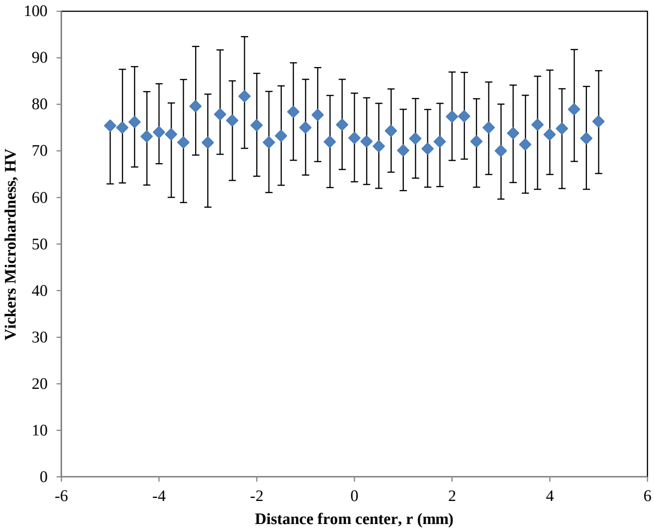

Figure 4.13: Vickers Microhardness across the diameter of unprocessed unmodified Al-7%Si alloy

4.3.2 Microstructural evolution

Figure 4.14 shows the optical micrograph of Al-7%Si piston alloy sample after $\frac{1}{4}$, $\frac{1}{2}$, 1 and 10 HPT turns. There is no observable change in the microstructure at the central region after $\frac{1}{4}$ turn since large and unbroken Si and intermetallic particles can be observed in Figure 4.14a. At the edge, there is a break down of intermetallic phases as indicated in Figure 4.14b. A higher magnification micrograph at the edge, (Figure 4.15), reveals cracks on Si and other intermetallic particles. This means that Si particles have started breaking down.

After $\frac{1}{2}$ HPT turn, a few broken Si and fragments of other intermetallic particles can be observed (Figure 4.14c). At the edge, Figure 4.14d, there is no significant break down since large particles and unbroken Si particles are still present.

After 1 turn, the microstructure at the centre shown in Figure 4.14e is not very different from that observed after $\frac{1}{2}$. At the edge, however, considerable transformation of the microstructure can be observed as shown in Figure 4.14f. There is break down and redistribution of Si and intermetallic particles throughout the microstructure. Near-circular particles can also be observed. This observation is further illustrated by Figure 4.16. However, there are still large phases and unbroken Si particles present which means that full microstructural refinement has not yet occurred.

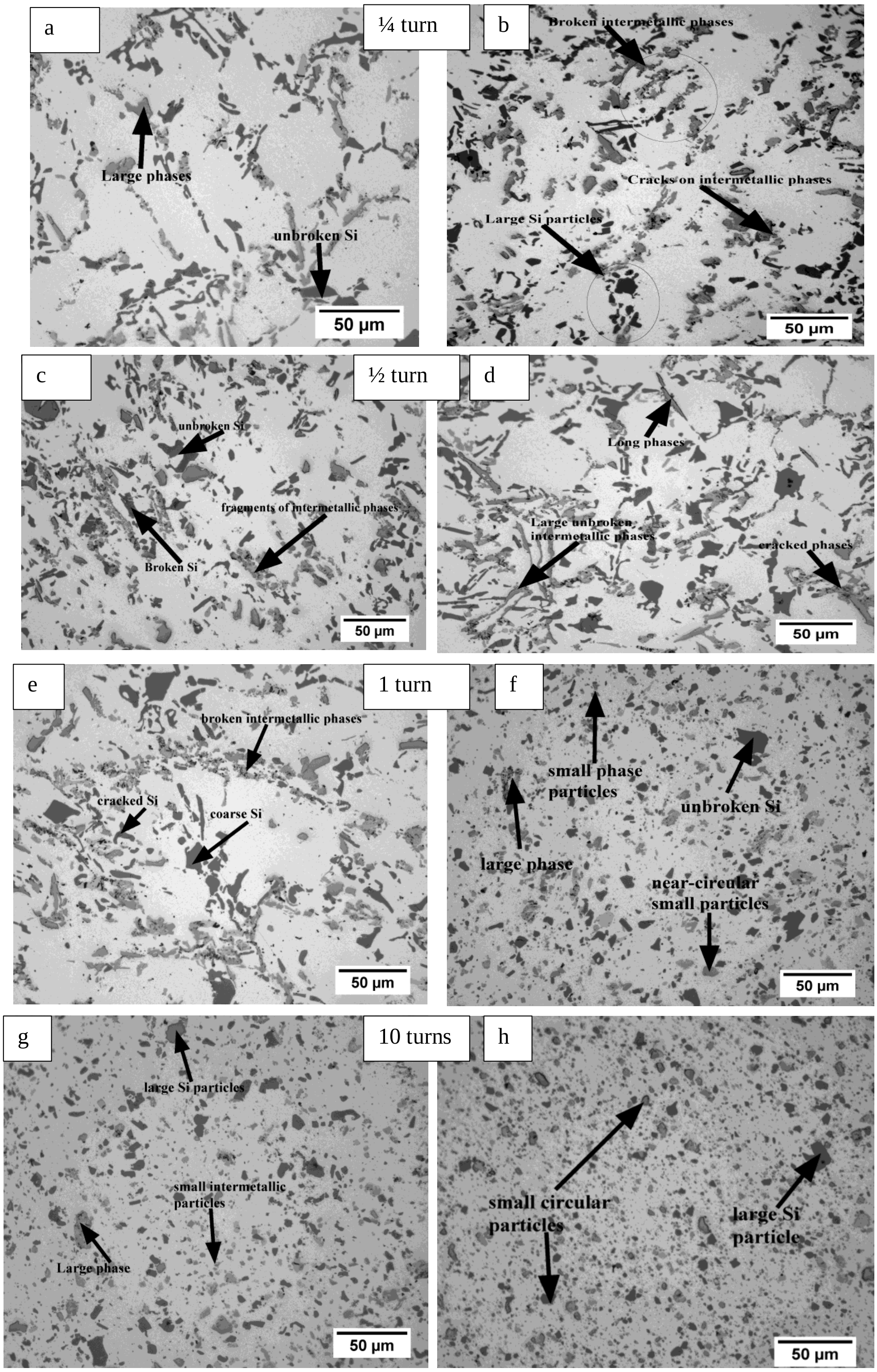

Figure 4.14: Optical micrographs showing microstructural evolution during HPT of unmodified Al-7%Si alloy at different number of turns. Images a, c, e, g represent the microstructure at the central region while images b, d, f, h represent the microstructure at the edges.

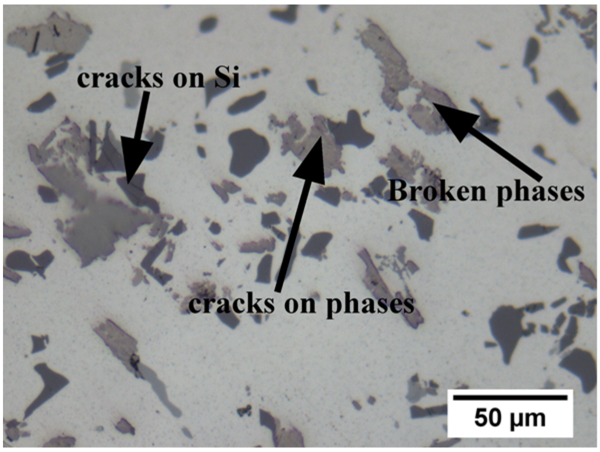

Figure 4.15: Optical micrograph at the edge of unmodified Al-7%Si alloy showing cracks on Si and intermetallic phases after $\frac{1}{4}$ HPT turn

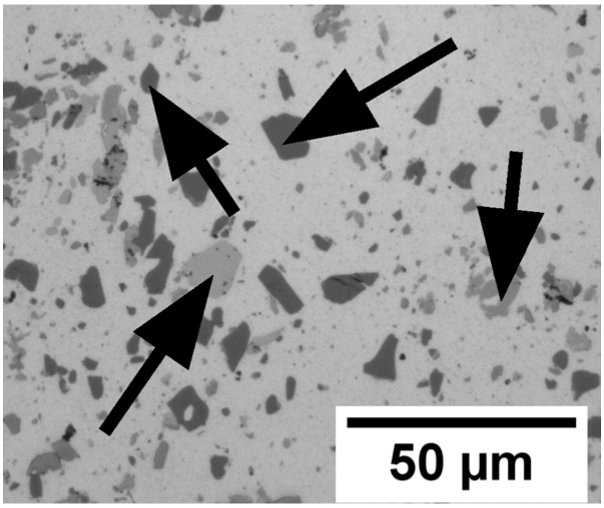

Figure 4.16: Optical micrograph showing near-circular particles (indicated by arrows) at edge of unmodified Al-7%Si alloy after 1 HPT turn

After 10 turns, it can be observed that most of the intermetallic particles and coarse Si have broken down into small particles at the centre as shown in Figure 4.14g. However, there are occasionally large particles, which are still present at the central region. At the edge, Figure 4.14h, the microstructure is nearly equiaxed with very fine circular particles uniformly distributed within the Al matrix. The uniform distribution of particles can be confirmed by the nearly homogeneous microhardness profile after 10 turns in subsection 4.3.3. However, as shown in Figure 4.17, large Si particles are still present. This is an indication that unlike other intermetallic particles, Si particles have not fully broken down after 10 turns. These observations are consistent with earlier work on properties of particles in Al-Si piston alloys in which Si particles were shown to have the highest hardness and strength [74]. This is the reason for slow break down of Si particles during HPT.

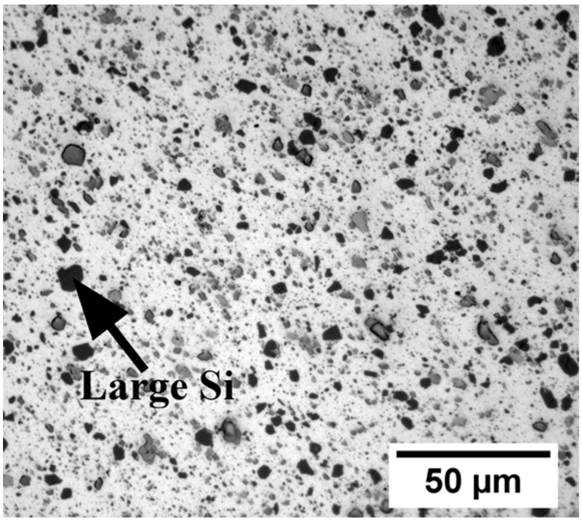

Figure 4.17: Optical micrograph showing large Si at the edge of unmodified Al-7%Si alloy after 10 turns

4.3.3 Microhardness evolution

Figure 4.18 shows average Vickers microhardness line profile for unmodified Al-7%Si piston alloy after $\frac{1}{4}$, $\frac{1}{2}$, 1 and 10 HPT turns. After $\frac{1}{4}$ turn, the microhardness at the centre has increased by ∼43% whereas at the periphery, the microhardness has increased by ∼58%. The scatter bars of the measured microhardness values are higher at the periphery than at the centre. This can be attributed to the presence of broken intermetallic particles, cracked Si and large Si particles in the microstructure at the edge as it was observed in Figure 4.14b. This means that if the microhardness indenter hits on all these particles and phases for a single measurement, the scatter bar in that microhardness value will be higher compared to that when the indenter hits on one of these phases.

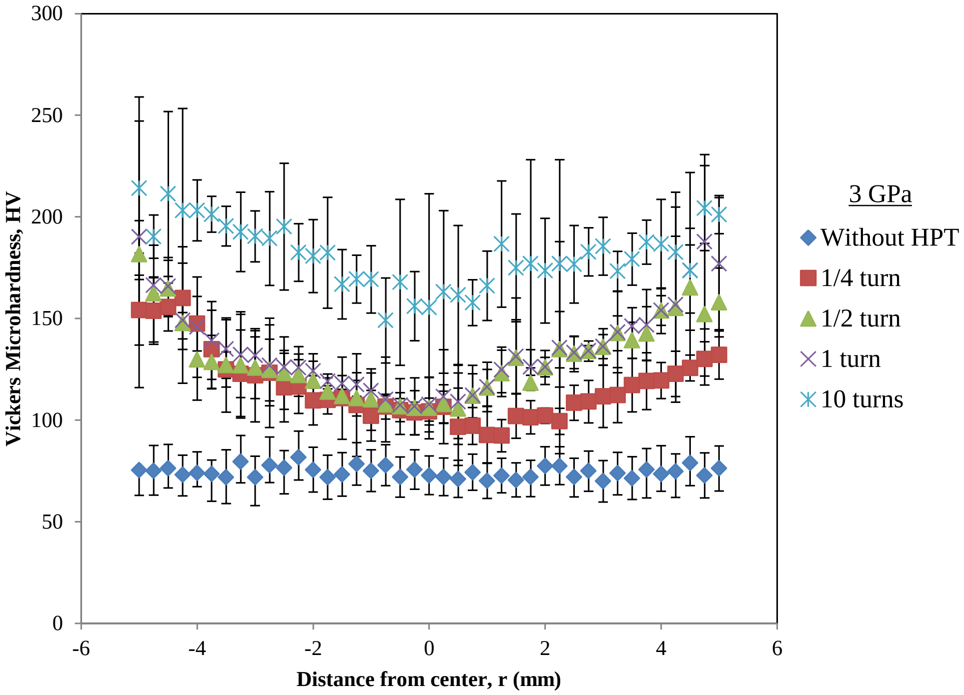

Figure 4.18: Vickers Microhardness and scatter bars along the diameter of unprocessed and processed unmodified Al-7%Si alloy at different number of turns

After $\frac{1}{2}$ turn, the increase in microhardness around the central region is ∼45%. This increment is nearly equal to that reported after $\frac{1}{4}$ turn. This is consistent with the microstructural evolution at the central region as observed in Figure 4.14c. The microhardness at the edge has increased by ∼105%. The scatter bars are larger than those observed after $\frac{1}{4}$ HPT turn. Furthermore, larger scatter bars can be observed at the edges than at the central region. This indicates that the scatter bars are increasing with strain. This is attributed to more break down and redistribution of particles observed at regions of higher strains.

After 1 HPT turn, the microhardness values have increased by ∼48% and ∼132% at the central region and periphery respectively. The microhardness profile at the central region is nearly equal to that observed after $\frac{1}{2}$ turn. This is expected since there were no significant microstructural changes observed at the central region after 1 turn in subsection 4.3.2 (Figure 4.14e). This observation is confirmed by the Weibull distribution in subsection 4.3.4 in which the plots after $\frac{1}{2}$ and 1 turns at the central region overlap at various points of the graph (Figure 4.20). There are larger scatter bars at the edge than at the central region. This can be attributed to break down of phases into small and near-circular particles at the edges as it was observed in Figure 4.14f (subsection 4.3.2).

The microhardness values at the centre and edge have increased by ∼116% and ∼160% respectively after 10 turns. Homogeneity in microhardness values can be observed from ∼2.8 mm to the edge. This is because most of the intermetallic phases and Si particles towards the edge have broken down into small and circular particles as observed in subsection 4.3.2. The microstructural refinement observed after 10 turns is the reason for high microhardness increase. The scatter bars are larger than those observed for $\frac{1}{4}$, $\frac{1}{2}$ and 1 turns (Figure 4.18). This is because there is more break down and redistribution of Si and other particles within the

Al matrix after 10 turns.

Generally, from Figure 4.18 we can draw the conclusion that the microhardness around the central region is almost equal after $\frac{1}{4}$, $\frac{1}{2}$ and 1 HPT turns. This is because there are no significant microstructural changes at the central region after these number of turns as observed in subsection 4.3.2. We can also draw the conclusion that all the microhardness line profiles are symmetrical about the central region. This is because higher microstructural refinement is observed at the edge than at the centre in subsection 4.3.2. This observation indicates that unmodified Al-7%Si piston alloy achieves microstructural/microhardness homogeneity through strain hardening as depicted by Figure 4.19. Finally, the scatter in microhardness measurements has increased with the number of HPT turns and along the diameter of the samples.

Figure 4.19 shows the variation of microhardness along the diameter with equivalent strain for HPT processed unmodified Al-7%Si piston alloy. The figure depicts a non-monotonic hardness-strain relationship exhibited by materials which undergo hardening with slow recovery. It can also be seen that the relationship is not symmetrical about the centre. This is due to nonhomogeneous microstructural refinement along the diameter of the sample observed earlier in subsection 4.3.2.

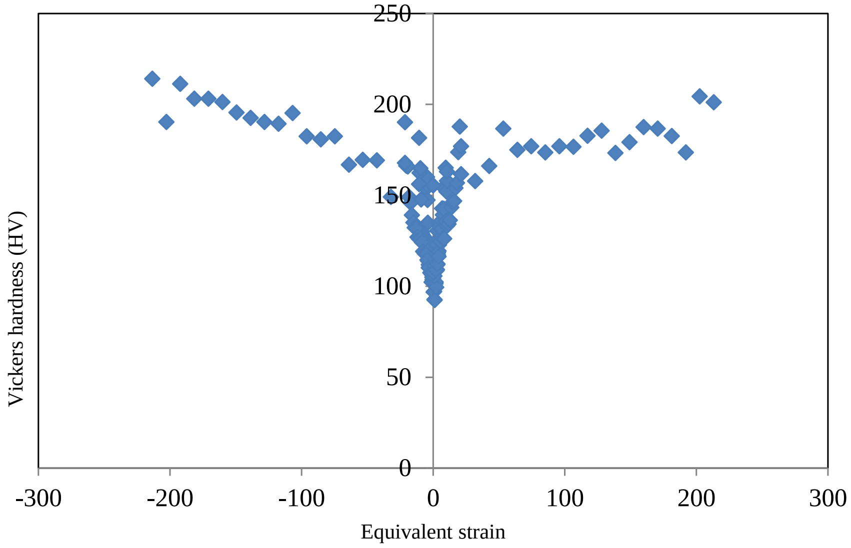

Figure 4.19: Microhardness versus equivalent strain for HPT-processed unmodified Al-7%Si sample

4.3.4 Distribution of particles in HPT processed unmodified Al-7%Si piston alloy

Figures 4.20 and 4.21 show the 3-parameter Weibull distribution fit for the area of particles for unprocessed and processed unmodified Al-Si piston alloy. The relatively larger AD values and P-values less than 0.005 indicate significant lack of good fit for the 3-parameter Weibull distribution of this data. The figures show similar results to those described under Al-12%Si sample. However, note the closeness of distribution curves at the centre and edge after 10 turns. It can be deduced that 90% of the particles (not shown in the figures) have areas equal to or less than 8.4 μm^2 and 12.4 μm^2 at edge and centre respectively. This closeness in particle refinement is the reason for reduced microhardness gradient after 10 turns shown in Figure 4.18.

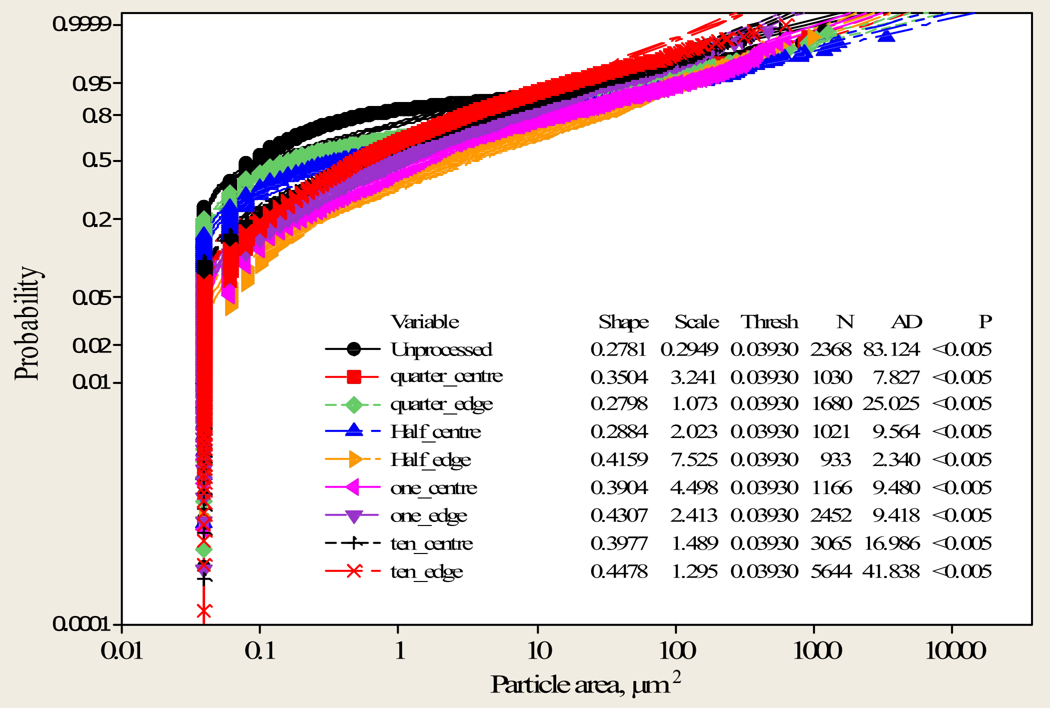

Variable	Shape	Scale	Thresh	N	AD	P
Unprocessed	0.2781	0.2949	0.03930	2368	83.124	<0.005
quarter_centre	0.3504	3.241	0.03930	1030	7.827	<0.005
quarter_edge	0.2798	1.073	0.03930	1680	25.025	<0.005
Half_centre	0.2884	2.023	0.03930	1021	9.564	<0.005
Half_edge	0.4159	7.525	0.03930	933	2.340	<0.005
one_centre	0.3904	4.498	0.03930	1166	9.480	<0.005
one_edge	0.4307	2.413	0.03930	2452	9.418	<0.005
ten_centre	0.3977	1.489	0.03930	3065	16.986	<0.005
ten_edge	0.4478	1.295	0.03930	5644	41.838	<0.005

Figure 4.20: The 3-parameter Weibull probability plots of areas of particle in unprocessed and HPT-processed unmodified Al-7%Si piston alloy. The parameter, AD and P values are also shown

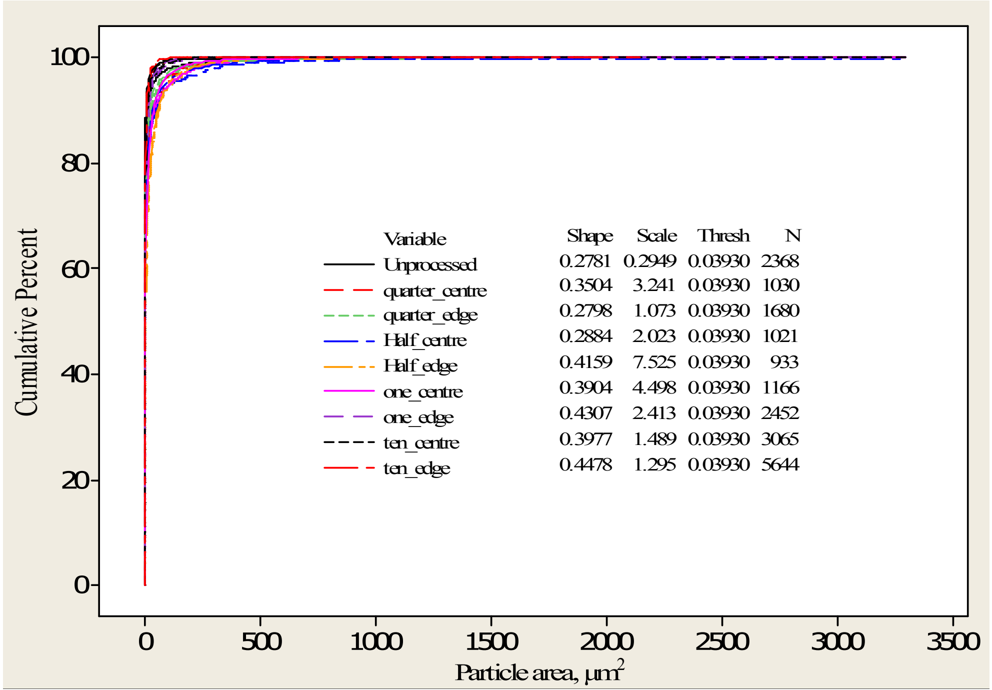

Figure 4.21: The 3-parameter Weibull cumulative distribution plots of areas of particle in unprocessed and HPT-processed unmodified Al-7%Si piston samples showing that the area population is heavily skewed to smaller particles after 10 HPT turns. The parameter values are also shown

The circularity Vs. particle area given in Figures 4.22 and 4.23 show that the circularity increases with HPT turns and reduction in particle sizes. It can be noted that at all number of turns, there is a 'mixture' of circular and irregular particles. At very low turns ($\frac{1}{4}$ turn), there are more long and irregular shaped particles whereas after 10 turns, there are relatively more regular shaped particles. As such, the local microhardness for each case is an average of microhardness of different phases. This explains the random distribution of microhardness scatter bars for both cases as observed in Figure 4.18.

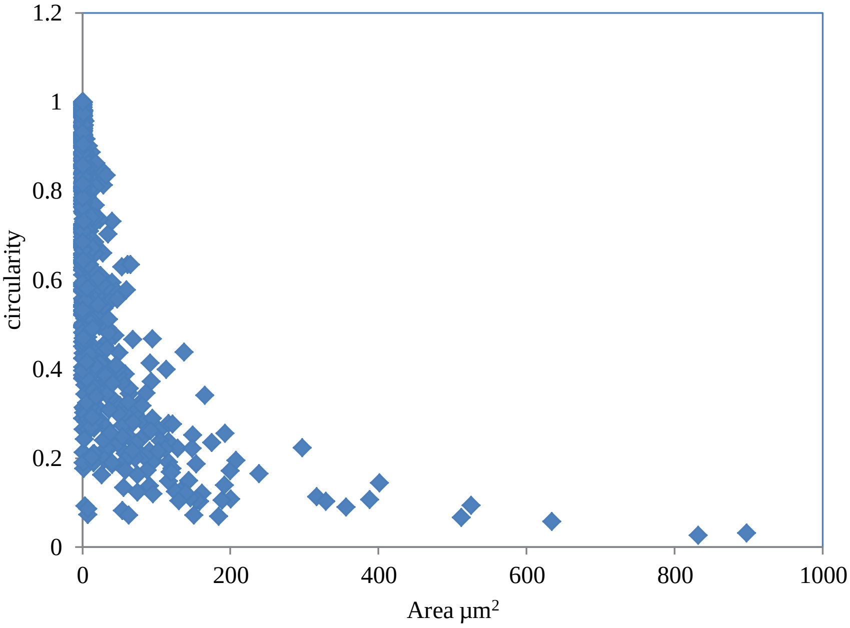

(a) $\frac{1}{4}$ turn-central region

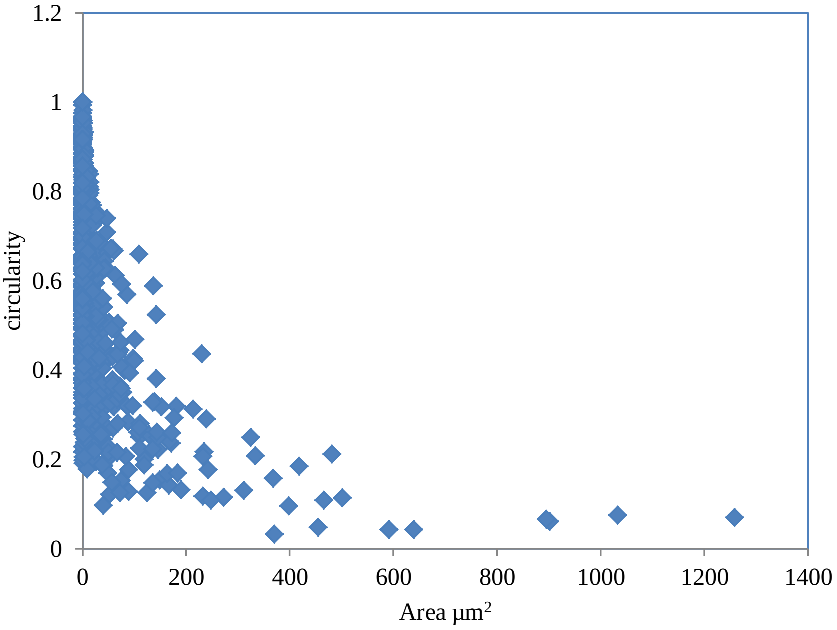

(b) $\frac{1}{4}$ turn-edge

Figure 4.22: Relationship between circularity and particle area for $\frac{1}{4}$-turn HPT-processed unmodified Al-7%Si alloy

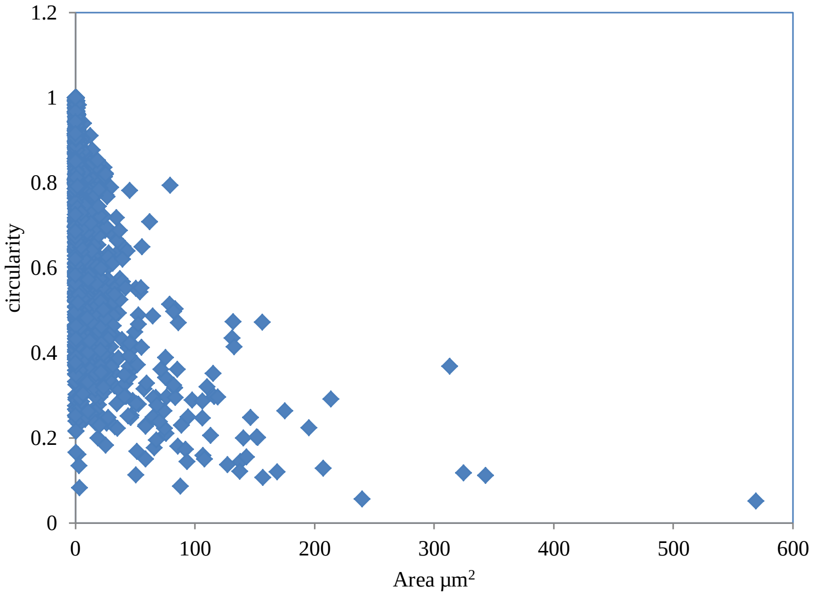

(a) 10 turns-central region

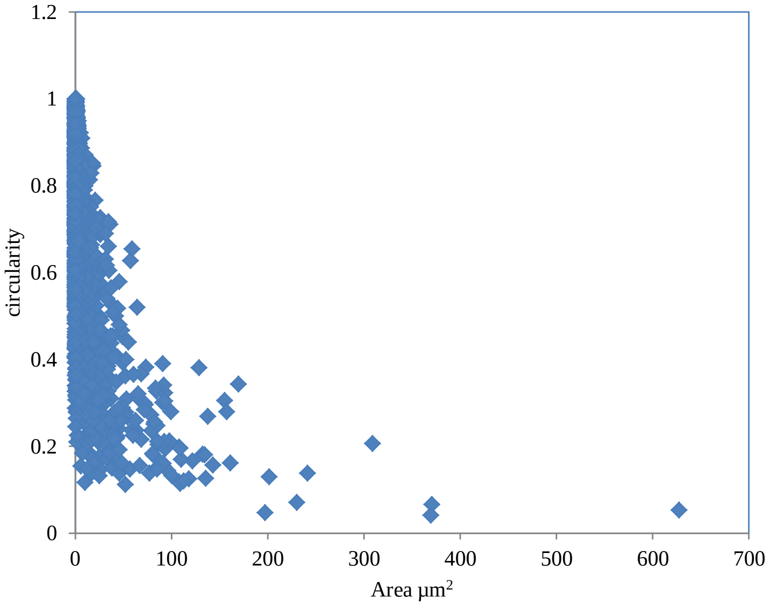

(b) 10 turns-edge

Figure 4.23: Relationship between circularity and particle area for 10-turn HPT-processed unmodified Al-7%Si alloy

4.4 High-pressure Torsion Processing of the Modified Al-7%Si Piston Alloy

4.4.1 Properties of As-received modified cast Al-7%Si piston alloy

Microstructure

Figure 4.24 shows the microstructure of the as-received modified cast Al-7%Si piston alloy. The modification of this alloy was achieved through addition of strontium. Strontium coats the silicon particles during solidification such that formation of Si dendrites does not occur. As such, the microstructure contains modified silicon structures and other intermetallic particles. Most of the phases contained in this alloy are similar to those present in the unmodified Al-7%Si except that this alloy contains smaller silicon particles due to modification by strontium addition. One of the most common phases in this alloy is AlCuNi phase and is indicated in the Figure 4.24 [61].

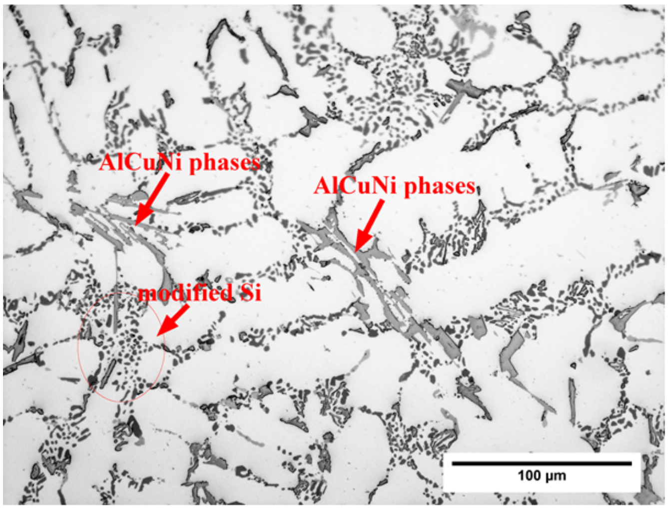

Figure 4.24: Optical micrograph of the unprocessed modified cast Al-7%Si piston alloy. The AlCuNi phase has been identified from literature

Microhardness

Figure 4.25 shows the microhardness and scatter bars along the diameter of the as-received modified cast Al-7%Si piston alloy. The microhardness is nearly uniform along the diameter.

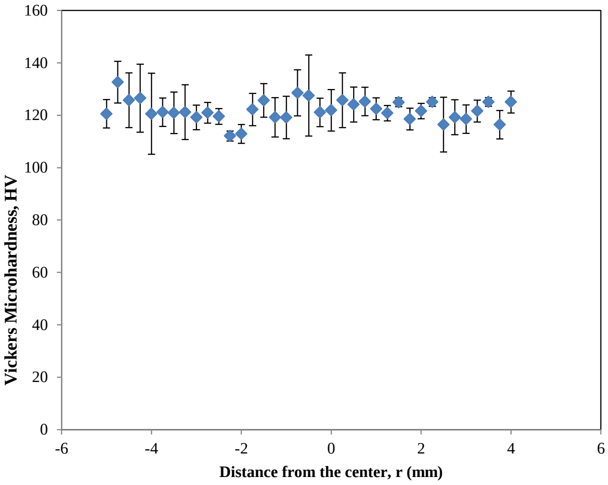

Figure 4.25: Vickers microhardness and scatter bars along the diameter of the unprocessed modified cast Al-7%Si piston alloy

4.4.2 Microstructural evolution

Figure 4.26 shows the optical micrograph of the modified Al-7%Si piston alloy after $\frac{1}{4}$, $\frac{1}{2}$, 1 and 10 HPT turns. There are no significant microstructural changes observed at the central region and the microstructural features are basically similar to those in the as-received alloy (Figure 4.26a). However, at higher magnification shown by the optical and SEM micrographs in Figures 4.27 and 4.28 respectively, cracking and breakage of intermetallic phases can be observed. At the edges, Figure 4.26b, very small cracks on AlCuNi phases and a few fragmented network of modified silicon can be observed. This is further illustrated by a higher magnification micrograph in Figure 4.29.

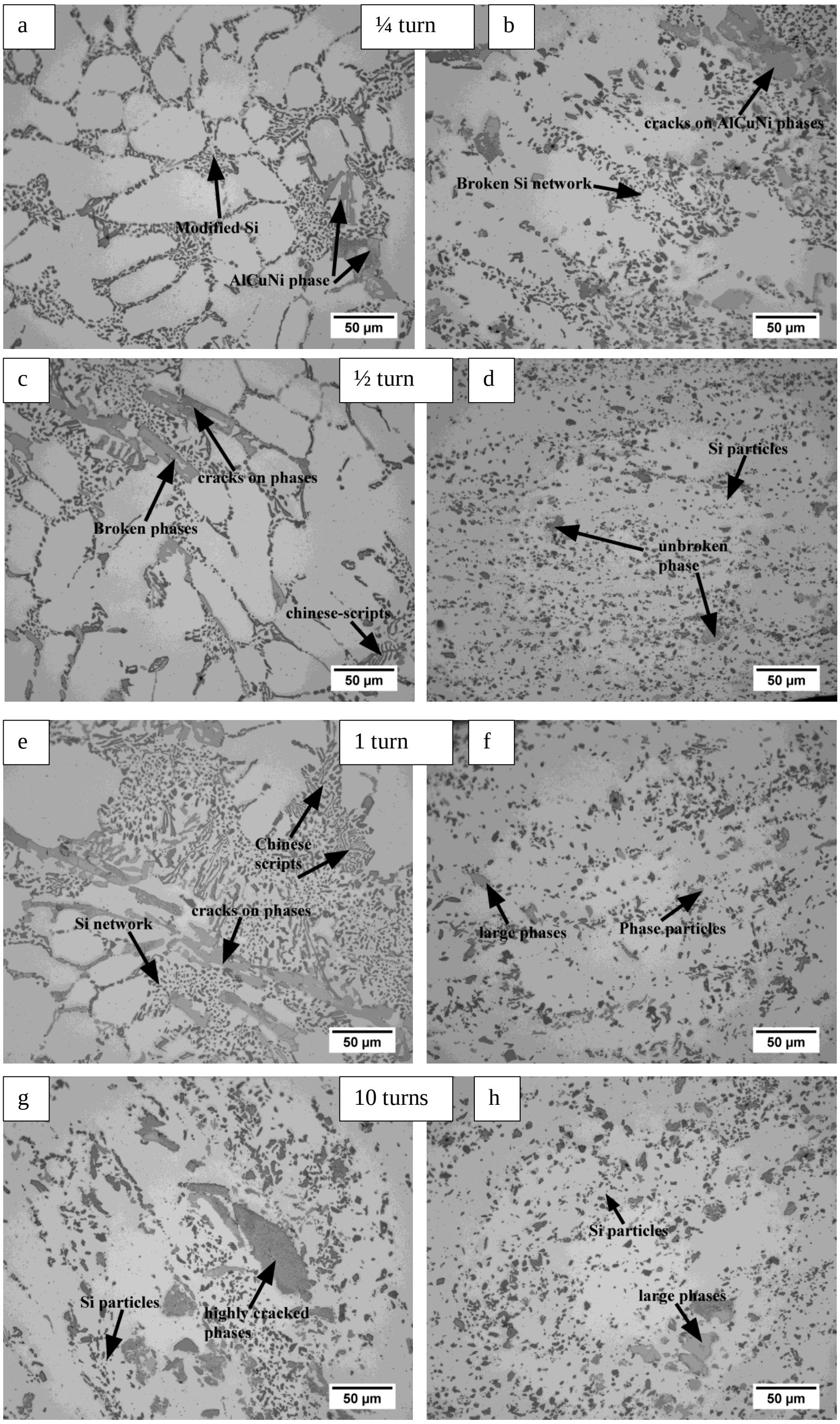

Figure 4.26: Optical micrographs showing microstructural evolution during HPT of modified Al-7%Si alloy at different number of turns. Images a, c, e, g represent the microstructure at the central region while images b, d, f, h represent the microstructure at the edges.

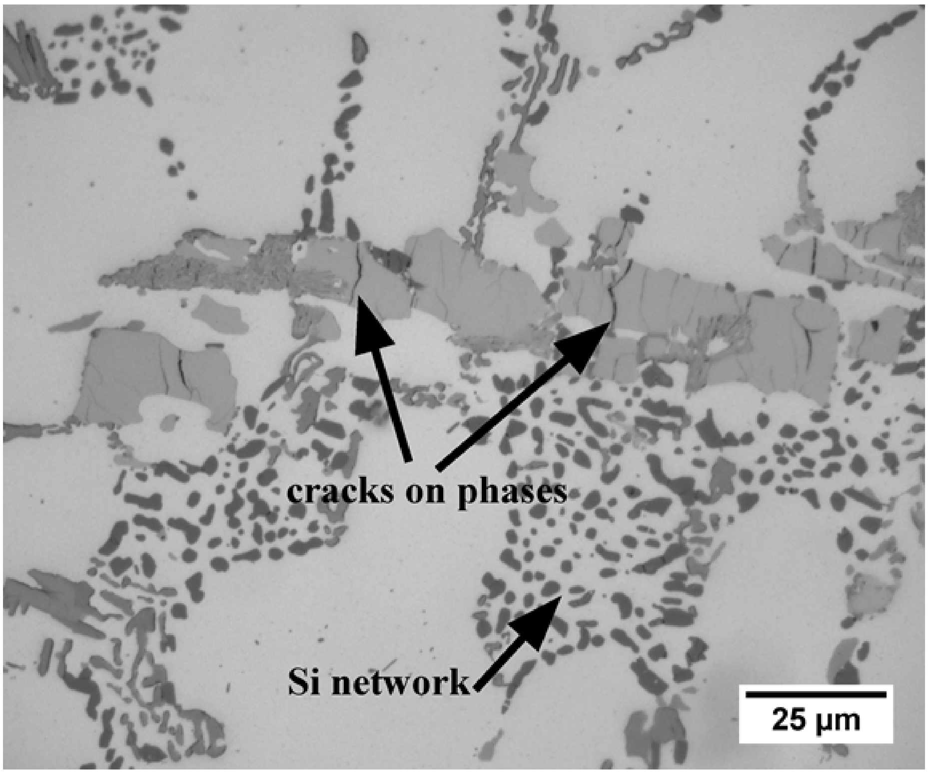

Figure 4.27: Optical micrograph showing cracked intermetallic phases at the central region after $\frac{1}{4}$ HPT turn

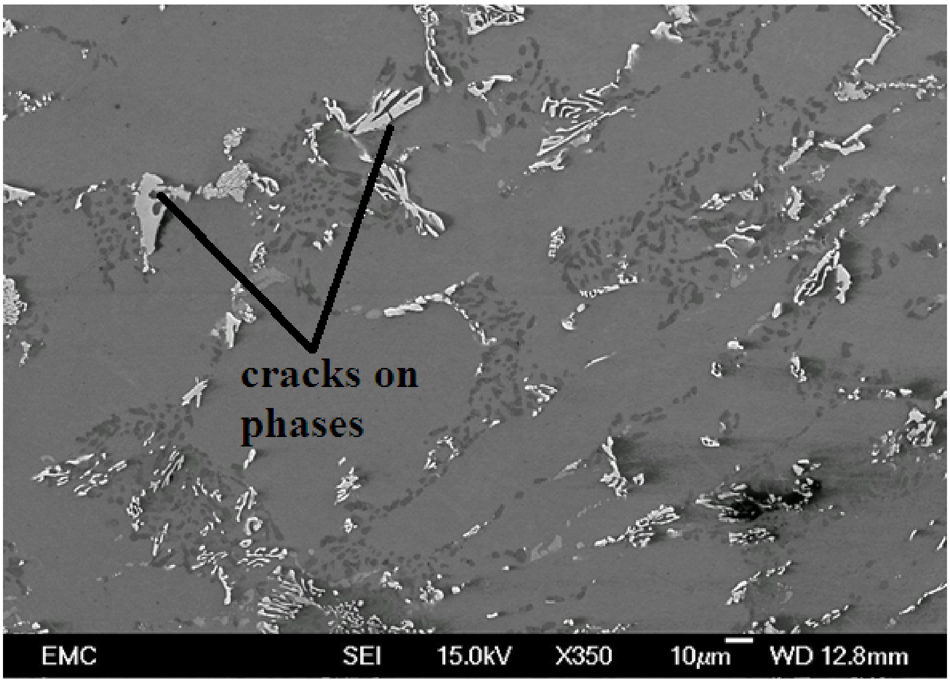

Figure 4.28: SEM micrograph showing cracked intermetallic phases at the central region after $\frac{1}{4}$ HPT turn

The SEM image in Figure 4.30 shows the presence of broken intermetallic phases and silicon particles at the edge of the sample. The presence of Si particles is an indication of the start of the break down of modified Si network into individual Si particles.

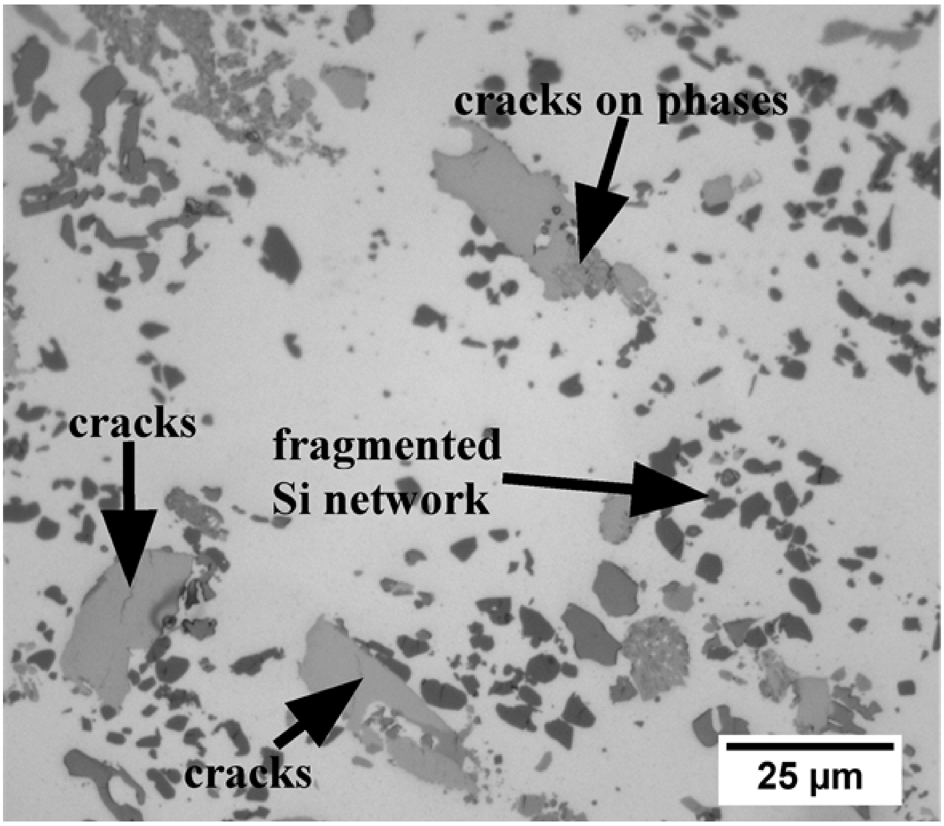

Figure 4.29: Optical micrograph showing cracked intermetallic phases and fragmented Si networks at the edge after $\frac{1}{4}$ HPT turn

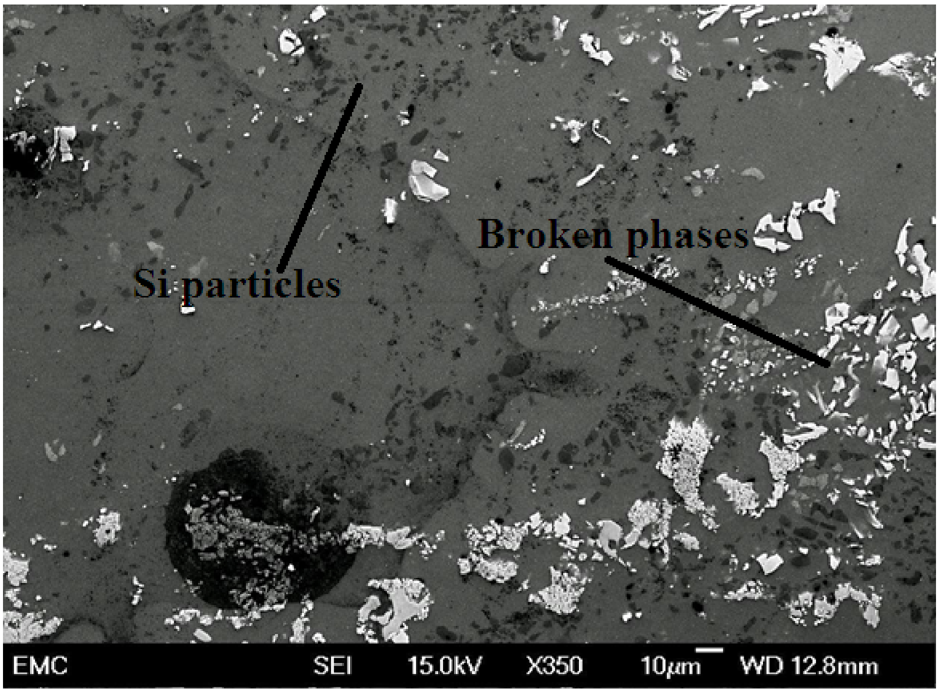

Figure 4.30: SEM micrograph showing broken phases and Si particles at the edge after $\frac{1}{4}$ HPT turn

After $\frac{1}{2}$ turn, few broken intermetallic particles and unchanged Si structures can be seen at the central region (Figure 4.26c). The SEM micrograph in Figure 4.31 of the central region shows break down of a few modified Si networks into small circular silicon particles. These silicon particles can be observed mostly where break down of the intermetallic particles has occurred. This means that AlCuNi phases break down more quickly than modified Si networks. This is further supported by the presence of cracks on the intermetallic phases surrounded by Si networks in Figure 4.32.

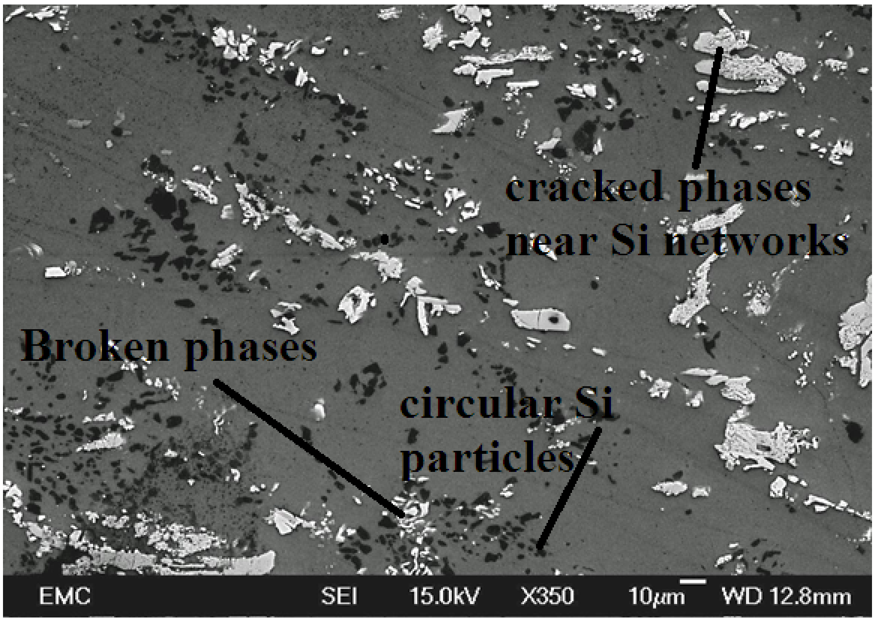

Figure 4.31: SEM micrograph showing circular Si particles around the broken phases at the centre after $\frac{1}{2}$ HPT turn. The broken phases are surrounded by unbroken network of modified Si

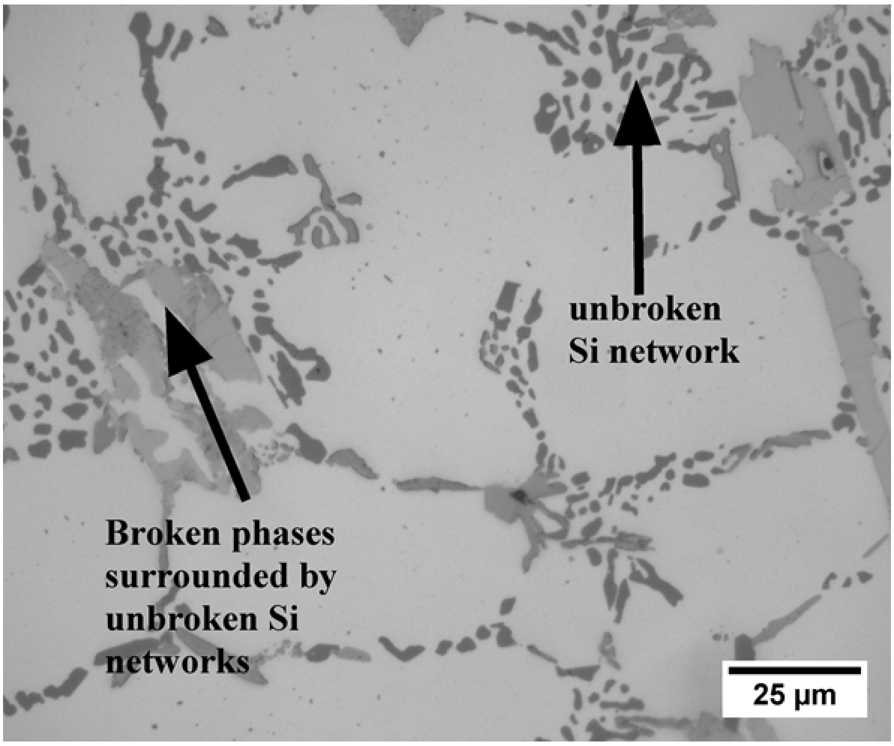

Figure 4.32: Optical micrograph showing cracked and broken phases surrounded by unbroken Si networks after $\frac{1}{2}$ HPT turn at the central region of modified Al-7%Si alloy

At the edge, most of the Si networks have broken down into individual particles as shown in Figure 4.26d. Most of the intermetallic phases at the edge are fragmented and redistributed within the microstructure. The SEM micrograph in Figure 4.33 however shows there are still unbroken and interconnected Si particles and phases present at the edge.

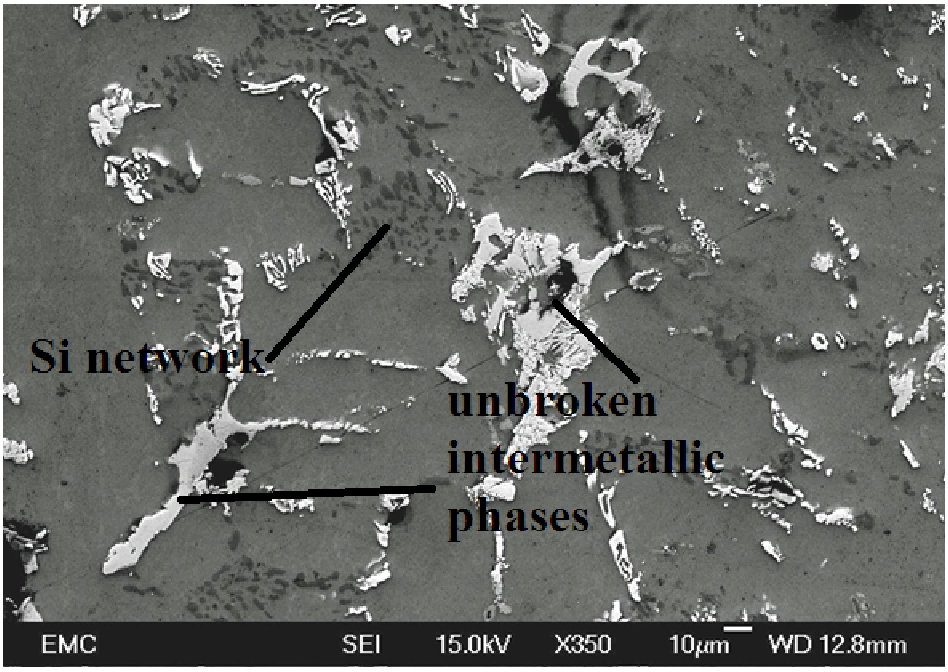

Figure 4.33: SEM Micrograph showing unbroken Si particles and intermetallic phases at the edge of modified cast Al-7%Si after $\frac{1}{2}$ HPT turn

There are no significant microstructural transformations observed after 1 turn (Figures 4.26e and 4.26f) since most of the features are similar to those observed after $\frac{1}{2}$ turn. After 10 turns, most of the intermetallic phases are broken down as indicated in Figure 4.26g. However, as seen in Figures 4.34 and 4.35, the microstructure still contains unbroken Si networks and cracked intermetallic phases. The microstructure at the edge contains small Si and intermetallic particles redistributed within the aluminium matrix (Figure 4.26h). Circular particles can also be observed as indicated in Figure 4.36. However, a higher SEM magnification shows that there are still large but cracked intermetallic particles present at the edge after 10 turns as shown in Figure 4.37. It can be deduced that in this alloy, there is no break down of individual Si particles; only fragmentation of network of modified Si into individual Si particles has been observed. This means that the modified Al-7%Si piston alloy should be processed for more than 10 turns for the break down of Si particles to occur.

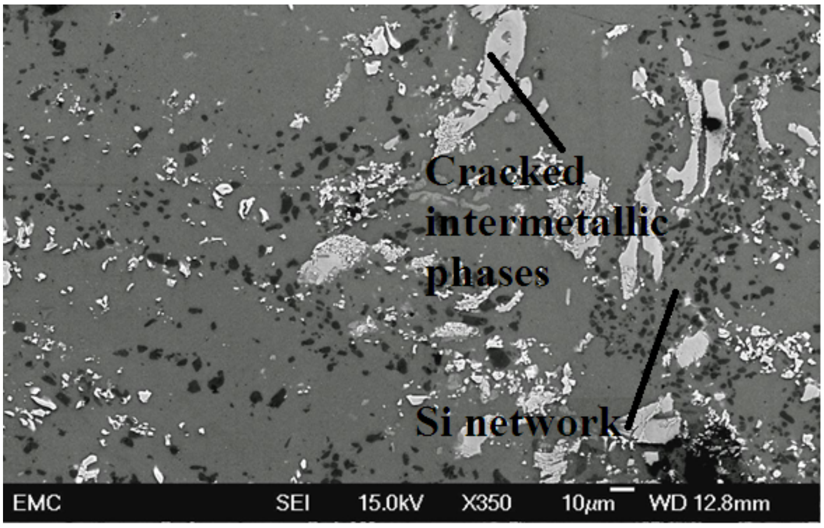

Figure 4.34: SEM micrograph showing unbroken Si network and intermetallic phases at the central region of the modified Al-7%Si after 10 HPT turns

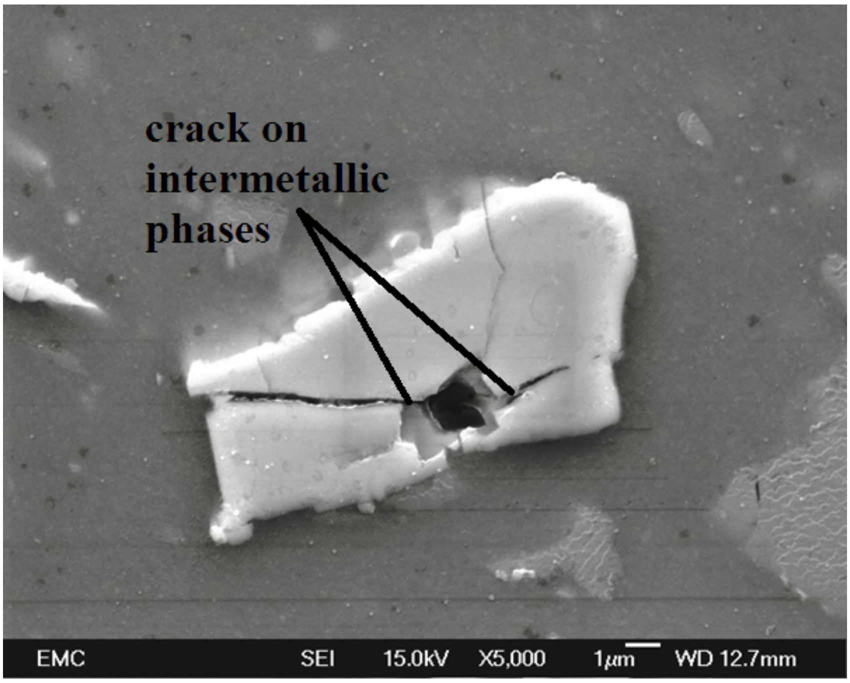

Figure 4.35: SEM micrograph showing cracks on intermetallic phases at the central region of modified Al-7%Si after 10 turns

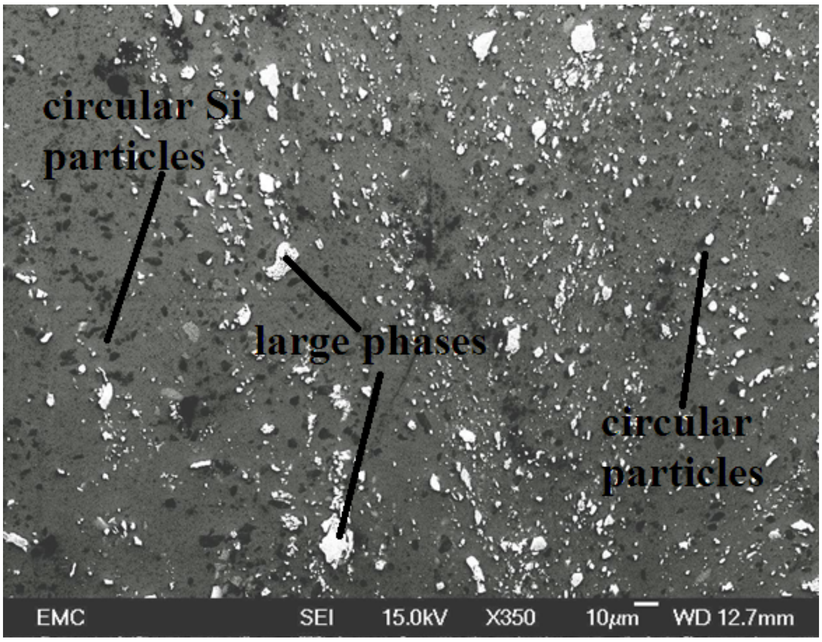

Figure 4.36: SEM micrograph showing circular particles at the edge of modified Al-7%Si after 10 turns

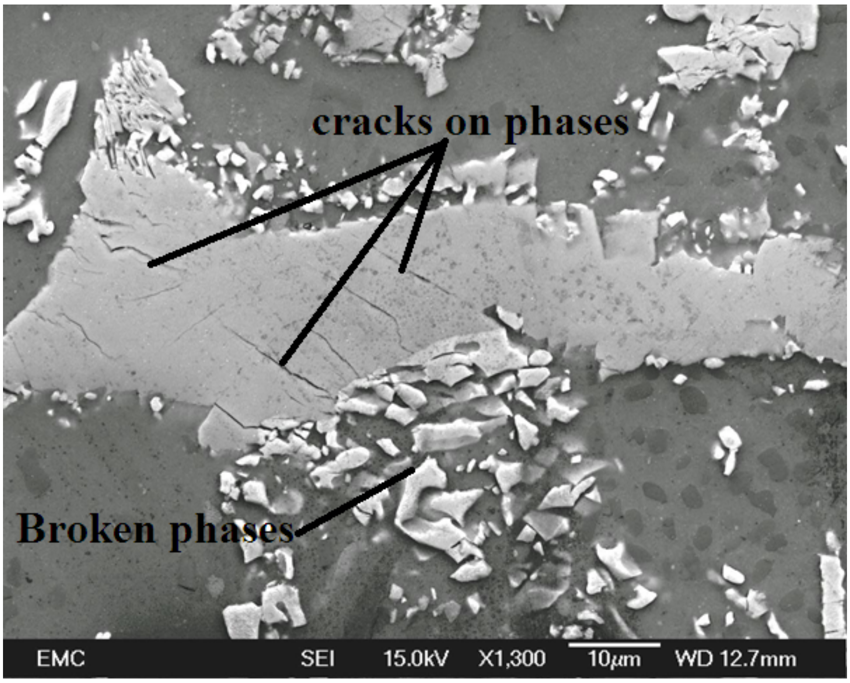

Figure 4.37: SEM micrograph showing cracked but unbroken intermetallic particles at the edge of modified Al-7%Si after 10 turns

4.4.3 Microhardness evolution

Figure 4.38 shows the variation of microhardness values and scatter bars along the diameter of modified Al-7%Si piston alloy after HPT processing. The microhardness and scatter bars for the as-received alloy are also shown for comparison. After $\frac{1}{4}$ turn, the microhardness has increased from an initial value of ~120 HV for the as-received alloy to ~145 HV around the central region, which is ~21% increase. At the edge, the microhardness has increased to ~180.7 HV, accounting for ~45% increase in microhardness. It can also be observed that the size of scatter bars along the diameter have increased significantly.

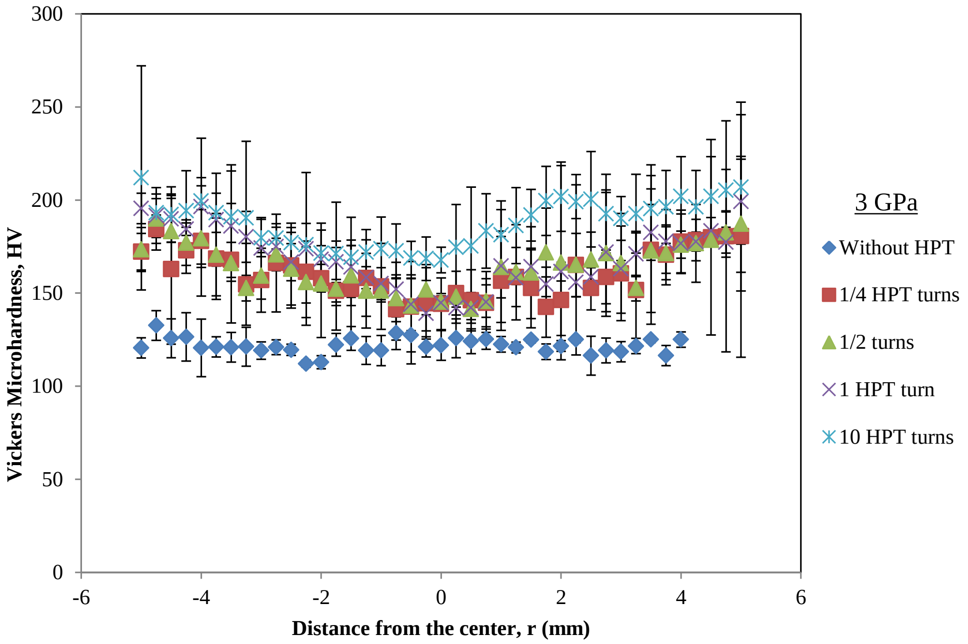

Figure 4.38: Vickers microhardness along the diameter of the unprocessed and HPT-processed modified Al-7%Si

After $\frac{1}{2}$ turn, the microhardness has increased by ~21.5% and ~50% at centre and edge respectively. The error bars of the microhardness measurements are generally larger compared to those after $\frac{1}{4}$ HPT turn. There are larger error bars at the edge than at the central region. This is because as observed in subsection 4.4.2, the microstructure at the edge (Figure 4.26) consists of broken and unbroken Si networks and intermetallic phases after half turn, hence the scatter in microhardness measurements.

The microhardness has increased by ~23% and ~60% at centre and edge respectively after 1 turn. The increase in microhardness from the centre to the edge is almost linear indicating that microstructural homogeneity has not been achieved. This is consistent with the microstructural observations after 1 turn in subsection 4.4.2. The scatter bars are slightly larger than those observed after $\frac{1}{2}$ turn.

Microhardness has increased by ∼35% and ∼66% at central region and edge respectively from the initial values of the as-received alloy after 10 turns. The microhardness along the diameter is nearly homogenous except that there is a ‘hump’ at the region between +1.8 and +2.5 mm. Microstructural observations around this region shown in Figure 4.39 reveal that the microstructure consists of fragmented Si networks and individual Si particles. Most of the intermetallic phases have broken down into small particles, which cannot be observed through an optical or SE microscope. Particle analysis (Figure 4.40 further shows that the region consists of particles with very high circularity values. Very high microhardness around this region is therefore due to presence of many circular Si particles. Silicon particles have the highest hardness (and hence strength) compared to all other phases in Al-Si alloys [61, 74] (see Table 6.1 in appendix B). However, further investigation is warranted to establish the mechanism for occurrence of this microstructural behavior. The scatter bars after 10 turns are generally larger than those observed after $\frac{1}{4}$, $\frac{1}{2}$ and 1 turns of HPT processing.

As shown in Figure 4.38, the microhardness line profiles are all symmetrical about the central region and the symmetry decreases with number of HPT turns. It can also be seen that the microhardness line profiles for $\frac{1}{4}$, $\frac{1}{2}$ and 1 turns are very close to each other. This is consistent with the microstructural observations made earlier in subsection 4.4.2 in which no major microstructural changes were observed for these number of turns.

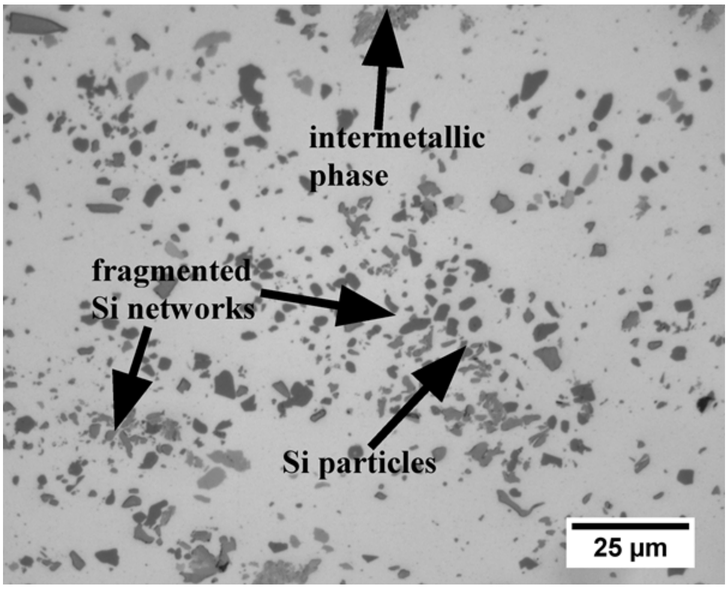

Figure 4.39: Microstructure of modified Al-7%Si piston alloy sample at region r=+1.8-2.5 mm after 10 turns

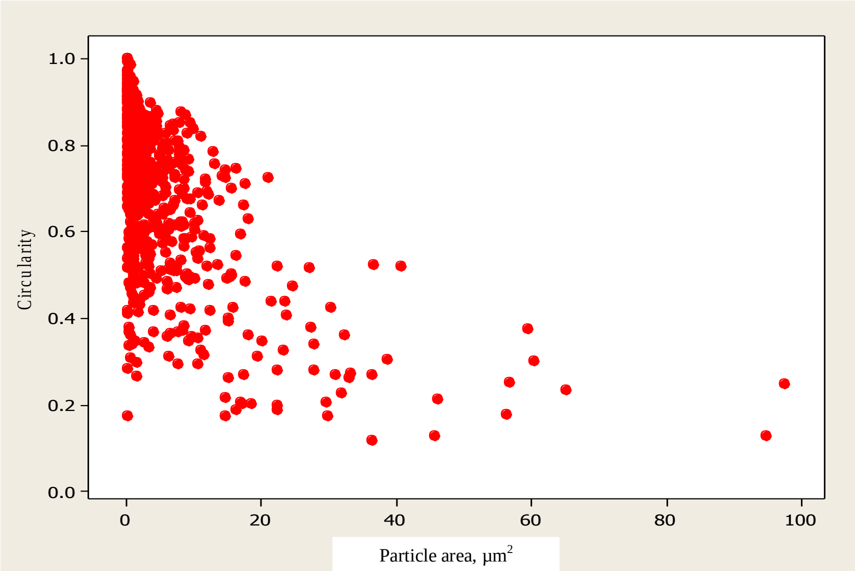

Figure 4.40: Circularity Vs. area of particles at region r=+1.8-2.5 mm of modified Al-7%Si piston alloy sample after 10 turns

Figure 4.41 shows the variation of microhardness along the diameter with the equivalent strain. The microhardness increases to a maximum at an equivalent strain of about 25, decreases slightly at equivalent strain of about 50 and then increases again gradually at a strain of about +100. Beyond the equivalent strain of +150, the microhardness along the diameter of the sample starts to increase gradually. This relationship has been reported in literature for alloys, which undergo strain hardening with slow recovery [18].

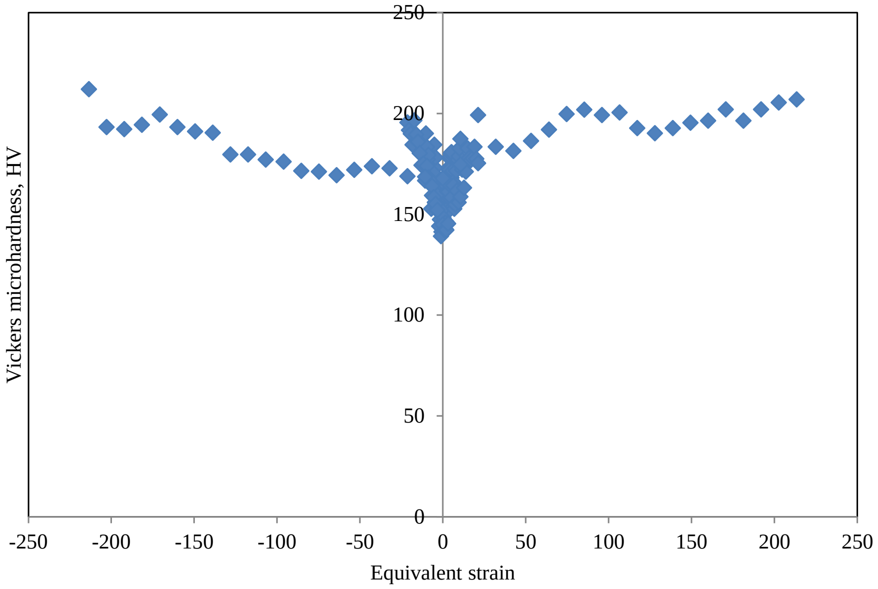

Figure 4.41: Vickers Microhardness versus equivalent strain for HPT processed modified Al-7%Si

4.4.4 Distribution of particles in HPT processed modified Al-7%Si piston alloy

Figures 4.42 and 4.43 show the 3-parameter Weibull distribution fit of the areas of particle for modified Al-7%Si piston alloy processed for $\frac{1}{4}$, $\frac{1}{2}$, 1 and 10 turns.

As shown, the particles at higher number of turns are heavily skewed towards the smaller particles.

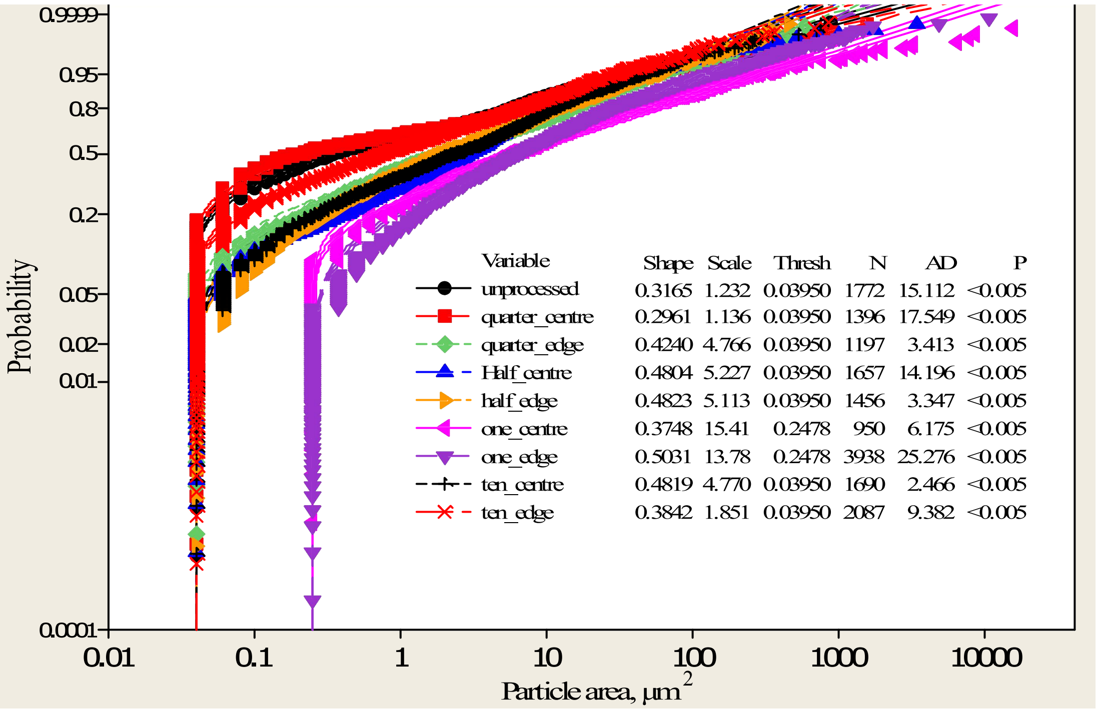

Variable	Shape	Scale	Thresh	N	AD	P
unprocessed	0.3165	1.232	0.03950	1772	15.112	<0.005
quarter_centre	0.2961	1.136	0.03950	1396	17.549	<0.005
quarter_edge	0.4240	4.766	0.03950	1197	3.413	<0.005
Half_centre	0.4804	5.227	0.03950	1657	14.196	<0.005
half_edge	0.4823	5.113	0.03950	1456	3.347	<0.005
one_centre	0.3748	15.41	0.2478	950	6.175	<0.005
one_edge	0.5031	13.78	0.2478	3938	25.276	<0.005
ten_centre	0.4819	4.770	0.03950	1690	2.466	<0.005
ten_edge	0.3842	1.851	0.03950	2087	9.382	<0.005

Figure 4.42: The 3-parameter Weibull probability plots of areas of particle in unprocessed and HPT-processed modified Al-7%Si piston alloy. The parameter, AD and P values are also shown

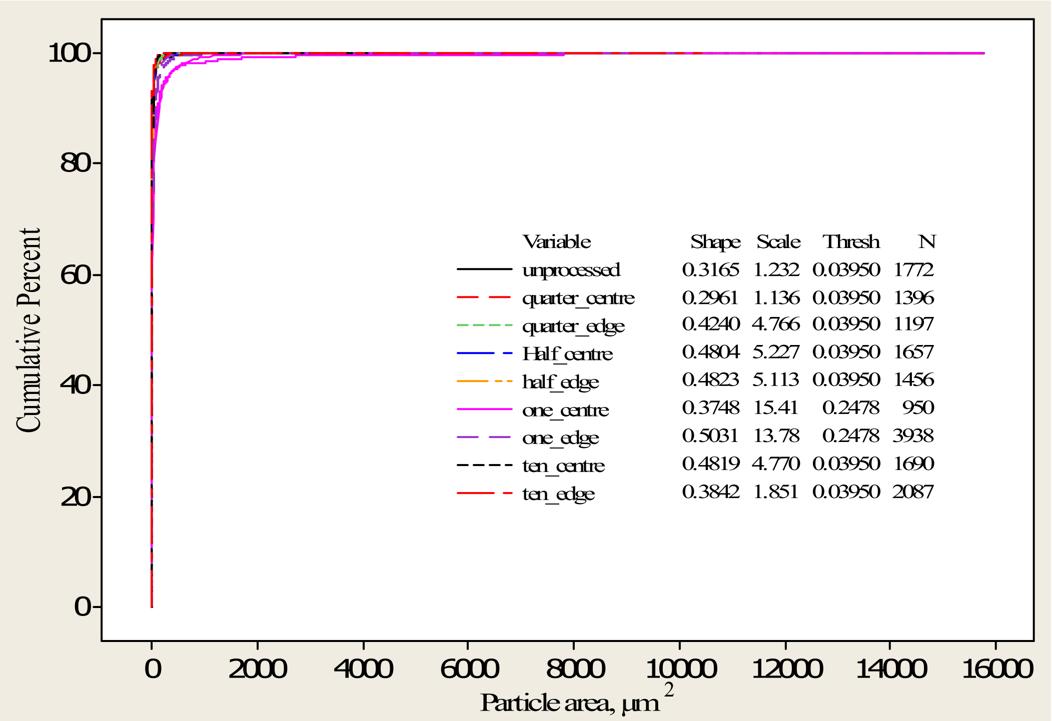

Figure 4.43: The 3-parameter Weibull cumulative distribution plots of areas of particle in unprocessed and HPT-processed modified Al-7%Si piston samples showing that the area population is heavily skewed to smaller particles after 10 HPT turns. The parameter values are also shown

Figures 4.44 and 4.45 show the relationship between circularity and area of particles for the modified Al-7%Si alloy. For illustration of the effect of HPT on circularity, the relationship is presented for $\frac{1}{4}$ and 10 turns. At $\frac{1}{4}$ turn, most of the particles have a circularity of less than 0.2. After 10 turns, shown in Figure 4.45b, most of the particles have a circularity of more than 0.2. The increase in the circularity of smaller particles may be part of the reason for the increase in microhardness after 10 turns.

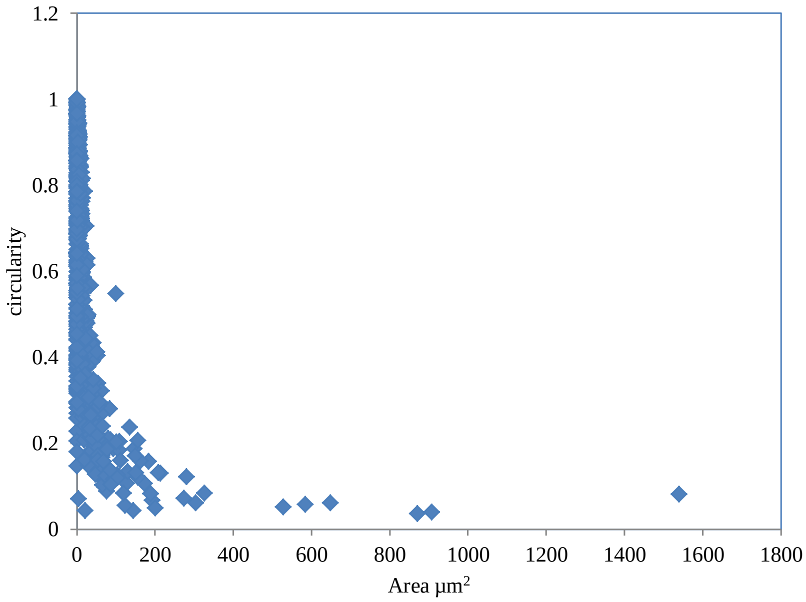

(a) $\frac{1}{4}$ turn-central region

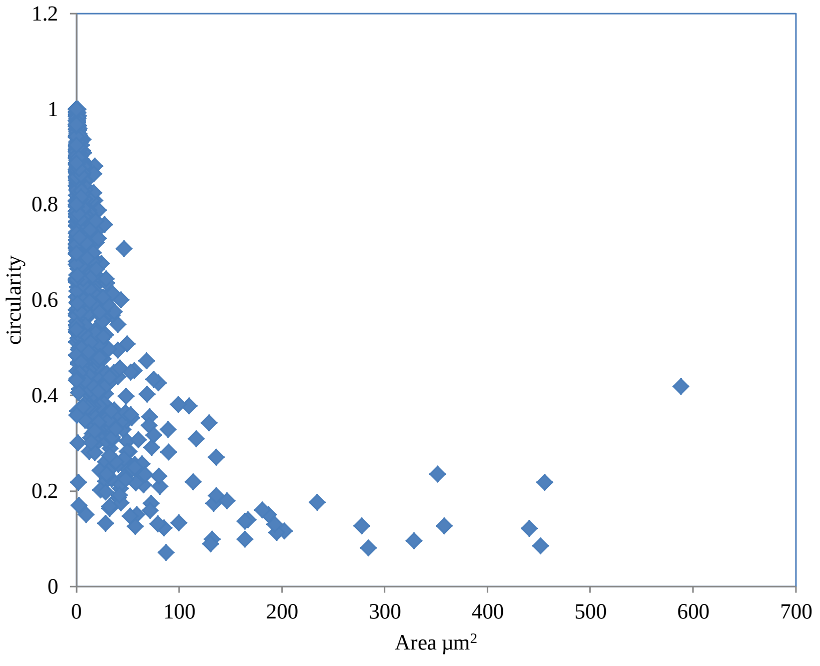

(b) $\frac{1}{4}$ turn-edge

Figure 4.44: Relationship between circularity and particle area for $\frac{1}{4}$-turn HPT-processed modified Al-7%Si alloy

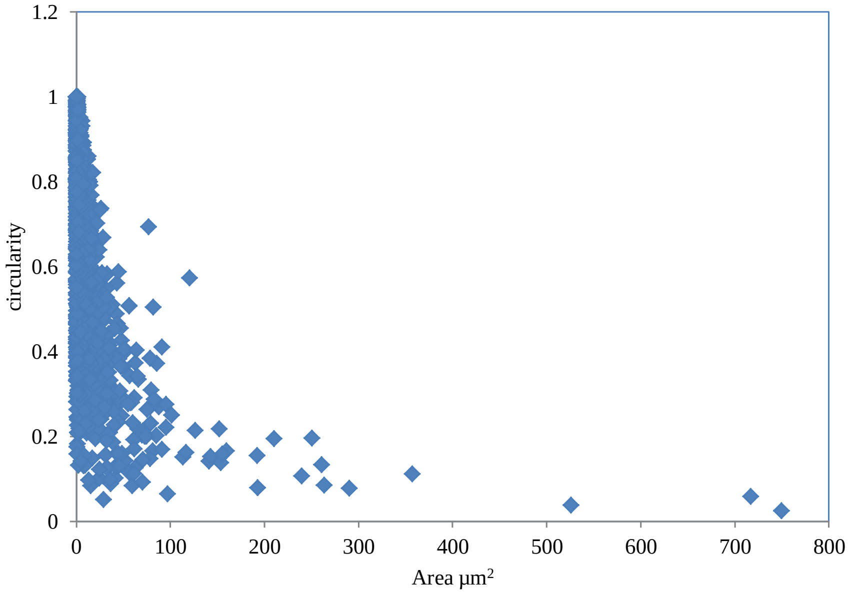

(a) 10 turns-central region

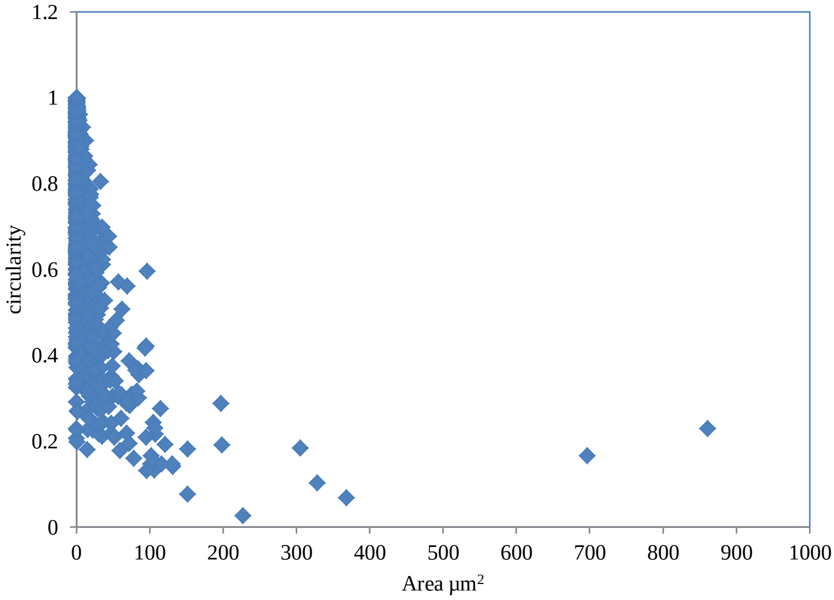

(b) 10 turns-edge

Figure 4.45: Relationship between circularity and particle area for 10-turn HPT-processed modified Al-7%Si alloy

4.5 Comparisons of Microhardness Evolution for Three Primary Alloys During High-pressure Torsion

Figure 4.46 compares the microhardness evolution of the three primary alloys after 10 turns. After 10 HPT turns, the microhardness values for modified and unmodified Al-7%Si piston alloy are nearly equal. This is because after 10 turns there were no major microstructural differences between the centre and edge of these samples. On the contrary, the microhardness for Al-12%Si exhibits inhomogeneity. This is because the microstructure at the edge appeared equiaxed and more refined than at the centre. This means that the concentration of Si content in Al-Si piston alloy reduces the refinement of the microstructure during HPT. This is because high Si content results in increase in concentration of Si-rich phases and as earlier stated, silicon is stronger than the rest of the phases and breaks down slowly during HPT. It can also be deduced that microhardness increases faster in the unmodified alloy than in the modified alloy. For instance, after $\frac{1}{4}$ turn, microhardness increase of 43% and 21% was recorded for unmodified and modified alloys respectively. This difference can be attributed to the observation that during HPT there occurs breakdown of the modified Si networks rather than the Si particles in the modified alloy, which does not bring a major change in properties of the modified alloy.

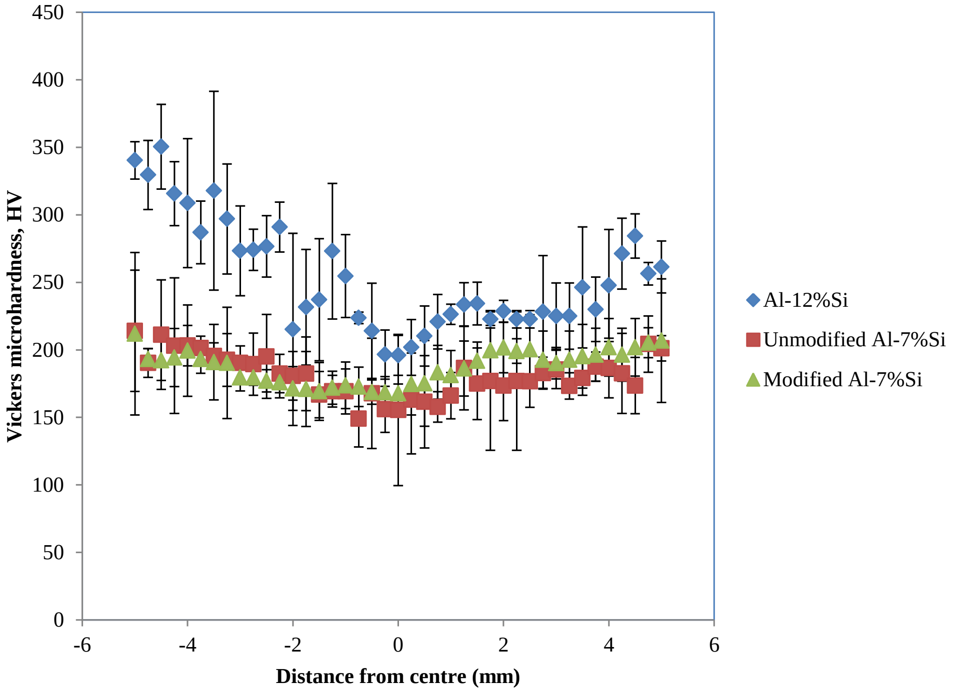

Figure 4.46: Comparison of microhardness evolution for the three primary alloys after ten turns

4.6 Summary of Discussions

4.6.1 Microhardness and microstructure as function of number of turns, N

The microhardness increased on HPT processing and with the increasing number of turns for all the three primary piston alloys. This is consistent with previous reports on HPT processing of commercial purity aluminium [35, 36, 56, 58], aluminium alloys [18–21, 31, 54, 55] and ECAP processing of pure aluminium [38–40]. As reported in literature [41, 75], this increase in microhardness can be attributed to microstructural refinement observed in this research. Microstructural observations revealed gradual break down of Si and other intermetallic particles with increasing number of turns. These microstructural observations were confirmed by a Weibull distribution which revealed that most of the particles tended to be skewed towards the smaller particle sizes with increase in number of turns. The increase in microhardness can also be attributed to increase in circularity of particles with number of HPT turns reported in the present results. It has been reported in literature [76, 77] that spherical or circular Si particles improve the mechanical properties of Al-Si piston alloys. This increase has also been attributed to evolution of LAGBs into HAGBs during HPT in previous studies [18, 19, 35]. However, grain size evolution (and hence grain boundaries) was not undertaken in this research and therefore can not been discussed.

The present results have shown that scatter bars in microhardness values of primary Al-Si piston alloys increase with number of turns. For all the three alloys, the largest scatter bars were observed after 10 turns. This is contrary to previous reports on high-pressure torsion of simple Al alloy systems [18–21,31,35,36,54–56,58]. This can be attributed to redistribution of small Si and other complex intermetallic particles within the matrix during HPT. The redistribution ensures that during a single hardness measurement, the four values obtained are for different phases, hence the scatter in the average microhardness value (see Figure 3.3 in chapter **??** for microhardness measurement procedure). A similar redistribution of particles was reported in an earlier study for ECAP-processed Al-3%Si and Al-7%Si alloys [78]. Microstructural observations further revealed that even after 10 turns, unbroken cracked and large Si and phases were still present. These observations could also be the reason for large scatter bars after 10 turns and also indicate that homogeneity and full microstructural refinement was not achieved after 10 HPT turns.

4.6.2 Microhardness and microstructure as functions of distance from centre

The microhardness increased with the increase in distance from the centre. This result is consistent with strain gradient theory [22, 66] and previous reports on HPT-processed alloys [18, 19, 21, 56]. This variation could be attributed to more microstructural refinement at edge than at the centre as revealed by the microstructural observations and Weibull probability and distribution plots of particle sizes. The circularity-particle size relationship revealed a higher circularity at the edge than at the centre for all number of turns. This is because there was higher break down at the edge than at the central region and as reported earlier [70], smaller particle sizes exhibit higher circularity than coarse particles. The higher circularity of particles at the edge further explains the occurrence of higher microhardness at the edge. Observations of evolution of spherical particles on HPT have been reported in literature for other Al-Si alloys [21, 54]

There is tendency for HPT-processed samples to evolve towards microhardness and microstructural homogeneity with increasing number of HPT turns [18,22,79]. In the present results, the homogeneity in microstructure was evaluated by the microhardness line profiles. The microhardness gradient along the diameter of the samples was seen to decrease with increase in number of turns. However, contrary to pure aluminium [35,36,56,58] and other alloys [18–21,31,54,55], homogeneity in microhardness was not achieved after 10 turns. There were still differences between the microstructure at the centre and edge for all the alloys after 10 turns. These observations were confirmed by the 3-parameter Weibull probability and cumulative plots in which there were still significant differences between the particle sizes at the centre and edge after 10 turns. These observations indicate that primary Al-Si piston alloys require straining beyond 10 turns to achieve full microstructural refinement. This is because, in relation to simple Al-Si alloy systems, Al-Si piston alloys are multi-component and contain complex phases, which evolve differently during HPT

CHAPTER FIVE

5.0 RESULTS AND DISCUSSIONS: SECONDARY Al-Si PISTON ALLOY DURING HIGH-PRESSURE TORSION

5.1 Introduction

This chapter presents microhardness and microstructural results and discussion of the secondary Al-Si piston alloy. The alloy studied is the recycled base Al-Si piston alloy (sample P) whose composition was given in Table 3.2. The results in this chapter are useful in evaluating HPT for improvement of properties of recycled materials.

5.2 Properties of as-received base Al-Si piston alloy

5.2.1 Microstructure

The optical micrographs in Figure 5.1 show the microstructure of the recycled base alloy. Secondary Al-Si piston alloys contain very high content of alloying elements and as a result, these alloys contain complex network of intermetallic particles. These particles include Al_3CuNi, Al_3Ni, Al_9FeNi (thick/thin plates) and Al_7Cu_4Ni [62]. Al_9FeNi is the most frequent phase in this alloy [62]. The microstructure also contains large and blocky primary Si particles and acicular eutectic Si. The phases in Figure 5.1 were identified by comparison with the previous results from the literature [62].

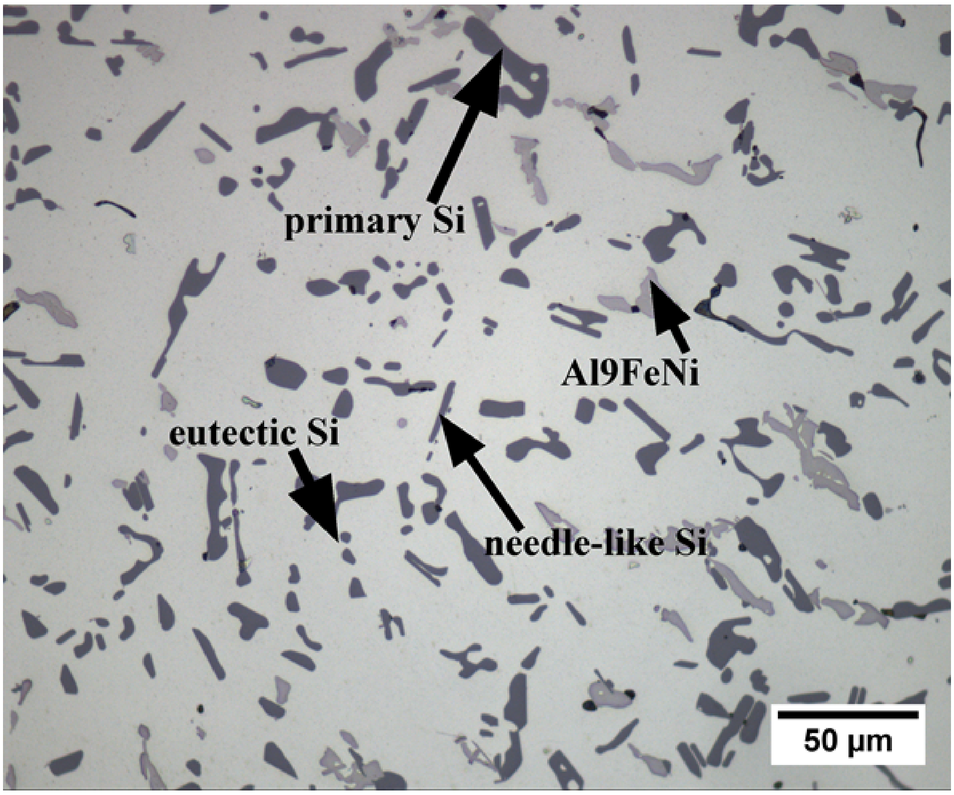

Figure 5.1: Optical micrograph of unprocessed secondary base Al-Si piston alloy

5.2.2 Microhardness

Figure 5.2 shows the microhardness along the diameter of the as-received secondary alloy. The microhardness is nonhomogeneous as illustrated by the scattering in the error bars. This scattering is due to difference in hardness exhibited by different particles (see Table 6.1 in Appendix B).

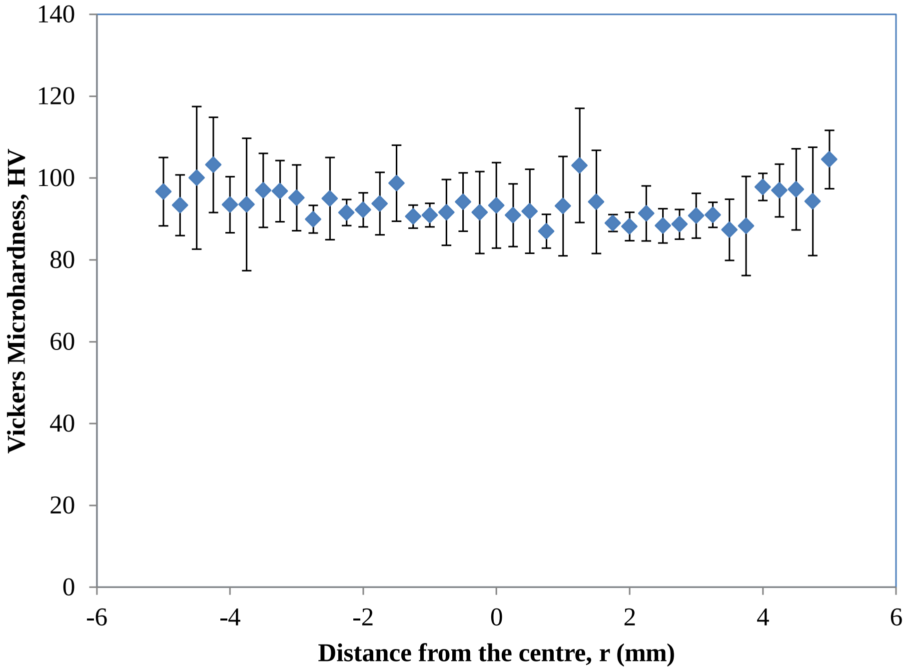

Figure 5.2: Vickers Microhardness across the diameter of as-received secondary Al-Si (sample P)

5.3 Microstructural evolution

Figure 5.3, shows the optical micrograph of recycled base Al-Si piston alloy after $\frac{1}{4}$, $\frac{1}{2}$, 1 and 10 HPT turns. After $\frac{1}{4}$ turn, Figure 5.3a, there is no change on the microstructure at the central region. However, broken intermetallic phases and very small cracks on Si can be observed in Figure 5.3b. These observations are clearly illustrated by the SEM image in Figure 5.4.

After $\frac{1}{2}$ turn, there are no major microstructural transformations observed at the central region except a few cracks on Si and intermetallic particles as shown in Figure 5.3c. The SEM image in Figure 5.5 clearly shows these broken intermetallic phases and cracks on Si particles. At the edge, there is more break down of the particles and silicon particles can now be observed (Figure 5.3d). This means that Si particles have broken down into small particles after $\frac{1}{2}$ turn at the edge of the sample as further illustrated by Figure5.6.

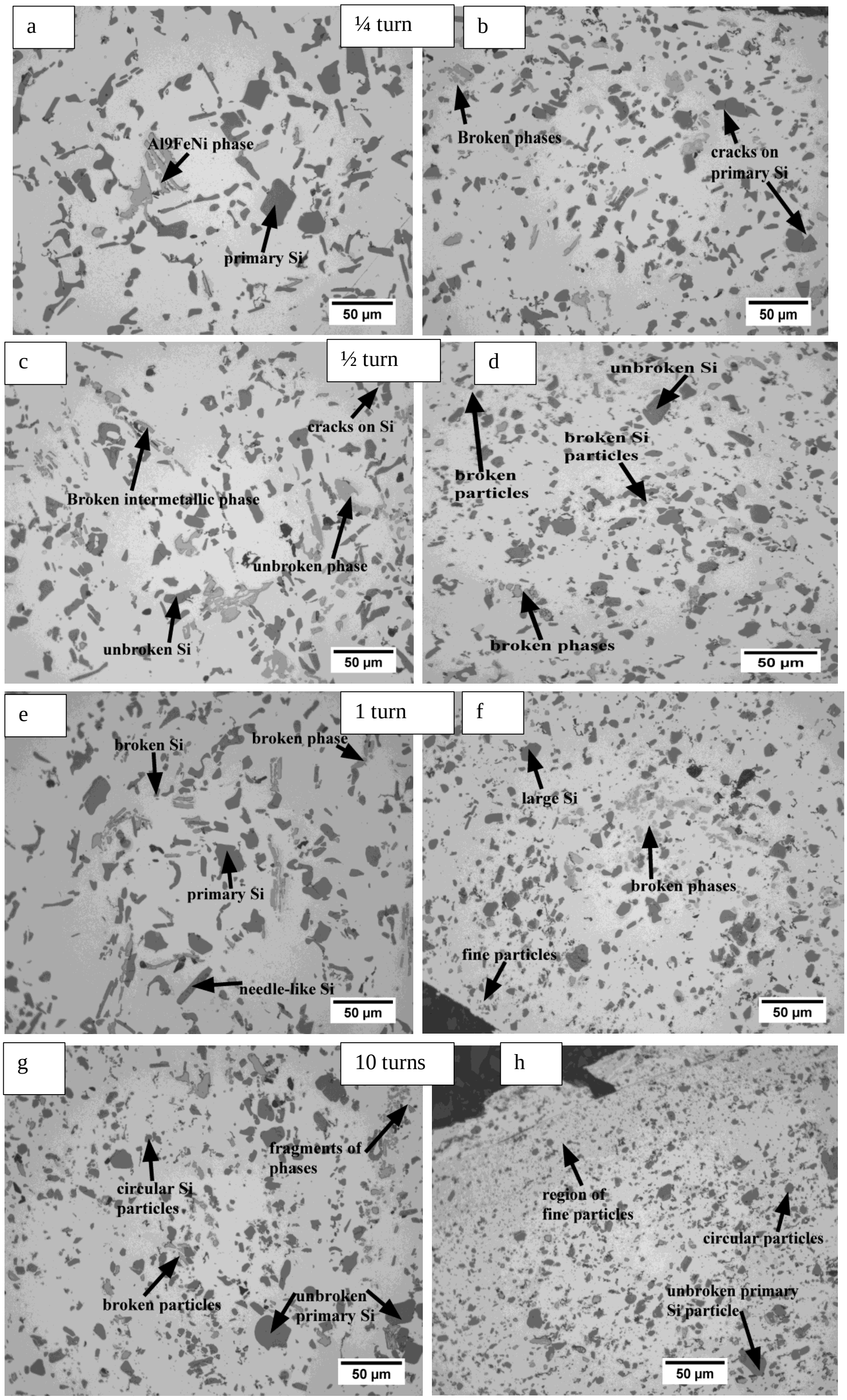

Figure 5.3: Optical micrographs showing microstructural evolution during HPT of recycled base alloy at different number of turns. Images a, c, e, g represent the microstructure at the central region while images b, d, f, h represent the microstructure at the edges.

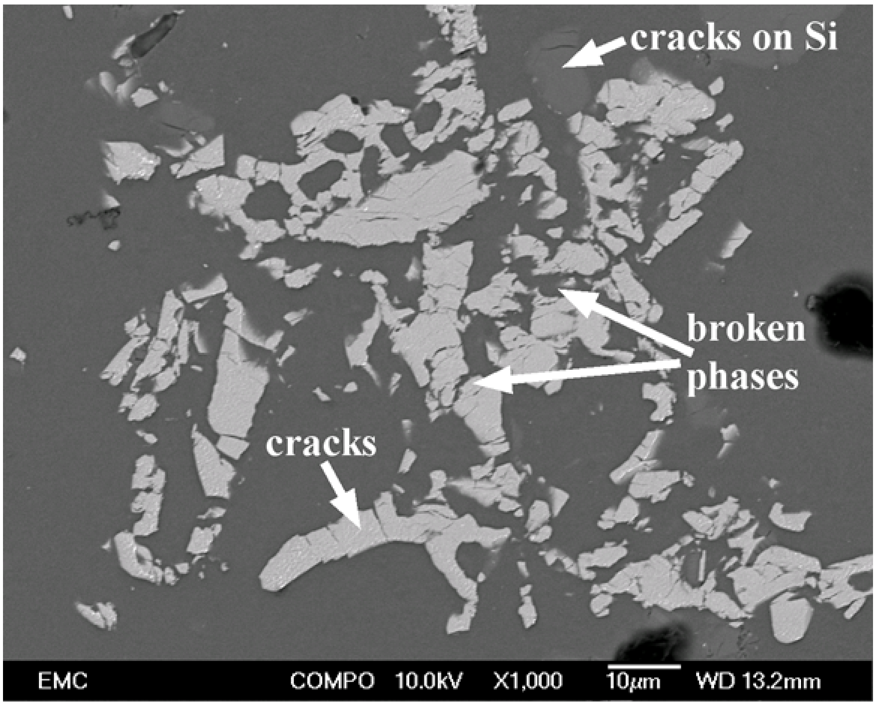

Figure 5.4: SEM image showing cracks on Si and intermetallic phases at the edge of recycled base alloy after $\frac{1}{4}$ HPT turns. Broken phases are also shown.

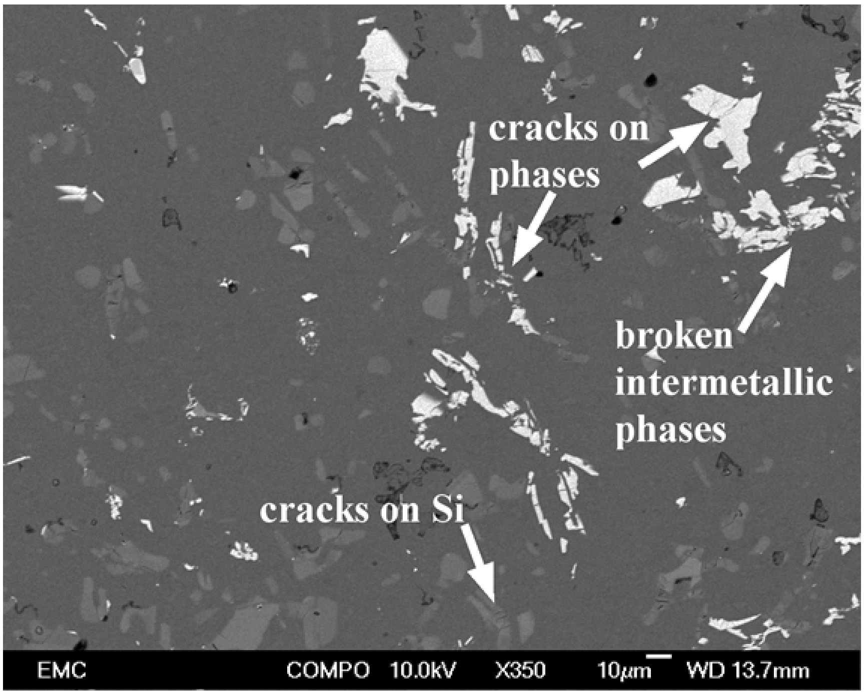

Figure 5.5: SEM image showing cracks on Si and broken intermetallic phases at the centre of recycled base alloy after $\frac{1}{2}$ HPT turn.

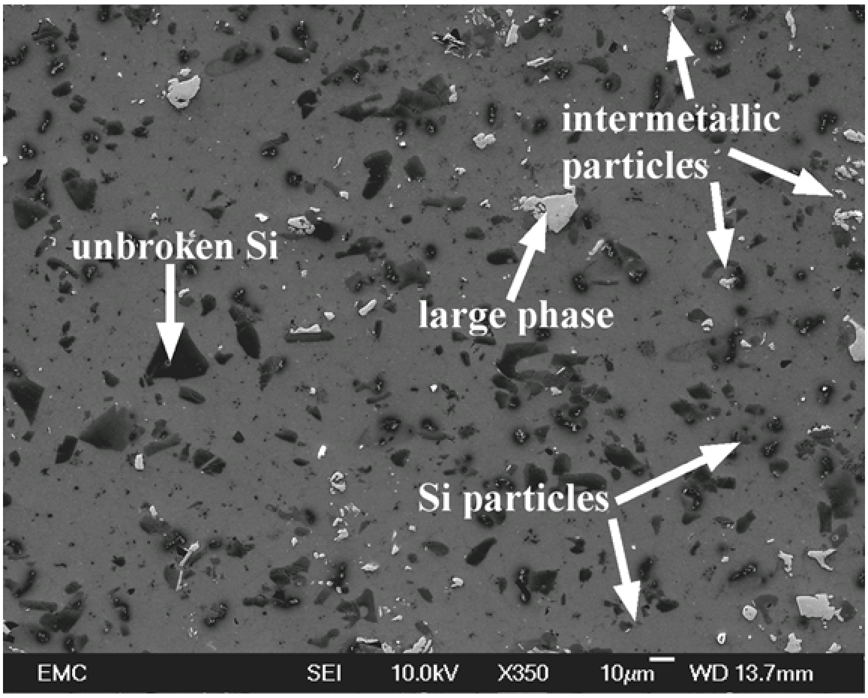

Figure 5.6: SEM image showing presence of Si particles at the edge of recycled base alloy after $\frac{1}{2}$ HPT turn.

The optical micrograph at the centre after 1 turn shown in Figure 5.3e does not reveal significant differences compared to the microstructure after $\frac{1}{4}$ turn at the central region. There are still many unbroken Si particles with a few broken intermetallic phases present as illustrated by the SEM micrograph in Figure 5.7. At the edge (Figure 5.3f), nearly all intermetallic phases have broken down and as such very few phases can be observed. However, there are still large and unbroken Si particles present. The SEM micrograph at the edge reveals few unbroken intermetallic phases, presence of near-circular particles and unbroken Si (Figure 5.8).

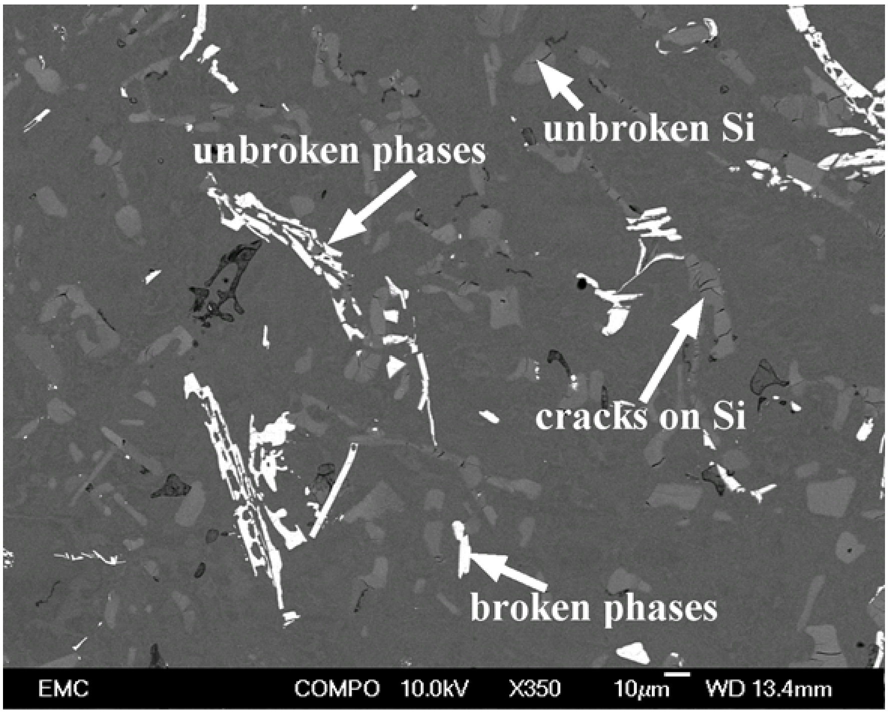

Figure 5.7: SEM image at the central region of recycled base alloy after 1 HPT turn. Unbroken phases and Si particles are shown.

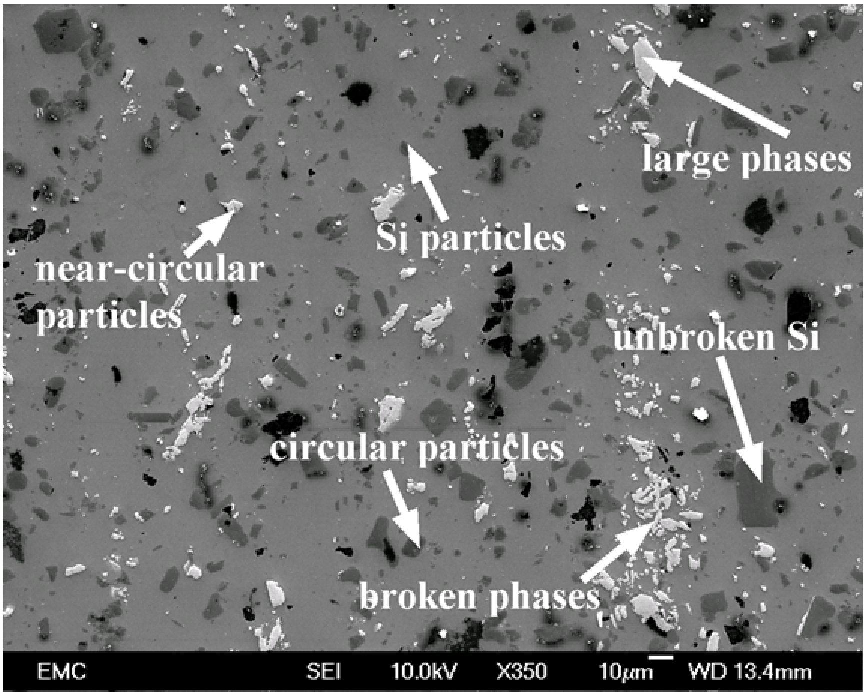

Figure 5.8: SEM image at the edge of recycled base alloy after 1 HPT turn. It shows the presence of unbroken Si particles and very few intermetallic phases.

After 10 turns, the optical micrograph at the central region reveals a more refined microstructure with very few unbroken intermetallic phases and Si particles (Figure 5.3g). The micrograph also shows the presence of circular particles at the central region. The SEM image in Figure 5.9 shows that large Si particles are still present at the central region of the base alloy after 10 turns. At the edges, the microstructure appears considerably refined consisting of a region of fine particles at the extreme edge of the sample as indicated in Figure 5.3h. However, a few primary silicon particles can still be observed. This means that Si particles have not fully broken down after 10 turns. Furthermore, the microstructure contains fine and circular Si and intermetallic particles as shown in Figure 5.10.

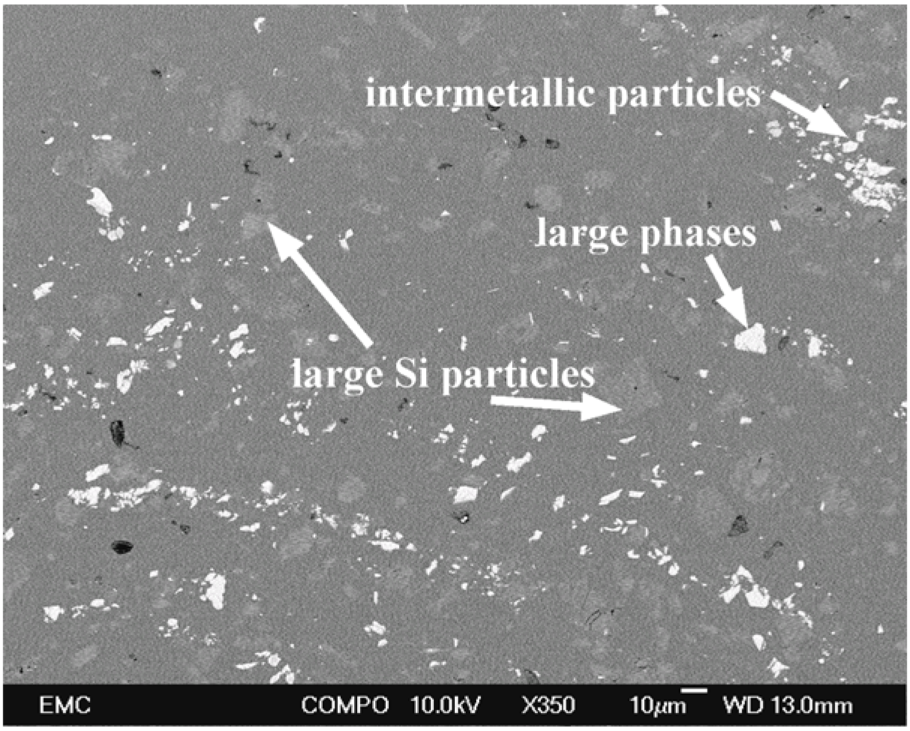

Figure 5.9: SEM image at the central region of recycled base alloy after 10 HPT turns showing a few unbroken phases and Si particles.

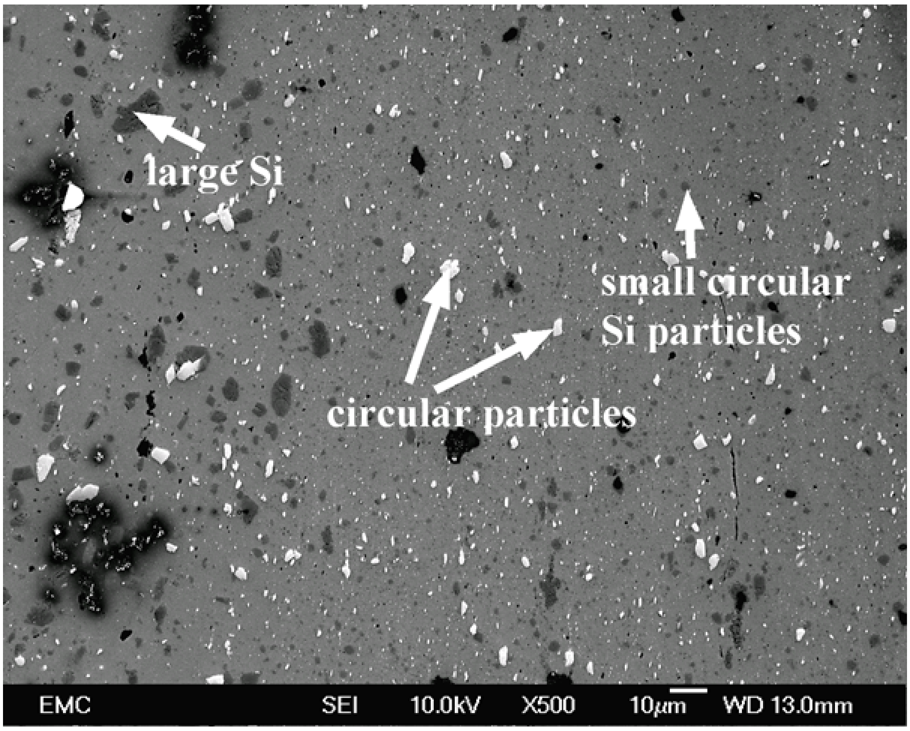

Figure 5.10: SEM image at the edge of recycled base alloy showing a considerably refined microstructure after 10 HPT turns.

5.4 Microhardness evolution

Figure 5.11 shows the microhardness along the diameter of secondary base Al-Si piston alloy after $\frac{1}{4}$, $\frac{1}{2}$, 1 and 10 HPT turns. The microhardness for as-received sample is also shown for comparison.

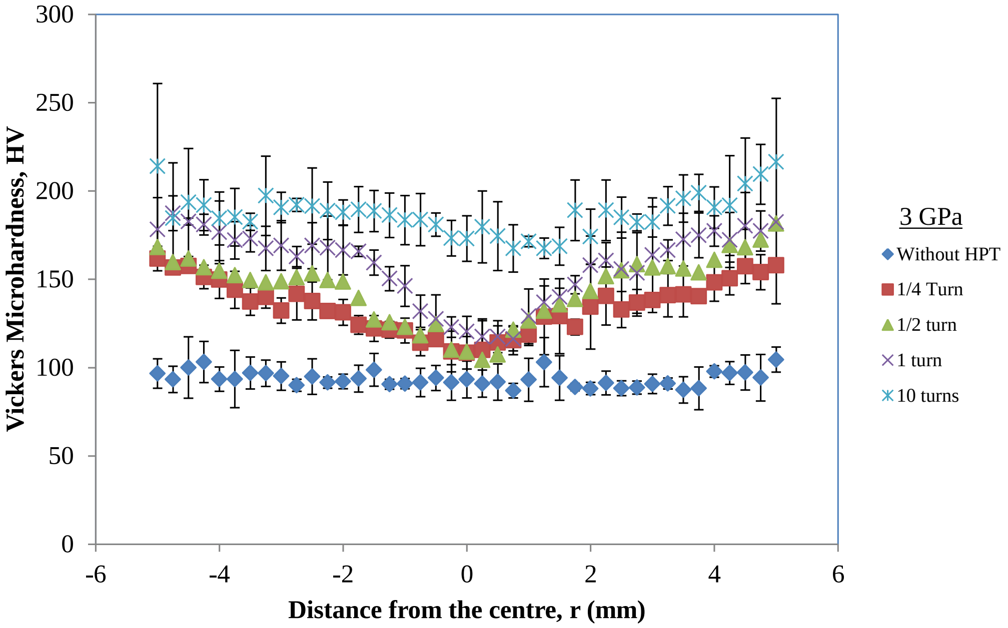

Figure 5.11: Vickers Microhardness across the diameter of the recycled base alloy for different number of turns

After $\frac{1}{4}$ turn, the microhardness has increased by ∼16% and ∼67% at central region and edges respectively from the microhardness of the as-received alloy. The small increase at the central region is due to very minimal break down observed in the microstructure around that region. The microhardness increases linearly up to diameter of ±2 mm followed by a decrease. The linear increase can be attributed to microstructural refinement observed towards the edge of the sample in subsection 5.3. The scatter bars are generally small and almost equal except at some random positions where larger scatter bars were observed.

There is no significant increase in microhardness after $\frac{1}{2}$ turn at the central region. This is because the microstructural features observed are similar to those observed after $\frac{1}{4}$ turn at the central region in Figure 5.3c (subsection 5.3). However, there is a slight increase in the microhardness at the edges with ~74% increase recorded. This is because considerable microstructural break down of intermetallic phases was observed at the edges. Generally, the scatter bars are larger and randomly distributed throughout the diameter.

After 1 turn, the microhardness has increased by ~29% and ~84% at the central region and at the edges respectively from the initial values of the as-received alloy. The microhardness gradient between the centre and edge decreases considerably. This shows the evolution of this alloy towards homogeneity and is due break down of more intermetallic and Si particles into smaller particles at the edge and central region of the alloy. Large and varied-sized scatter bars can be observed at the edges than at the central region. This can be attributed to more break down and redistribution of particles at the periphery of the alloy sample shown in Figure 5.3f (subsection 5.3).

The microhardness is nearly homogenous along the diameter after 10 HPT turns as shown in Figure 5.11. This is because micrographs at both the central region and edge revealed considerable refinement of the microstructure (Figures 5.9 and 5.10). However, the microhardness values around the extreme edges are higher. This can be attributed to the presence of the region of very fine particles at the extreme edge. The size of the scatter bars have increased significantly along the diameter after 10 turns. The presence of unbroken primary Si particles and intermetallic phases after 10 turns maybe the reason for large scatter bars.

Figure 5.11 shows that all the microhardness line profiles are symmetrical about the central region which indicates that refinement is slower at the central region than at the edge. The microhardness increase around the central region after $\frac{1}{4}$, $\frac{1}{2}$ and 1 turns is very small. This is consistent with the microstructural observations in which no microstructural transformation was reported at the central region after these number of turns.

Figure 5.12 shows the variation of vickers microhardness with the equivalent strain for recycled piston alloy P. As shown, the microhardness increases rapidly up to an equivalent strain of 25, then decreases slightly and increases again beyond the strain of 100. This behavior is similar to what has been reported in previous studies on HPT processed Aluminium alloys and is exhibited by materials which undergo strain hardening with slow recovery [18,19,56].

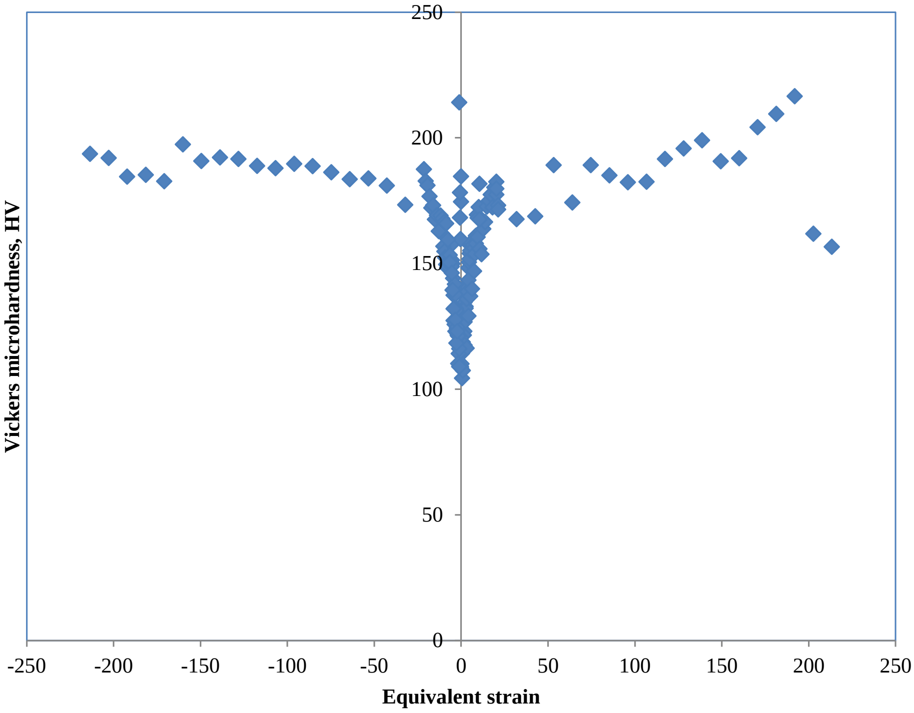

Figure 5.12: Vickers Microhardness variation with equivalent strain for the recycled base alloy

5.5 Distribution of particles in HPT processed recycled base Al-Si piston alloy

Figures 5.13 and 5.14 show the 3-parameter Weibull distribution of particle areas for base alloy processed up to 10 turns. It can be seen that most of particles at the central region are skewed relatively towards the larger particles. It is also observed that the distribution plots for $\frac{1}{4}$, $\frac{1}{2}$ and 1 turns at the central regions are very close to each other. This is consistent with the microstructural and microhardness observations in which there were no microstructural changes reported at the central region after these number of turns. The distribution plots at the centre and edge are closer to each other after 10 turns. This confirms the occurrence of microstructural homogeneity illustrated by the microhardness measurements after 10 turns in subsection 5.4. The evolution towards homogeneity in this alloy is further represented by the circularity-particle size relationships in Figures 5.15 and 5.16. As shown, the circularity of particles increased considerably both at the centre and edge after 10 turns. After $\frac{1}{4}$ turn, the particles at the edge have more circularity than at the central region. These observations support the microhardness results reported after $\frac{1}{4}$ and 10 turns.

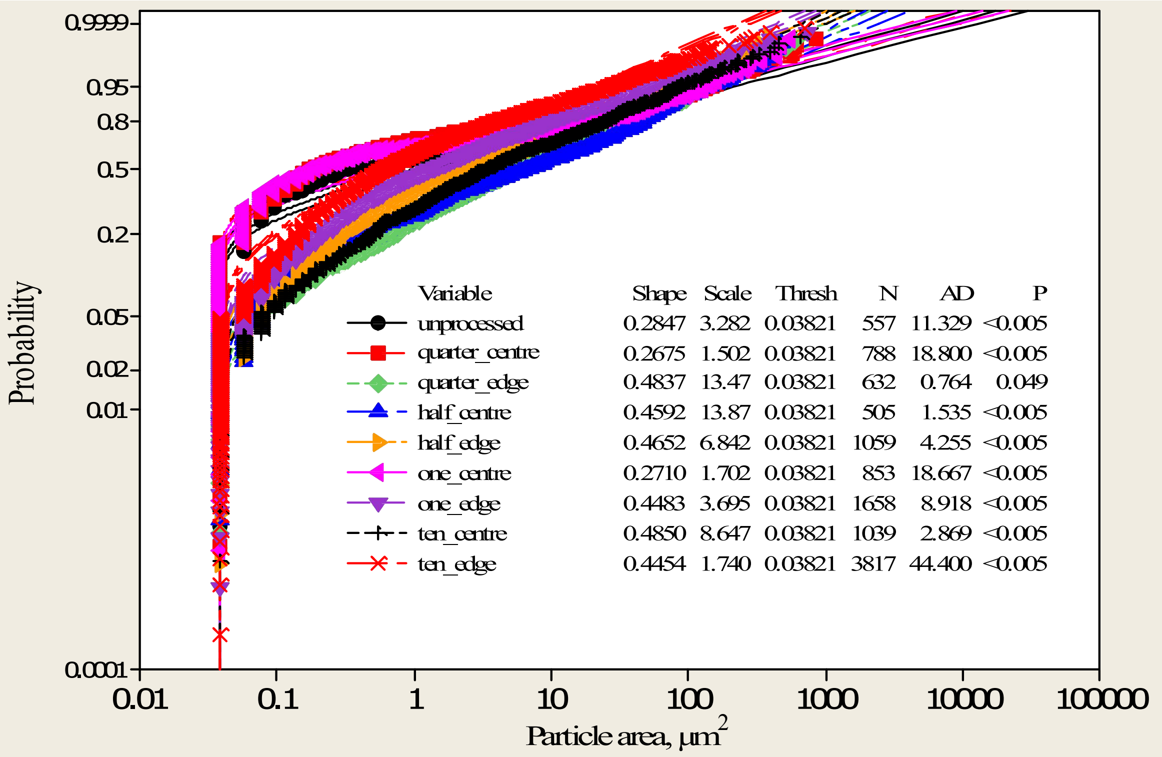

	Variable	Shape	Scale	Thresh	N	AD	P
●	unprocessed	0.2847	3.282	0.03821	557	11.329	<0.005
■	quarter_centre	0.2675	1.502	0.03821	788	18.800	<0.005
◆	quarter_edge	0.4837	13.47	0.03821	632	0.764	0.049
▲	half_centre	0.4592	13.87	0.03821	505	1.535	<0.005
▶	half_edge	0.4652	6.842	0.03821	1059	4.255	<0.005
◀	one_centre	0.2710	1.702	0.03821	853	18.667	<0.005
▼	one_edge	0.4483	3.695	0.03821	1658	8.918	<0.005
+	ten_centre	0.4850	8.647	0.03821	1039	2.869	<0.005
×	ten_edge	0.4454	1.740	0.03821	3817	44.400	<0.005

Figure 5.13: The 3-parameter Weibull probability plots of areas of particle in unprocessed and HPT-processed recycled base Al-Si piston alloy. The parameter, AD and P values are also shown

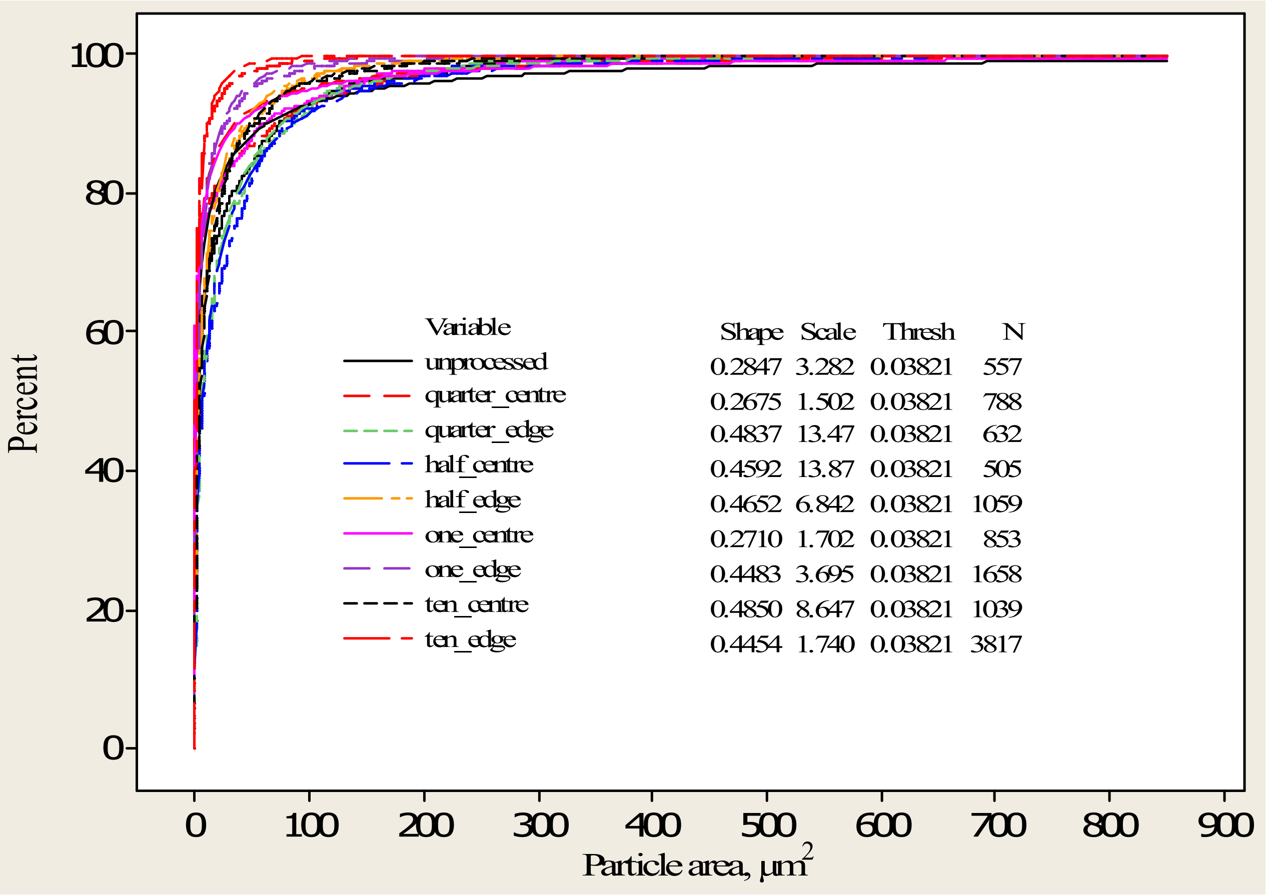

Figure 5.14: The 3-parameter Weibull cumulative distribution plots of areas of particle in unprocessed and HPT-processed recycled base Al-Si piston alloy samples showing that the area population is heavily skewed to smaller particles after 10 HPT turns. The parameter values are also shown

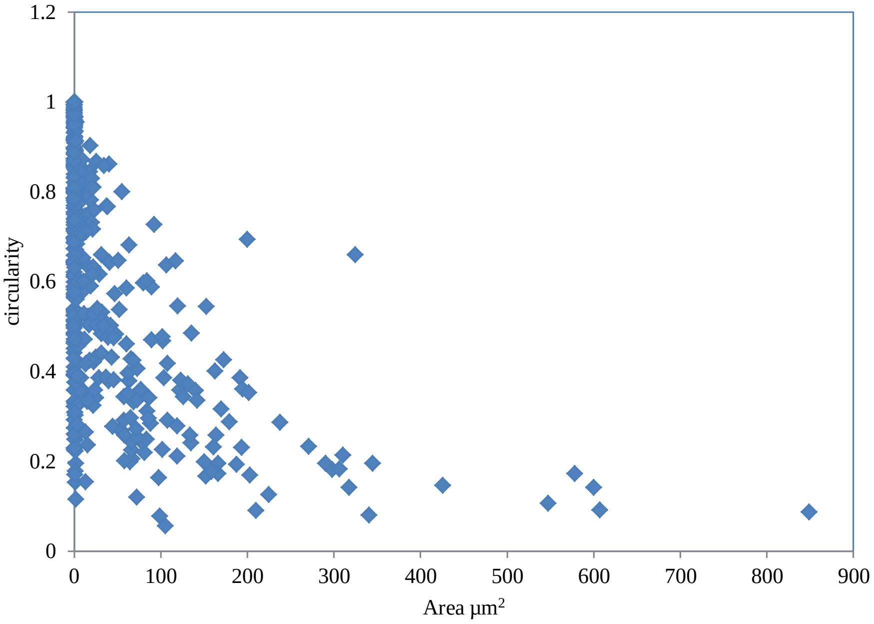

(a) $\frac{1}{4}$ turn-central region

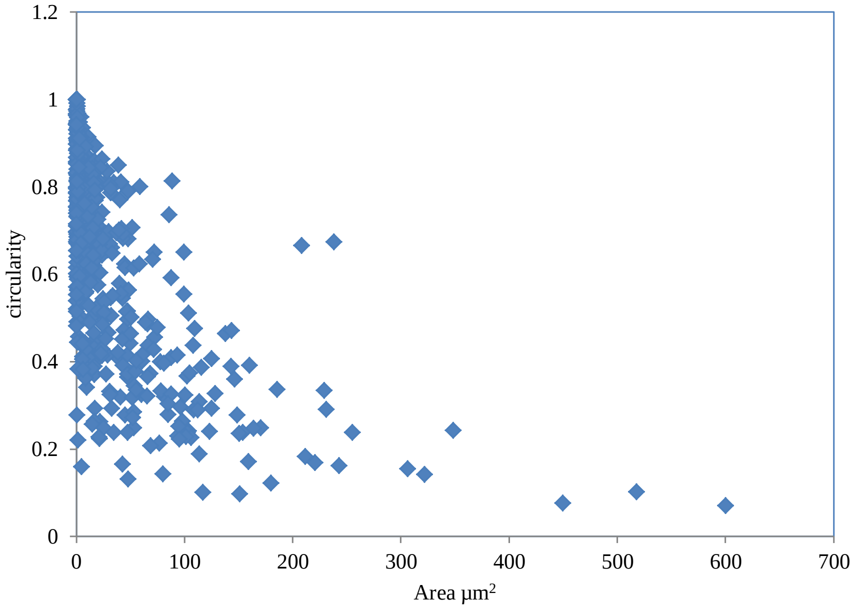

(b) $\frac{1}{4}$ turn-edge

Figure 5.15: Relationship between circularity and particle area for $\frac{1}{4}$-turn HPT-processed recycled base Al-Si piston alloy

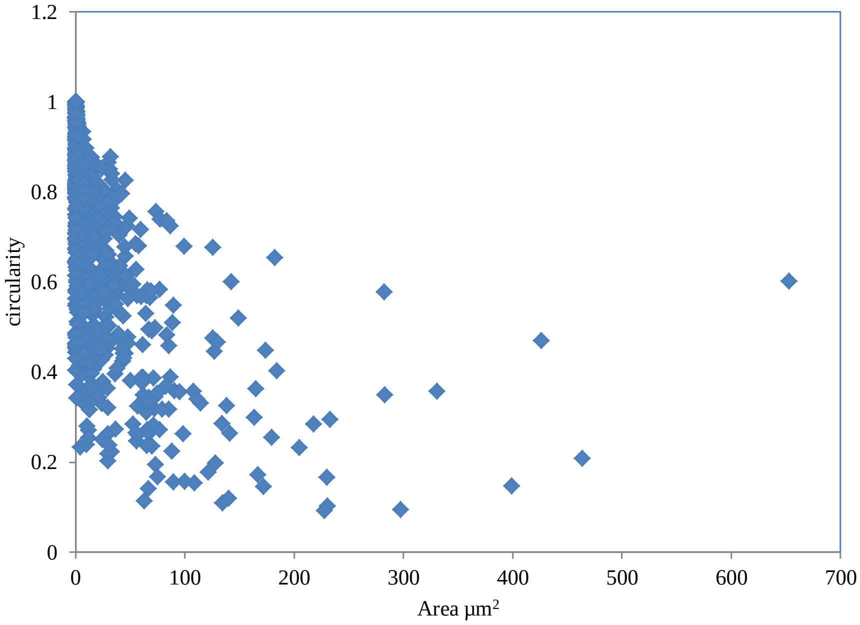

(a) 10 turns-central region

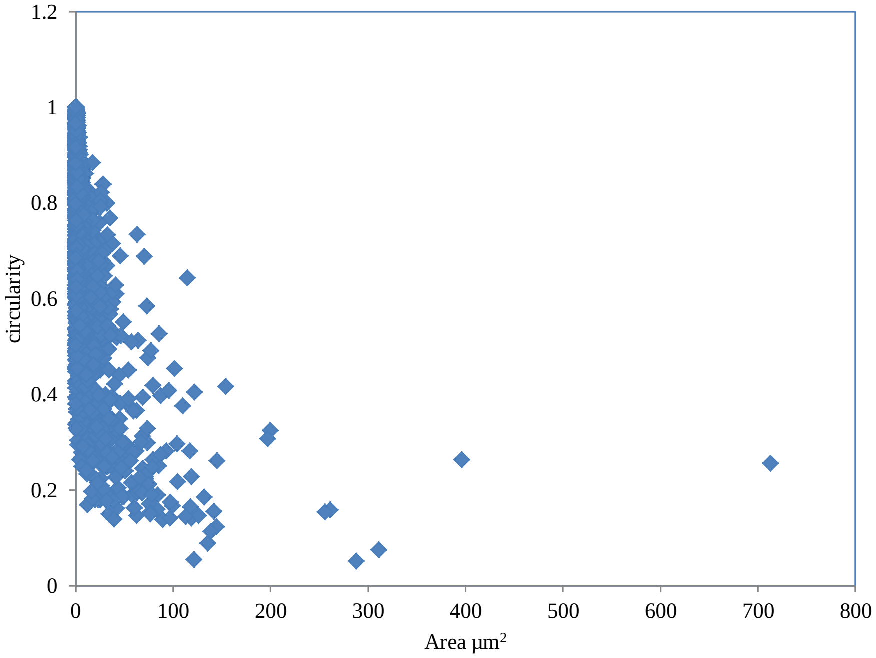

(b) 10 turns-edge

Figure 5.16: Relationship between circularity and particle area for 10-turn HPT-processed recycled base Al-Si piston alloy

CHAPTER SIX

6.0 CONCLUSION AND RECOMMENDATION

6.1 Conclusion

There is no much difference observed, in terms of microstructural and microhardness evolution, between the primary and secondary Al-Si piston alloys. The microhardness increases after high-pressure torsion for all the alloys. In all the alloys, the coarse silicon structures and other intermetallic particles break down into small and circular particles after 10 HPT turns. The presence of large and unbroken phases and silicon particles after 10 turns indicates that full microstructural refinement has not been achieved after 10 turns.

There are microhardness gradients along the diameter of all the alloys as revealed by the microhardness line profiles even after 10 turns. This is an indication of nonhomogeneous microstructural refinement in Al-Si piston alloys.

All the alloys have shown the tendency to evolve towards microstructural homogeneity with increasing number of turns. For all the alloys, a finer microstructure has been observed at the edge compared to the central region for all number of HPT turns. The microstructure at the central region for all the alloys was observed to contain relatively large and unbroken phases even after 10 turns. All the alloys exhibit a non-monotonic microhardness-strain relationship; which means that both primary and secondary cast Al-Si piston alloys undergo strain hardening with slow recovery during severe plastic deformation.

There is improvement in the microstructure and microhardness of the secondary Al-Si piston alloy as revealed by the results presented in Chapter 5. These results indicate that HPT can be used as a post-recycling method to improve the strength of the materials for various applications.

An important output of this work is the development of a new method of measuring microhardness along the diameter of HPT samples.It uses more local points (40 points) along the sample diameter. The use of more measurement points renders this new method statistically more accurate than the methods in literature. Since the measurements obtained through this method are comparable to the microstructure properties, this method is suitable for microhardness characterization of HPT processed samples.

6.2 Recommendations for Future Work

This research recommends the following studies for future work:

- High-pressure torsion should be undertaken on these alloys for more than 10 turns to establish the number of turns necessary to cause full and homogenous refinement of the microstructure.

- Grain size, grain boundary and dislocation evolutions should be undertaken on HPT-processed Al-Si piston alloys to gain a deeper understanding into the deformation mechanisms of these alloys during SPD. These studies require use of TEM, which could not be accessed in the present investigations.
- Further studies into other mechanical properties such as thermal stability, wear and corrosion resistances on HPT-processed Al-Si piston alloys are recommended.
- To upscale these results to full scale production, a high-pressure torsion equipment suitable for implementation in the existing engine piston production lines should be developed.

REFERENCES

[1] Valiez R.Z., Islamgaliev R.K., Alexandrov I.V., "Bulk nanostructured materials from severe plastic deformation," *Progress in Materials Science*, vol. 45, pp. 103–189, 2000.

[2] Cui Q., Ohori K., "Grain refinement of high purity aluminium by asymmetric rolling," *Materials Science and Technology*, vol. 16, pp. 1095–1101, 2000.

[3] Verlinden B., "Severe plastic deformation of metals," *Association of Metallurgical Engineers Serbia and Montenegro*, pp. 165–182, 2004.

[4] Dobatkin S.V., Bastarache E.N., Sakai G., Fujita T., Horita Z., Langdon T.G., "Grain refinement and superplastic flow in an aluminium alloy processed by high-pressure torsion," *Materials Science and Engineering A*, vol. 408, pp. 141–146, 2005.

[5] McClintock, F., Argon, A.S., *Mechanical Behavior of Materials.* Addison Wesley, 1966.

[6] Valiez R.Z., Salimoneko D.A., Tsenev N.K., Berbon P.B., Langdon T.G., "Observations of high strain rate superplasticity in commercial aluminium alloys with ultrafine grain sizes," *Scripta Materialia*, vol. 37, pp. 1945–1950, 1997.

[7] Valiev R.Z., Alexandrov I.V., Zhu Y.T., Lowe T.C., "Paradox of strength and ductility in metals processed by severe plastic deformation," *Journal of Material Resources*, vol. 17.1, pp. 5–8, 2002.

[8] Valiev, R.Z, "Paradoxes of severe plastic deformation," *Advanced Engineering Materials*, vol. 5, pp. 296–300, 2003.

[9] Valiev R.Z., Kozlov E.V., Ivanov Y. F., Lian J., Nazarov A.A., & Baudelet B., "Deformation behaviour of ultra-fine-grained copper," *Acta Metallurgica et Materialia*, vol. 42 (7), pp. 2467–2475, 1994.

[10] Yang Z., Welzel U., "Microstructure-microhardness relation of nanostructured nickel produced by high-pressure torsion," *Material Letters*, vol. 59, pp. 3406–3409, 2005.

[11] Zhilyaev A.P., Nurislamova G.V., Kim B.K., Baro M.D., Szpunar J.A., Langdon T.G., "Experimental parameters influencing grain refinement and microstructural evolution during high pressure torsion," *Acta Materialia*, vol. 51, pp. 753–765, 2003.

[12] Vorhauer A., Pippan R., "On the homogeneity of deformation by high-pressure torsion," *Scripta Materialia*, vol. 51, pp. 9–21, 2004.

[13] Jiang H., Zhu Y.T., Butt D.P., Alexandrov I.V., Lowe T.C., "Microstructural evolution, microhardness and thermal stability of hpt-processed cu," *Materials Science and Engineering A*, vol. 290, pp. 128–132, 2000.

[14] Zhilyaev A.P., McNelley T.R., Langdon T.G., "Evolution of microstructure and microtexture in face centered metals during high-pressure torsion," *Journal of Materials Science*, vol. 42, pp. 15–17, 2007.

[15] Wei Q., Zhang H.T., Schuster B.E., Ramesh K.T., Valiev R.Z., Kecskes L.J., Dowding R.J., Magness L., Cho K., "Microstructure and mechanical properties of super-strong nanocrystalline tungsten processed by high-pressure torsion," *Acta Materialia*, vol. 54, pp. 40–79, 2006.

[16] Wei Q., Pan Z.L., Wu X.L., Schuster B.E., Kecskes L.J., Valiev R.Z., "Microstructure and mechanical properties at different length scales and strain rates of nanocrystalline tantalum produced by high-pressure torsion," *Acta Materialia*, vol. 59, pp. 2423–2436, 2011.

[17] Sakai G., Horita Z., Langdon T.G., "Grain refinement and superplasticity in an aluminum alloy processed by high-pressure torsion," *Materials Science and Engineering A*, vol. 393, pp. 344–351, 2005.

[18] Mungole T., Nadammal N., Dawra K., Kumar P., Kawasaki M., Langdon T.G., "Evolution of microhardness and microstructure in a cast aluminium-7% silicon alloy during high pressure torsion," *Journal of Material Science*, vol. 7061, pp. 3–8, 2012.

[19] Zhilyaev A.P., Garcia-Infanta J.M., Carren O F., Langdon T.G., Ruano O.A., "Particle and grain growth in an aluminium-silicon alloy during high-pressure

torsion," *Scripta Materialia*, vol. 57, pp. 763–765, 2007.

[20] Sabbaghianrad S., Langdon T.G., Kawasaki M., "Microstructural evolution and the mechanical properties of an aluminum alloy processed by high-pressure torsion," *Journal of Materials Science*, vol. 47, pp. 7789–7795, 2012.

[21] Rajinikanth V., Venkateswarlu K., Sen M.K., Das M., Alhajeri S.N., Langdon T.G., "Influence of scandium on an aluminiuml-2% silicon processed by high pressure torsion," *Materials Science and Engineering A*, vol. 528, pp. 1702–1706, 2011.

[22] Zhilyaev A.P., Langdon T.G., "Using high-pressure torsion for metal processing: Fundamentals and applications," *Progress in Materials Science*, vol. 53, pp. 893–979, 2008.

[23] Zhu Y.T., Lowe T.C., Langdon T.G., "Performance and applications of nanostructured materials produced by severe plastic deformation," *Scripta Materialia*, vol. 51, pp. 825–830, 2004.

[24] Harai Y., Ito Y., Horita Z., "High-pressure torsion using ring specimens," *Scripta Materialia*, vol. 58, pp. 469–472, 2008.

[25] Reichstein S., Konrad P., Kenningley S., Dornenburg F., "Remelt microstructure modification of piston materials for high stress and temperature conditions," *Aachener Kolloquium and Motorentechnik*, vol. 16, pp. 1241–1249, 2007.

[26] Reichstein S., Weiss R., Kenningley S., Lades K., Konrad P., Doernenburg F., “High-perfomance cast aluminium pistons for highly efficient diesel engines,” *SAE International*, vol. 01-1438, pp. 1–8, 2007.

[27] Angella G., Bassani P., Tuissi A., Vedani M., “Intermetallic particle evolution during ecap processing of a 6082 alloy,” *Materials Transactions*, vol. 45 (7), pp. 2182–2186, 2004.

[28] Pashinska E., Varyukhin V., Zavdoveev A., Tkacheko V., & Glazunov F., “Effect of high-angle grain boundaries on mechanical properties of low-carbon steel subjected to warm severe plastic deformation,” *Donetsk Institute for Physics and Engineering, NAS of Ukraine*, 2008.

[29] Zeynali E., Bisadi H , “Comparing plastic deformations produced by hpt and ecap processes using the finite element analysis method,” *International Journal of Mechanics and Applications*, vol. 2(1), pp. 20–24, 2012.

[30] Bridgeman P.W., “On torsion combined with compression,” *Journal of Applied Physics*, vol. 14, p. 273, 1943.

[31] Alhajeri S.N., *Processing of Aluminium and Titanium alloys by Severe Plastic Deformation.* PhD thesis, University of Southampton, 2010.

[32] Degtyarev M.V., Chashchukina T.I., Voronova L.M., Davydova LS., Pilyugin V.P., “Deformation strengthening and structure of structural steel upon shear

under pressure," *Physics of Metals and Metallography*, vol. 90, pp. 604–608, 2000.

[33] Loucif A., Figuiredo R.B., Baudin T., Brisset F., Langdon T.G., "Microstructural evolution in an aluminium-6061 alloy processed by high-pressure torsion and rapid annealing," *Materials Science Forum*, vol. 667-669, pp. 223–228, 2011.

[34] Xu C., Horita Z., Langdon T.G, "The evolution of homogeneity in processing by high-pressure torsion," *Acta Materialia*, vol. 55, pp. 203–212, 2007.

[35] Zhilyaev A.P., Oh-ishi K., Langdon T.G., McNelley T.R., "Microstructural evolution in commercial purity aluminum during high-pressure torsion," *Materials Science and Engineering A*, vol. 410-411, pp. 277–280, 2005.

[36] Xu C., Horita Z., Langdon T.G., "Microstructural evolution in pure aluminum in the early stages of processing by high-pressure torsion," *Materials Transactions*, vol. 51, pp. 2–7, 2010.

[37] Iwahashi Y., Wang J., Horita Z., Nemoto M., "Principle of equal channel pressing of ultra-fine grained materials," *Scripta Materialia*, vol. 35, pp. 143–146, 1996.

[38] Xu C., Furukawa M., Horita Z., Langdon T.G., "The evolution of homogeneity and grain refinement during equal-channel angular pressing: A model for grain

refinement in ecap," *Materials Science and Engineering A*, vol. 398, pp. 66–76, 2005.

[39] Prell M., Xu C., Langdon T.G., "The evolution of homogeneity on longitudinal sections during processing by ecap," *Materials Science and Engineering A*, vol. 480, pp. 449–455, 2008.

[40] Xu C., Langdon T.G., "The development of hardness homogeneity in aluminiun and an aluminium alloy processed by ecap," *Journal of Material Science*, vol. 42, pp. 1542–1550, 2007.

[41] Tsai T.L., Sun P.L., Kao P.W., Chang C.P., "Microstructure and tensile properties of a commercial 5052 aluminum alloy processed by equal channel angular extrusion," *Materials Science and Engineering A*, vol. 342, pp. 144–151, 2003.

[42] Xu C., Zhilyaev A.P., Horita Z., Langdon T.G., "Factors influencing the development of homogeneity in disks processed by high-pressure torsion," *Materials Science Forum*, vol. 584-586, pp. 3–8, 2008.

[43] Horita Z., Smith D.J., Furukawa M., Nemoto M., Valiev R.Z., Langdon T.G., "An investigation of grain boundaries in submicrometer-grained Al-Mg solid solution alloys using high-resolution electron microscopy," *Journal of Materials Research*, vol. 11, pp. 1880–1890, 1996.

[44] Horita Z., Smith D.J., Furukawa M., Nemoto M., Valiev R.Z., Langdon T.G., "Observations of grain boundary structure in submicrometer-grained Cu and Ni using high-resolution electron microscopy," *Journal of Materials Research*, vol. 13, pp. 446–450, 1998.

[45] Gill S., Houtte P.V, Aernoudt E., "Large strain work hardening and textures," *Progress in Materials Science*, vol. 25, pp. 69–412, 1980.

[46] Hughes D.A., Hansen N., "High angle boundaries formed by grain subdivision mechanisms," *Acta Materialia*, vol. 45, pp. 3871–3886, 1997.

[47] Senkov O.N., Froes F.H., Stolyarov V.V., Valiev R.Z., Liu J., "Microstructure and microhardness of an Al-Fe alloy subjected to severe plastic deformation and aging," *Nanostructured Materials*, vol. 10, pp. 691–698, 1998.

[48] Senkov O.N., Froes F.H., Stolyarov V.V., Valiev R.Z., Liu J., "Microstructure of aluminum-iron alloys subjected to severe plastic deformation," *Scripta Materialia*, vol. 38, pp. 1511–1516, 1998.

[49] Stolyarov V.V., Shestakova L.O., Zhu Y.T., Valiev R.Z., "Formation of metastable states in nanostructured Al- and Ti-based alloys by the SPTS technique," *Nanostructured Materials*, vol. 12, pp. 923–926, 1999.

[50] Brodova G., Bashlykov D.V., Manukhin A.B., Stolyarov V.V., Soshnikova E.P., "Formation of nanostructure in rapidly solidified Al-Zr alloy by severe plastic deformation," *Scripta Materialia*, vol. 44, pp. 1761–1764, 2001.

[51] Figueiredo R.B., Pereira P.H. R., Aguilar M.T.P., Cetlin P., Langdon T.G., “Using finite element modeling to examine the temperature distribution in quasi-constrained high-pressure torsion,” *Acta Materialia*, vol. 60, pp. 3190–3198, 2012.

[52] Todaka Y., Umemoto M., Yamazaki A., Susaki J., Tsuchiya K., “Influence of high-pressure torsion straining conditions on microstructure evolution in commercial purity aluminum,” *Materials Transcactions*, vol. 49, pp. 7–14, 2008.

[53] Edalati K., Miresmaeili R., Horita Z., Kanayama H., Pippan R., “Significance of temperature increase in processing by high-pressure torsion,” *Materials Science and Engineering A*, vol. 528, pp. 7301–7305, 2011.

[54] El Aal M., Yoon E.Y., Kim H. S., “Recycling of AlSi8Cu3 alloy chips via high pressure torsion,” *Materials Science and Engineering A*, vol. 560, pp. 121–128, 2013.

[55] Cepeda-Jimnez C.M., Garca-Infanta J.M., Zhilyaev A.P., Ruano O.A., Carre F., “Influence of the supersaturated silicon solid solution concentration on the effectiveness of severe plastic deformation processing in Al-7% Si casting alloy,” *Materials Science and Engineering A*, vol. 528, pp. 7938–7947, 2011.

[56] Kawasaki M., “Different models of hardness evolution in ultrafine-grained materials processed by high-pressure torsion,” *Journal of Material Science*,

pp. 76–87, 2013.

[57] Gako M., Rosenberg G., "Correlation between hardness and tensile properties in ultra-high strength dual phase steel-short communication," *Materials Engineering - Materilov ininierstvo*, vol. 18, pp. 155–159, 2011.

[58] Ito Y., Horita Z., "Microstructural evolution in pure aluminum processed by high-pressure torsion," *Materials Science and Engineering A*, vol. 503, p. 3236, 2009.

[59] Setman D., Kerber M.B., Schafler E., Zehetbauer M., "Activation enthalpies of deformation-induced lattice defects in severe plastic deformation nanometals measured by differential scanning calorimetry," *Metallurgical and Materials Transactions A*, vol. 41. 4, pp. 810–815, 2010.

[60] Kawasaki M., Langdon T.G., "The significance of strain reversals during processing by high-pressure torsion," *Materials Science and Engineering A*, vol. 498, pp. 341–348, 2008.

[61] Moffat J.A., *Micromechanistic analysis of fatigue in aluminium-silicon casting alloys.* PhD thesis, University of Southampton, 2007.

[62] Mbuya T.O., Sinclair I., Mose B.R., Maranga S.M., Reed P.A.S., "Characterisation of the influence of minor elements on microstructure variation in a secondary cast aluminium piston alloy," in *Proceedings of 12th international*

conference on aluminium alloys, September 5-9, 2010, Yokohama, Japan. The Japan Institute of Light Alloys , 2010.

[63] Bruno Mose R., "Effect of minor elements on microstructure and mechanical properties of secondary Al-Si alloys," Master's thesis, Jomo Kenyatta University of Agriculture and Technology, 2009.

[64] Figueiredoa R.B., Cetlin P.R., Langdon T.G., "Using finite element modeling to examine the flow processes in quasi-constrained high-pressure torsion," *Materials Science and Engineering A*, vol. 528, pp. 8198– 8204, 2011.

[65] Figueiredo R.B., Faria G.C., Cetlin P.R., Langdon T.G., "Three-dimensional analysis of plastic flow during high-pressure torsion," *Journal of Material Science*, vol. 48, pp. 4524–4532, 2013.

[66] Estrin Y., Molotnikov A., Davies C.H.J., Lapovok R., "Strain gradient plasticity modelling of high-pressure torsion," *Journal of the Mechanics and Physics of Solids*, vol. 56, pp. 1186–1202, 2008.

[67] *The ImageJ user guide 1.44, 2011.*

[68] Janaka G. H. A., Kumara J., Kimitoshi Hayano & Keita Ogiwara, "Image analysis techniques on evaluation of particle size distribution of gravel," *International Journal of Geotechnique, Construction Materials and Environment*, vol. 3, pp. 290–297, 2012.

[69] Haden C.V., Harlow D.G., "Statistical characterization of the geometric properties of particles in 7075-T6 aluminium alloy," *Fatigue Fracture, Engineering Materials and Structures*, vol. 10, pp. 1–10, 2014.

[70] Mbuya T.O., *Analysis of microstructure and fatigue micromechanisms in cast aluminium piston alloys.* PhD thesis, University of Southampton, Faculty of Engineering & Environment, Engineering Sciences, 2011.

[71] Saramak D., "Mathematical models of particle size distribution in simulation analysis of high-pressure grinding roll operations," *Physicochemical Problems of Mineral Processing*, vol. 49(1), pp. 121–131, 2013.

[72] Kawasaki M., Figueiredo R., Langdon T., "An investigation of hardness homogeneity throughout disks processed by high-pressure torsion," *Acta Materialia*, vol. 59, pp. 308–316, 2011.

[73] Berbon P.B., Furukuwa M., Horita Z., Nemoto M., Tsenev N.K., Valiev R.Z., Langdon T.G., "Requirements for achieving high-strain-rate superplasticity in cast aluminium alloys," *Philosophy Magazine Letters*, vol. 78, pp. 3–13, 1998.

[74] Chen C., *Characterisation of Intermetallic phases in multicomponent Al-Si alloys for piston applications.* PhD thesis, Loughborough University, 2006.

[75] Moreno-Valle E.C., Sabirov I, Perez-Prado M.T., Murashkin M.Y., Bobruk E.V., Valiev R.Z., "Effect of the grain refinement via severe plastic deforma-

tion on strength properties and deformation behavior of an Al-6061 alloy at room and cryogenic temperatures," *Materials Letters*, vol. 65, pp. 2917–2919, 2011.

[76] Zuo Y.B., Fan Z., Zhu Q.F., Lei J.Z., "Modification of a hypereutectic aluminium silicon alloy under the influence of intensive melt shearing," *Materials Science Forum*, vol. 765, pp. 140–144, 2013.

[77] Barekar N.S., Babu H., Dhindaw B.K., Fan Z., "Effect of intensive shearing on morphology of primary silicon and properties of hypereutectic aluminium-silicon alloy," *Materials Science and Technology*, vol. 3, pp. 1–6, 2009.

[78] Szczygiel P., Roven H. J., Reiso O., "On the effect of severe plastic deformation on recycled experimental aluminium alloys: Nanostructures, particle break-up and properties," *Materials Science and Engineering A*, vol. 410-411, pp. 261–264, 2005.

[79] Wang J., Horita Z., Furukuwa M., Nemoto M., Tsenev N.K., Valiev R.Z., Ma Y., Langdon T.G., "An investigation of ductility and microstructural evolution in an aluminium-3% magnesium alloy with submicron grain size," *Journal of Material Science*, vol. 8, pp. 2810–2816, 1993.

Appendix A

Goodness of fit test for 3-parameter lognormal and Weibull distributions

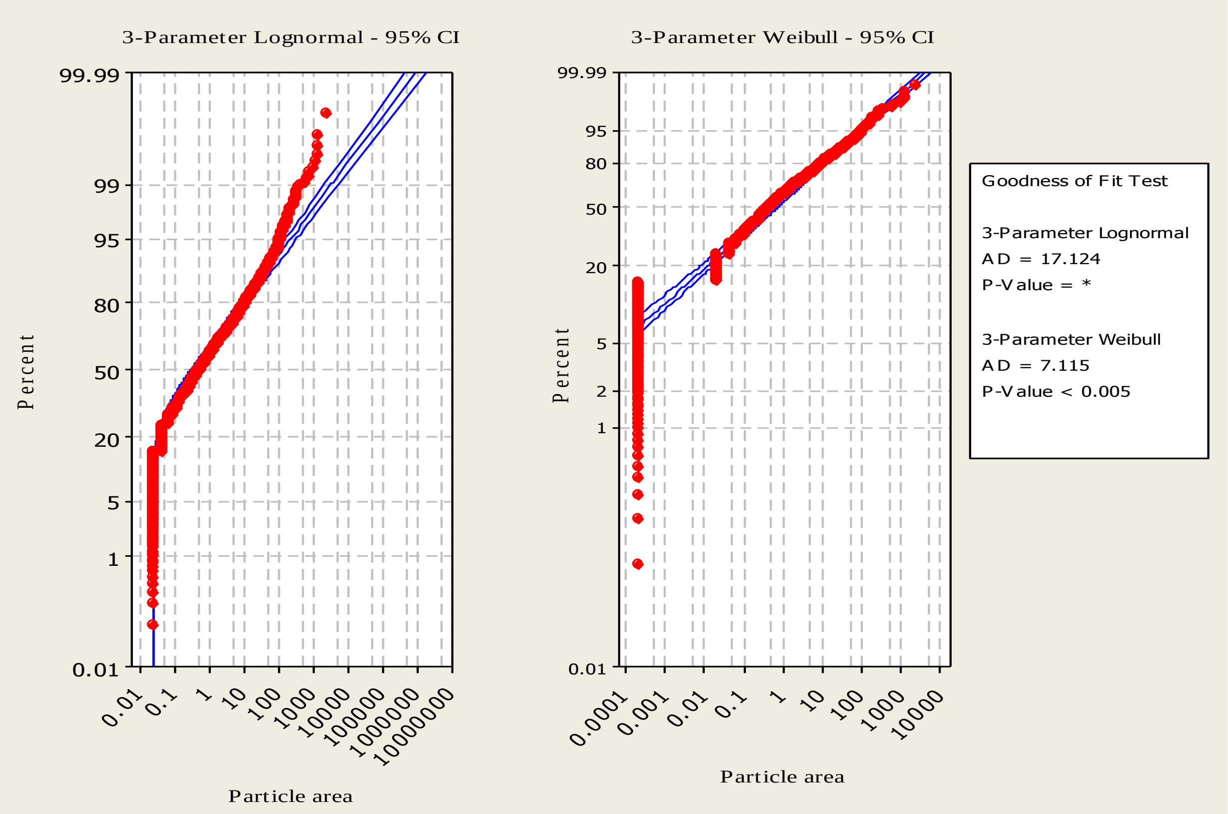

Figure 6.1: Probability plots for particle areas at the central region of Al-12%Si alloy after $\frac{1}{4}$ turn of HPT processing.

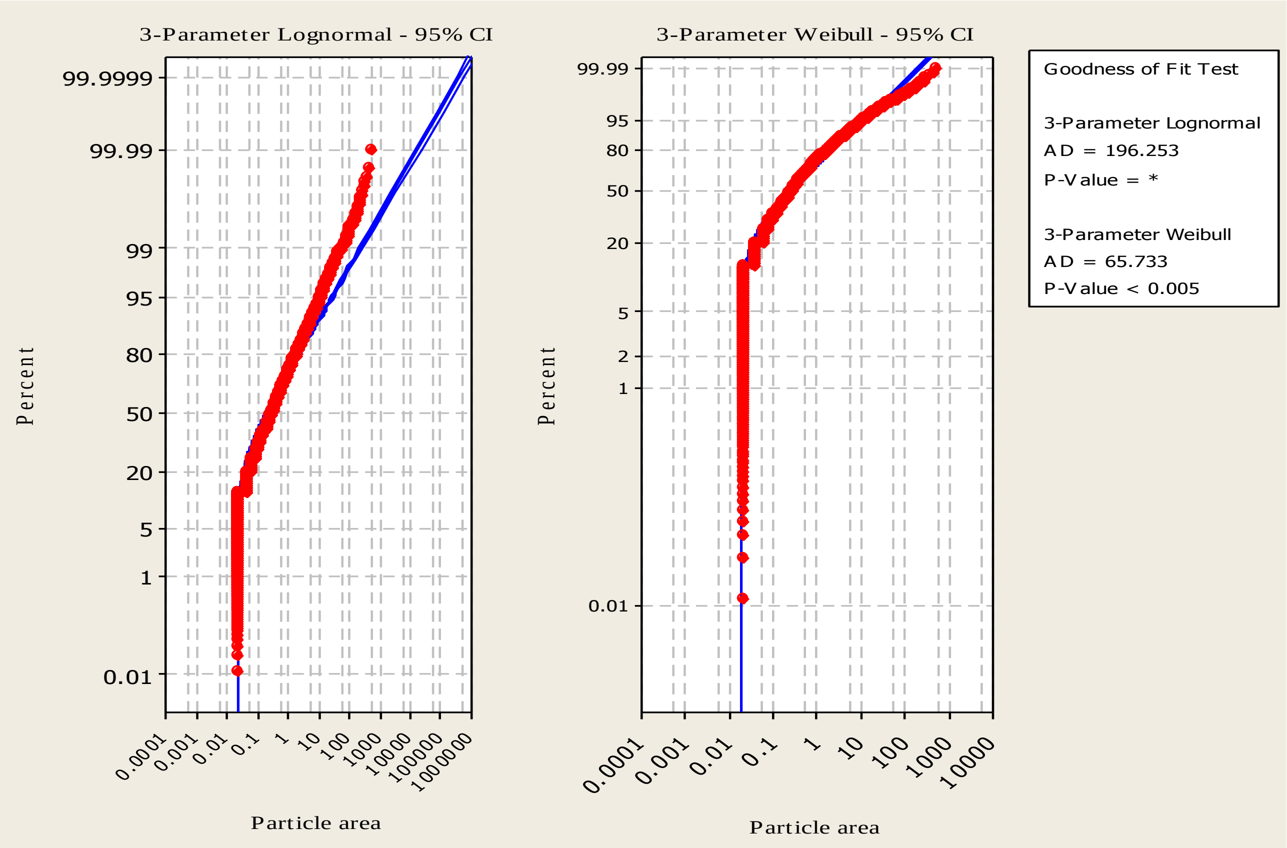

Figure 6.2: Probability plots for particle areas at the central region of Al-12%Si alloy after 10 turns of HPT processing.

Appendix B

Hardness of intermetallic phases

Table 6.1: Properties of particles and phases in Al-Si piston [74]

Phase	**Hardness (HV)**		
	25^{o}C	200^{o}C	350^{o}C
Si	1132	1132	938.1
AlFeMnSi	1101	1030	826
Al_3Ni_2	1071	969	683
Al_7Cu_4Ni	948	836	510
Al_9FeNi	785	683	591
$Al_5Cu_2Mg_8Si_6$	663	602	520
Al_2Cu	591	540	254
Al matrix	153	71.4	10.2